

The Design, Synthesis and Application of Redox-Responsive MRI Contrast Agents

by

Meng Yu

A dissertation submitted to the Graduate Faculty of
Auburn University
in partial fulfillment of the
requirements for the Degree of
Doctor of Philosophy of Science

Auburn, Alabama
August 1, 2015

Reactive oxygen species, MRI contrast agent, Redox-responsive, Manganese

Copyright 2015 by Meng Yu

Approved by

Christian R. Goldsmith, Chair, Associate Professor of Chemistry and Biochemistry

David M. Stanbury, Professor of Chemistry and Biochemistry

Douglas C. Goodwin, Associate Professor of Chemistry and Biochemistry

Anne E. V. Gordon, Associate Professor of Chemistry and Biochemistry

Dean D. Schwartz, Associate Professor of Physiology

Abstract

Reactive oxygen species (ROSs), such as hydroxyl radicals, superoxide anions and hydrogen peroxide, are side products of aerobic respiration. Although ROSs regulate several physiological processes, they have been implicated in the pathology of many health conditions. The need to elucidate the specific roles that ROSs play in these disorders has spurred the development of various techniques to detect oxidative stress. Such techniques have the promise to better understand the pathologies and allow the early diagnosis of several diseases. Magnetic resonance imaging (MRI) is particularly attractive due to its good visualization depth which allows it to be used in non-invasive whole body imaging.

MRI contrast agents are commonly utilized to shorten the relaxation time of protons and enhance the contrast. In this dissertation, three different categories of manganese-based MRI contrast agents were synthesized and characterized. Each has a redox-active ligand that can react with hydrogen peroxide. Upon activation, the contrast agents undergo structural changes that can alter either the overall paramagnetism or the hydration number of the manganese ions with concomitant changes to the longitudinal relaxation time (T_1). The ability of $[\text{Mn}(\text{H}_4\text{qtp}_2)\text{Br}_2]$ to identify doxorubicin-induced oxidative stress in the *ex vivo* imaging of rat hearts demonstrates the viability of this strategy as a means to detect the over-production of ROSs before they can damage tissues.

Acknowledgements

This dissertation was completed under the supervision of Prof. Christian R. Goldsmith. I spent five years developing redox-responsive MRI contrast agents. This project was difficult at the beginning. Fortunately, I had a great advisor who was always willing to give me insightful suggestions when needed. His knowledge of the field and his critical analysis of the problems that I encountered taught me much. I would also like to thank Prof. David M. Stanbury for helpful discussions. I also greatly appreciate Prof. Anne E. V. Gorden for allowing me to borrow her chemicals and instruments. Prof. John D. Gorden's skill in crystallography and helpful advice greatly contributed to the work. I'm thankful to Prof. Douglas C. Goodwin for serving on my committee as a substitute. I also thank Prof. Evert Duin for his help in the design of EPR experiments and the subsequent data interpretation as well as Dr. Yonnie Wu for his analogous assistance with mass spectrometry. I would also like to express my gratitude to our collaborators for their enthusiasm and hard work. Prof. Dean D. Schwartz helped us with the studies of the antioxidant activity and cytotoxicity. Dr. Ronald J. Beyers helped us design and conduct all the MRI experiments. Prof. Russell C. Cattley and his laboratory prepared the animals for the *ex vivo* cardiac imaging. Last but not least, I appreciate the friendship with my previous and current group members: Dr. Yu He, Dr. Wenchan Jiang, Dr. Qiao Zhang, and Angela Bell-Taylor. I also thank my former undergraduate mentees: Stephen L. Ambrose, Zachary L. Whaley, and T. Miller Bradford. Meghan Ward, Robert Boothe, and Adam Bashir are continuing my work, and I wish them each the best of luck.

In the end, I want to thank my family members and my girlfriend Yang Peng for their support and encouragement; without these, I could not have overcome all the difficulties on the way to my PhD.

Table of Contents

Abstract.....	ii
Acknowledgements.....	iii
Table of Contents.....	v
List of Tables.....	viii
List of Figures.....	ix
List of Schemes.....	xiv
Chapter 1 Introduction to Redox-Responsive MRI Contrast Agents.....	1
1.1 Reactive Oxygen Species in Biology.....	2
1.2 Current Means to Detect ROSs.....	2
1.3 Introduction to Magnetic Resonance Imaging (MRI) and Fundamental Principles in Designing MRI Contrast Agents.....	5
1.4 Introduction to Redox-Responsive MRI Contrast Agents.....	7
1.5 T_1/T_2 -weighted Redox-Responsive MRI Contrast Agents.....	8
1.5.1 Magnetism-Based Redox-Responsive MRI Contrast Agents.....	9
1.5.2 Hydration Number-Based Redox-Responsive MRI Contrast Agents.....	13
1.5.3 Tumbling Rate-Based Redox-Responsive MRI Contrast Agents.....	20
1.6 CEST-Derived Redox-Responsive MRI Contrast Agents.....	21
1.6.1 Ligand-Based Redox-Responsive PARACEST Agents.....	23
1.6.2 Metal-Based Redox-Responsive PARACEST Agents.....	25
References.....	28
Chapter 2 A Magnetic Resonance Imaging Contrast Agent Capable of Detecting Hydrogen Peroxide.....	35

2.1 Introduction.....	36
2.2 Experimental Section.....	37
2.3 Results and Discussion.....	43
2.4 Conclusions.....	48
Appendix.....	49
References.....	62
Chapter 3 A Mononuclear Manganese(II) Complex Demonstrates a Strategy to Simultaneously Image and Treat Oxidative Stress.....	65
3.1 Introduction.....	66
3.2 Experimental Section.....	67
3.3 Results and Discussion.....	73
3.4 Conclusions.....	81
Appendix.....	83
References.....	104
Chapter 4 Adding a Second Quinol to a Redox-Responsive MRI Contrast Agent Improves its Relaxivity Response to H ₂ O.....	107
4.1 Introduction.....	108
4.2 Experimental Section.....	111
4.3 Results.....	120
4.4 Discussion.....	136
4.5 Conclusions.....	141
Appendix.....	142
References.....	160
Chapter 5 Summary and Future Perspectives.....	165

References..... 171

List of Tables

Table 2A.1 Selected crystallographic data for [Mn(Hptp1)(MeCN)](ClO ₄) ₂ and [Mn ₂ (Hptp1 ₂)(MeCN) ₂](ClO ₄) ₃	53
Table 2A.2 Selected bond lengths (Å) and bond angles (°) for [Mn(Hptp1)(MeCN)](ClO ₄) ₂ ..	54
Table 2A.3 Selected bond lengths (Å) for [Mn ₂ (Hptp1 ₂)(MeCN) ₂](ClO ₄) ₃	54
Table 3A.1 Selected crystallographic data for 1	97
Table 3A.2 Selected bond lengths for 1	97
Table 4.1 Selected crystallographic data for 2 and 3	124
Table 4.2 Selected bond lengths (Å) for complexes 2 and 3	124
Table 4A.1 Doxorubicin rat serum enzyme and histology results	157
Table 4A.2 Listed data for binding constant (log(K)) measurement of 2	159

List of Figures

Figure 1.1 Examples of reaction-based fluorescent probes for ROSs detection.....	4
Figure 1.2 Schematic demonstration of supramolecular adduct between Mn ^{II} tpps and poly-β-CD	10
Figure 1.3 Structural representation of Mn ^{II} -HBET and Mn ^{III} -HBET complexes. Oxidation state of metal ion can be tuned by reacting with H ₂ O ₂ and glutathione (GSH)	11
Figure 1.4 Structural demonstration of glycyilmethyl DOTA(Gd) 5-hydroxytryptamide (5-HT- DOTA(Gd), DOTA = 1,4,7,10-tetraazacyclododecane-1,4,7,10-tetraacetic acid)	12
Figure 1.5a Ligand structure of Mn ^{II} -Hptp1	13
Figure 1.5b ORTEP representation of binuclear product [Mn ₂ (Hptp1 ₂)(MeCN) ₂] ³⁺	13
Figure 1.6 Schematic representations of proposed mechanisms of activation by β-galactosidase for β-EGadMe and α-EGadMe, respectively	14
Figure 1.7a Transformation of complex between acyclic and cyclic forms triggered by NADH and H ₂ O ₂	16
Figure 1.7b Conversion of the open-ring form to spiropyran isomer by NADH	16
Figure 1.8 4NO ₂ 2MeOSAGd reduced to 4NH ₂ 2MeOSAGd under hypoxia.....	17
Figure 1.9 Proposed mechanism for H ₂ O ₂ detection by MnH ₂ qtp1	18
Figure 1.10 Structure of Gd-DO3AS-Act.....	19
Figure 1.11 Schematic representation of the encapsulated Gd ₂ O ₃ NPs “turned on” through polymer degradation	19
Figure 1.12 DOTA derivatives bearing thiol groups (n = 3-9).....	20
Figure 1.13 Schematic demonstration of Gd(III) complex included nanocapsules decompose through disulfide bond cleavage under reducing condition.....	21
Figure 1.14 Representation of structural change induced by β-NADH.....	23
Figure 1.15 Reduction of nitroxide radical groups to hydroxylamines by L-ascorbic acid	24

Figure 1.16 Mechanistic demonstration of responsive lipoCEST agent triggered by cleavage between the lipid core and Gd(III) complex (SR: paramagnetic Shift Reagent)	25
Figure 1.17 Structure of $[\text{Co}(\text{TPT})]^{2+}/[\text{Co}(\text{TPT})]^{3+}$ complexes	27
Figure 2.1 ORTEP representation of $[\text{Mn}(\text{Hptp1})(\text{MeCN})]^{2+}$	44
Figure 2.2 ORTEP representation of $[\text{Mn}_2(\text{Hptp1}_2)(\text{MeCN})_2]^{3+}$	45
Figure 2A.1 Mass spectrum (ESI) for $[\text{Mn}(\text{Hptp1})(\text{MeCN})](\text{ClO}_4)_2$ in MeCN	49
Figure 2A.2 Mass spectrum (ESI) for $[\text{Mn}_2(\text{Hptp1}_2)(\text{MeCN})_2](\text{ClO}_4)_3$ in MeCN	50
Figure 2A.3 Mass spectrum (ESI) of an aqueous solution containing 1.00 mM $[\text{Mn}(\text{Hptp1})(\text{MeCN})](\text{ClO}_4)_2$ and 10 mM H_2O_2	51
Figure 2A.4 IR spectrum of $[\text{Mn}(\text{Hptp1})(\text{MeCN})](\text{ClO}_4)_2$ (KBr)	52
Figure 2A.5 IR spectrum of $[\text{Mn}_2(\text{Hptp1}_2)(\text{MeCN})_2](\text{ClO}_4)_3$ (KBr)	52
Figure 2A.6 X-Band electron paramagnetic resonance spectra of 1.0 mM $[\text{Mn}(\text{Hptp1})(\text{MeCN})](\text{ClO}_4)_2$ in an aqueous solution containing 50 mM HEPES buffered to 7.0 ..	55
Figure 2A.7 X-Band electron paramagnetic resonance spectra of 0.50 mM $[\text{Mn}_2(\text{Hptp1}_2)(\text{MeCN})_2](\text{ClO}_4)_3$ in an aqueous solution containing 50 mM HEPES buffered to 7.0	56
Figure 2A.8 Spectrophotometric analysis of the reaction between 0.10 mM $\text{Fe}(\text{ClO}_4)_2$ and 0.10 mM $[\text{Mn}(\text{Hptp1})(\text{MeCN})](\text{ClO}_4)_2$ in MeCN at 25 °C	57
Figure 2A.9 Longer range analysis of the reaction between 0.10 mM $\text{Fe}(\text{ClO}_4)_2$ and 0.10 mM $[\text{Mn}(\text{Hptp1})(\text{MeCN})]^{2+}$ in MeCN at 25 °C	58
Figure 2A.10 Plots of $(1/T_1)$ as functions of Mn(II) concentration for $[\text{Mn}(\text{Hptp1})(\text{MeCN})](\text{ClO}_4)_2$ in the presence (black) and absence (blue) of 10 mM H_2O_2	59
Figure 2A.11 Mass spectrum (ESI) for a sample containing 1.00 mM $[\text{Mn}(\text{Hptp1})(\text{MeCN})](\text{ClO}_4)_2$, 1.50 mM H_2O_2 , and 1.00 mM 2,4-dimethylphenol (dmp) in MeCN	60
Figure 2A.12 Plots of $(1/T_1)$ as functions of Mn(II) concentration for $[\text{Mn}(\text{Hptp1})(\text{MeCN})](\text{ClO}_4)_2$ in the presence (blue) and absence (black) of 10 mM H_2O_2	61
Figure 3.1 Structure of $[\text{Mn}(\text{H}_2\text{qtp1})(\text{MeCN})]^{2+}$	75
Figure 3.2 Superoxide scavenging effects of 1 and 2	79

Figure 3.3 DPPH free radical scavenging assay of 1 , 2 , and ascorbic acid	80
Figure 3A.1 Spectrophotometric analysis of the reaction between 0.10 mM Fe(ClO ₄) ₂ and 0.10 mM [Mn(H ₂ qtp1)(MeCN)](OTf) ₂ in MeCN at 25 °C	83
Figure 3A.2 Longer range analysis of the reaction between 0.10 mM Fe(ClO ₄) ₂ and 0.10 mM [Mn(H ₂ qtp1)(MeCN)](OTf) ₂ in MeCN at 25 °C	84
Figure 3A.3 Mass spectrum (ESI) for [Mn(H ₂ qtp1)(MeCN)](OTf) ₂ (1) in MeCN.....	85
Figure 3A.4 Mass spectrum (ESI) for 1 in MeCN after reaction with 10 equiv of H ₂ O ₂ for 30 min	86
Figure 3A.5 Mass spectrum (ESI) for 1 in H ₂ O after reaction with 4 equiv. of H ₂ O ₂ for 30 min	87
Figure 3A.6 ¹ H NMR spectrum of the diamagnetic product from the reaction between 10 mM 1 and 2 equiv of Zn(ClO ₄) ₂ in MeCN- <i>d</i> ₃	88
Figure 3A.7 ¹ H NMR spectrum of the complex formed from the reaction between 10 mM H ₂ qtp1 and 10 mM Zn(ClO ₄) ₂ in MeCN- <i>d</i> ₃	89
Figure 3A.8 HQ-COSY NMR of the Zn(II)-H ₂ qtp1 complex from Figure 3A.7.....	90
Figure 3A.9 ¹ H NMR spectrum of reaction between 10 mM 1 and 4.0 equiv of H ₂ O ₂ in MeCN- <i>d</i> ₃	91
Figure 3A.10 IR spectrum of 1 (KBr). The 3384 and 3472 cm ⁻¹ features are assigned to the O-H stretches of the H ₂ qtp1 quinol.....	92
Figure 3A.11 IR spectrum of the crude product from the reaction between 1.0 mM 1 and 4.0 mM H ₂ O ₂ in MeOH.....	93
Figure 3A.12 X-band EPR spectrum of a water solution containing 1.0 mM of 1	94
Figure 3A.13 X-band EPR spectrum of the reaction between 1.0 mM 1 and 10 mM H ₂ O ₂ in water.....	94
Figure 3A.14 UV/Vis spectra depicting the reaction between 0.10 mM 1 and 10 mM H ₂ O ₂ in H ₂ O	95
Figure 3A.15 IR spectrum of the product of the reaction between dithionite and the oxidized form of 1	96

Figure 3A.16 Plots of $(1/T_1)$ versus Mn(II) concentration for 1 in the presence (blue) and absence (black) of 10 mM H_2O_2	98
Figure 3A.17 Plots of $(1/T_1)$ versus Mn(II) concentration for 1 in the presence of various oxidants.....	99
Figure 3A.18 Cyclic voltammetry of an aqueous solution containing 1.0 mM 1 and 0.10 M phosphate (NaH_2PO_4/Na_2HPO_4) buffered to pH 7.2	100
Figure 3A.19 Cyclic voltammetry of an aqueous solution containing 1.0 mM H_2qtp1 , 1.0 mM $Zn(ClO_4)_2$, and 0.10 M phosphate (NaH_2PO_4/Na_2HPO_4) buffered to pH 7.2.....	101
Figure 3A.20 Cyclic voltammetry of an aqueous solution containing 1.0 mM 1 and 0.10 M phosphate (NaH_2PO_4/Na_2HPO_4) buffered to pH 7.2	102
Figure 3A.21 Cytotoxic effects of 1 and 2 on H9c2 cells.....	103
Figure 4.1 Structure of $[Mn(H_4qtp2)Br_2]$ (2).....	123
Figure 4.2 Structure of $[Mn(qtp2)Br_2]$ (3)	123
Figure 4.3 X-band EPR spectra of 1.0 mM solutions of 2 in MeOH in the absence and presence of 10 mM H_2O_2	127
Figure 4.4 UV/vis spectra corresponding to the 298 K reaction between a 0.10 mM 2 and 10 mM H_2O_2 in MeOH.....	128
Figure 4.5 Plots of $(1/T_1)$ versus Mn(II) concentration for 2 in the presence (blue) and absence (black) of 10 mM H_2O_2	130
Figure 4.6 Cytotoxicity of 2 towards H9c2 cells	131
Figure 4.7 T_1 maps of rat hearts treated without and with contrast agent 2	133
Figure 4.8 <i>Ex vivo</i> cardiac MRI of rats treated with contrast agent 2	134
Figure 4.9 Superoxide scavenging effects of 1 , 2 , and $[Mn(Htp1)(MeCN)](ClO_4)_2$	135
Figure 4.10 DPPH free radical scavenging assay of 2 and ascorbic acid.....	135
Figure 4A.1 UV/Vis spectra depicting the stability of a 0.10 mM solution of $[Mn(H_4qtp2)Br_2]$ (2) in MeOH to air.	142

Figure 4A.2 Spectrophotometric analysis of the reaction between 0.10 mM Fe(ClO ₄) ₂ and 0.10 mM 2 in MeOH at 298 K.....	142
Figure 4A.3 Cyclic voltammetry of 1.0 mM 2 in 0.10 M phosphate buffer (NaH ₂ PO ₄ /Na ₂ HPO ₄ , pH=7.2).	143
Figure 4A.4 Mass spectrometry (ESI) of 2 in MeOH.....	144
Figure 4A.5 Mass spectrometry (ESI) of [Mn(qtp2)Br ₂] (3) in MeCN.....	144
Figure 4A.6 Mass spectrometry (ESI) of a mixture of 2 in H ₂ O and 4 equiv. of H ₂ O ₂	145
Figure 4A.7 Mass spectrometry (ESI) of a reaction between 2 and 4 equiv. of H ₂ O ₂ in MeOH	146
Figure 4A.8 Mass spectrometry (ESI) of a reaction between 2 and 8 equiv. of H ₂ O ₂ in MeOH	147
Figure 4A.9 IR spectrum of 2 (KBr).....	148
Figure 4A.10 IR spectrum of the crude product from the reaction between 1.0 mM 2 and 4.0 mM H ₂ O ₂ in MeOH.....	149
Figure 4A.11 IR spectrum of 3 (KBr).....	150
Figure 4A.12 ¹ H NMR spectra of H ₄ qtp2 in CD ₃ OD (top) and CD ₃ CN (bottom).	151
Figure 4A.13 ¹ H NMR spectrum of the diamagnetic product from the reaction between 10 mM 2 and 20 mM Zn(ClO ₄) ₂ in CD ₃ CN	152
Figure 4A.14 ¹ H NMR spectrum of the diamagnetic product from the reaction between 10 mM 3 and 20 mM Zn(ClO ₄) ₂ in CD ₃ CN	153
Figure 4A.15 ¹ H NMR spectrum of the diamagnetic product between 2 , 4 equiv. of H ₂ O ₂ , and 2 equiv. of Zn(ClO ₄) ₂ in CD ₃ CN	154
Figure 4A.16 ¹ H NMR spectrum of the diamagnetic product between 2 , 8 equiv. of H ₂ O ₂ , and 2 equiv. of Zn(ClO ₄) ₂ in CD ₃ CN	155
Figure 4A.17 ORTEP representation of the ligand precursor <i>N</i> -(2,5-dihydroxybenzyl)- <i>N,N'</i> -bis(2-pyridinylmethyl)-1,2-ethanediammonium trifluoroacetate	156
Figure 4A.18 Gene expression in the hearts and kidneys of doxorubicin-treated rats	158

List of Schemes

Scheme 2.1 Structure of Hptp1 ligand.....	37
Scheme 3.1 Ligand structure of 1 and 2	73
Scheme 3.2 Demonstration of quinol oxidation by H ₂ O ₂	74
Scheme 4.1 Ligand structure for complex 1 and 2	110
Scheme 4.2 Mechanism of MRI response to H ₂ O ₂	110

Chapter 1

Introduction to Redox-Responsive MRI Contrast Agents

1.1 Reactive Oxygen Species in Biology

Reactive oxygen species (ROSs), such as hydrogen peroxide (H_2O_2), superoxide ($\text{O}_2^{\bullet-}$), and hydroxyl radicals ($\bullet\text{OH}$), are side products of aerobic respiration that result from the incomplete reduction of O_2 to H_2O . Although recent research has found that ROSs play important roles in mediating several biological processes, such as cell signaling, gene expression, neurotransmission and the immune response,¹⁻⁵ ROSs are better known for being implicated in several physiological conditions. Under normal health conditions, the concentrations of ROSs are strictly controlled by enzymes such as catalases and superoxide dismutases; however, the failure of these regulating systems can lead to ROSs accumulation and oxidative stress. Oxidative stress has been linked to many and diverse health disorders, such as inflammatory, cardiovascular and neurological diseases.⁶⁻¹⁰ The details of how ROSs participate in these aforementioned pathologies remain elusive. Understanding the roles of ROSs in pathological progression is of paramount significance in facilitating the early diagnosis and treatment of the diseases. Consequently, substantial efforts have been made to develop several complementary approaches to detect ROSs in biological systems.

1.2 Current Means to Detect Reactive Oxygen Species

Due to the fleeting nature of ROSs and the presence of anti-oxidants that are capable of degrading them, sensors for ROSs need to be highly sensitive. From this regard, fluorescent probes are attractive due to their great sensitivity, high spatial resolution, and facile data handling. Commonly, small organic fluorophores are modified with functional units that can react with certain ROSs to result in changes in either the intensity or wavelength of emission. Seemingly innumerable fluorescent probes have been made, and only a few paradigmatic examples are listed here for illustration. In order to detect ROSs biological systems, fluorescent probes need to

be reaction-based, meaning that they rely on a reaction that is bioorthogonal and does not interfere with endogenous cellular processes.¹¹

Reaction-based fluorescent sensors can be divided into two major categories: organic and metal-mediated. A commonly used strategy in designing purely organic fluorescent probes for ROSs is to use an oxidative cleavage reaction to deprotect a fluorophore. Chang's group has exploited the reactivity of arylboronates to detect H₂O₂ selectively.¹²⁻¹⁸ H₂O₂ nucleophilically attacks the boronate to yield phenol, with concurrent opening of the spiro-lactone ring generating a highly fluorescent species (Fig. 1.1a).¹³ Nagano used the same fundamental strategy for H₂O₂ detection, but employed a benzil group as the redox-responsive trigger (Fig. 1.1b).¹⁹ The benzil group quenches the fluorescence of the appended fluorescein through the donor-excited photoinduced electron transfer process (PET) due to its low enough energy level of LUMO capable of accepting electrons from the excited probe. Upon reacting with H₂O₂, the benzil group is initially converted into benzoic anhydride through a Baeyer-Villiger type mechanism before being hydrolyzed into benzoic acid. Compared with the aforementioned boronate ester approach, the benzil-based fluorescent probe has no response towards NO, a faster reaction rate, and lower background emission. These qualities make it more suitable for biological application. Oxidative *O*-dearylation and *N*-dearylation have also been used for detecting highly reactive oxygen species (hROS) such as hydroxyl radical (\bullet OH), peroxynitrite (ONOO⁻), and hypochlorite (OCl⁻) (Fig. 1.1c).²⁰

Metal-mediated reaction-based fluorescent probes represent another versatile approach for ROS detection. The wide range of redox potentials for transition metal ions and the noncovalent bonds between metals and their ligands makes tuning the reactivity of coordination complexes more facile than it is for an organic analog. Lippard and co-workers developed a

Cu(II)-aminoquinoline complex; prior to its activation, the paramagnetic Cu(II) quenches the fluorescence (Fig. 1.1d).²¹ NO induces reductive nitrosylation, which releases the metal and restores the fluorescence. This is the first example of a fluorescent probe that can directly and selectively detect NO in both aqueous solution and living cells via a metal-mediated reaction.

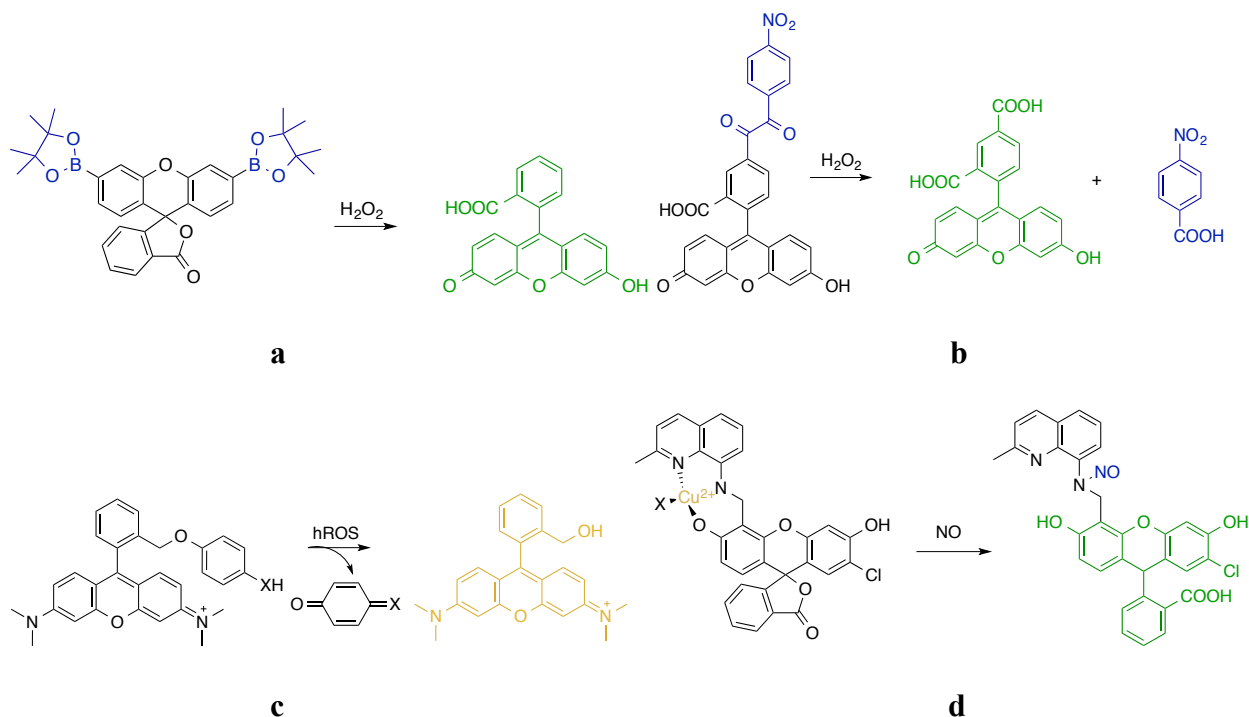


Figure 1.1 Examples of reaction-based fluorescent probes for ROSs detection. **a**, Oxidative cleavage of arylboronates to phenols by H_2O_2 . **b**, Benzil oxidative cleavage for selective H_2O_2 detection. **c**, Oxidative *O*-dearylation reaction triggered by highly reactive oxygen species. **d**, Reductive *N*-nitrosylation of a copper-dye complex by NO.¹¹

Generally speaking, properly designed fluorescent probes can be quite effective in cell imaging with excellent selectivity, sensitivity, cell permeability, and biocompatibility.^{11,22-25} However, the short wavelength of light used for excitation during fluorescent imaging limits the visualization depth, and visualizing biological processes within thick samples is difficult. Although near-infrared (NIR) optical imaging techniques can compensate somewhat, the issue

still remains.^{18,26} Additionally, fluorophores generally undergo side reactions, such as photobleaching or self-decomposition, that could potentially lead to data misinterpretation.^{27,28} Hence, although fluorescence is quite valuable for study within thin tissues and cell cultures, its application in whole-body imaging is impractical. This has spurred the development of alternative imaging techniques.

1.3 Introduction to Magnetic Resonance Imaging (MRI) and Fundamental Principles in Designing MRI Contrast Agents

Magnetic resonance imaging (MRI) is a powerful clinical technique used to obtain high-resolution three-dimensional spatial images. MRI uses long wavelength radio frequency photons to excite NMR active nuclei under a magnetic field. After the radio frequency photon is absorbed, the excited nuclei relax to their equilibrium state. This process changes the overall magnetization and emits a RF nuclear magnetic echo than can be used to generate image patterns. Most MR contrast images are derived from water protons. Soft tissues can be differentiated from each other through their water content or local environment.^{29,30} Other NMR-active nuclei, such as ¹⁹F or ¹³C, have also been used for MRI, but these are less useful due to their much less abundances in humans and relying on a high concentration of probes to be effective.^{31,32}

For practical purposes, MRI contrast agents are used to shorten the relaxation time and increase the amount of RF radiation absorbed. This provides sharper contrast between water-rich and water-deficient regions.³³ Normally, MRI contrast agents are monocuclear metal complexes containing paramagnetic metals, such as Gd³⁺, Mn²⁺, and Fe³⁺, although nanoparticles of materials such as iron oxide have also been explored. There are two relaxation pathways: longitudinal relaxation T_1 (spin-lattice relaxation) and transverse relaxation T_2 (spin-spin relaxation). $1/T_n$ corresponds to the rate of relaxation. Larger $1/T_1$ values tend to enhance the

signal whereas increasing $1/T_2$ leads to lower signal contrast. Contrast agents increase both longitudinal ($1/T_1$) and transverse ($1/T_2$) relaxation rates. Depending on the extent of change in $1/T_1$ and $1/T_2$, contrast agents can be divided into T_1 -weighted and T_2 -weighted MRI contrast agents.³⁴ For example, Gd(III) has seven unpaired electrons ($I = 7/2$) which is very paramagnetic and enhances $1/T_1$ and $1/T_2$ to similar degree. In tissues, the percentage change is greater for $1/T_1$; consequently, gadolinium-based contrast agents are more often utilized for T_1 -weighted imaging. Nanoparticles such as iron oxide display larger changes in $1/T_2$ than $1/T_1$ and are therefore more frequently used as T_2 -weighted contrast agents. The term relaxivity (r_i) evaluates how efficiently a contrast agent is able to enhance the relaxation rate. Statistically, r_1 and r_2 represent the change in $1/T_1$ and $1/T_2$ per millimolar of contrast agent as defined by equation (1) and (2) where subscripts “d” and “p” represent diamagnetic and paramagnetic contributions, respectively.^{30, 34} The paramagnetic portion is normally larger and linearly proportional to the concentration of contrast agent ([CA]).

$$(1/T_i) = (1/T_i)_d + (1/T_i)_p \quad (1)$$

$$(1/T_i) = (1/T_i)_d + r_i[\text{CA}] \quad (2)$$

Additionally, the paramagnetic relaxation rate is further determined by inner-sphere and outer-sphere interactions. The inner-sphere relaxation describes the contribution by solvent molecules directly coordinated to the paramagnetic center. The outer-sphere relaxation correlates with solvents communicating with the metal center through more remote interactions such as hydrogen bonding. The Solomon-Bloembergen-Morgan equations elucidate various factors that contribute to the inner-sphere relaxivity.³⁰ These include (1) the number of solvent molecules directly coordinating to the metal ion or inner-sphere aquatic number (q), (2) the distance between MRI active nuclei and unpaired electron spin (r), (3) the rotational correlation time (τ_R)

with a slower tumbling rate resulting in higher relaxivity, (4) solvent exchange rate or the residence lifetime of solvent molecules (τ_m), and (5) the field strength of the applied magnetic field.³⁰ Outer-sphere relaxation has two components: second-sphere relaxation resulting from water molecules associating with the paramagnetic center through hydrogen bonds and outer-sphere relaxation from bulk water.³⁰ The second-sphere relaxation mechanism can be parameterized in a manner similar to inner-sphere relaxation. The key difference is that second-sphere water molecules are much more difficult to quantify and monitor. Outer-sphere relaxation mechanism originates from the translational diffusion of nearby water molecules around the paramagnetic center. Overall, outer-sphere relaxation is less straightforward and more poorly understood; as such, it has not been a factor in the design of contrast agents.^{30,34-37}

1.4 Introduction to Redox-Responsive MRI Contrast Agents

The redox environment refers to the reductive or oxidative stress around an organelle, cell, tissue, or organ. The development of imaging tools for monitoring the fluctuation of local physiological redox environments will help us to better understand the roles of ROSs in a variety of pathologies. MRI has the ability to non-invasively image biochemical events within organs and whole-body subjects, making it particularly valuable for biological sensing. This application requires contrast agents that display changes in relaxivity upon reaction with the target analytes. A large number of responsive MRI contrast agents have been developed that are sensitive to pH, enzymes, metal ions, reductants, and oxidants. Among all these probes, redox-responsive contrast agents are most relevant to this thesis. This is a relatively new research area that has attracted the attention of diverse researchers.^{38,39}

1.5 T_1/T_2 -weighted Redox-Responsive MRI Contrast Agents

Highly paramagnetic metal ions, such as Gd(III) and Mn(II), are commonly used in MRI contrast agents due to their excellent ability to decrease longitudinal relaxation (T_1) through dipole interaction between the unpaired electron spin on metal center and water protons. Superparamagnetic iron oxide nanoparticles are frequently used for T_2 -weighted imaging. These are normally small particles with magnetite (Fe_3O_4) and γ -maghemite (Fe_2O_3) cores coated with different materials, with overall diameters ranging from a few nm to a few hundred nm.³⁷ Although these nanoparticles are effective for simple MRI imaging, most responsive MRI contrast agents are based on mononuclear metal complexes in that their properties are easier to predict and manipulate based on theory. Therefore, the discussion will focus more on T_1 -based MRI contrast agents. Although both inner-sphere and outer-sphere components contribute to the overall relaxation (T_1), as mentioned previously, inner-sphere interactions are most frequently considered in the design of contrast agents, since the relevant variables are more straightforward to theoretically understand and modify. As expressed in equation (3), the inner-sphere relaxation rate is proportional to the aquation number q (number of water molecules directly bound to the metal ion) and the mole fraction of bound water nuclei (P_m), which is directly proportional to the concentration of contrast agent.³⁰ T_{1m} refers to the relaxation rate enhancement of inner-sphere water protons. The mean residence lifetime of bound water molecules (τ_m) also influences the relaxation rate. The term T_{1m} is further divided into two pathways through dipole-dipole (DD) and scalar or contact (SC) mechanisms as shown in equation (4). The relaxation rates of both mechanisms are directly proportional to the effective magnetic moment (μ_{eff}) of the metal ion and also defined by correlation time τ_{c1} and τ_{e1} , respectively. Accordingly, equations (5) and (6) describe the contributing factors to correlation time τ_{c1} and τ_{e1} where T_{1e} represents the electronic longitudinal relaxation time, which is field dependent, and τ_R is the rotational correlation time of

the metal complex.^{30,35} By tuning these parameters researchers are able to change the relaxivity of contrast agents. The detection of redox-responsive species can be achieved by designing contrast agents that will have different q , μ_{eff} , or τ_{R} in certain redox environments.³⁸

$$1/T_1^{\text{IS}} = qP_{\text{m}}/(T_{1\text{m}} + \tau_{\text{m}}) \quad (3)$$

$$1/T_{1\text{m}} = 1/T_1^{\text{DD}} + 1/T_1^{\text{SC}} \quad (4)$$

$$1/\tau_{\text{cl}} = 1/T_{1\text{e}} + 1/\tau_{\text{m}} + 1/\tau_{\text{R}} \quad (5)$$

$$1/\tau_{\text{el}} = 1/T_{1\text{e}} + 1/\tau_{\text{m}} \quad (6)$$

1.5.1 Magnetism-Based Redox-Responsive MRI Contrast Agents

According to equation (3), when the water exchange rate is fast enough for τ_{m} to be negligible compared with $T_{1\text{m}}$, the overall longitudinal relaxation rate will be solely dependent on $T_{1\text{m}}$, q and P_{m} . Since $T_{1\text{m}}$ scales with the magnetic moment, one strategy for a redox-responsive MRI contrast agent is to have its paramagnetism change upon reacting with an oxidant or reductant. This can be achieved by either switching the oxidation state of the paramagnetic reporter or forming a polynuclear metal complex.⁴⁰⁻⁴³

Hypoxia is a term that refers to oxygen deficiency.⁴⁴ The concentration of oxygen appears to be relevant in certain pathological conditions, and numerous techniques have been developed to image local concentrations of O_2 .^{45, 46} Some O_2 -triggered MRI contrast agents are predicated on the simple idea of altering oxidation state of the metal center.^{40, 41, 95} Since the lanthanide metal ions commonly used for MRI contrast, such as gadolinium and europium, don't have multiple oxidation states that are stable under biological conditions, transition metals, such as manganese and cobalt, have been used instead.³⁹ Aime and coworkers synthesized a manganese-based porphyrin complex (Mn^{II} tpps) that oxidizes to a Mn(III) species upon reaction with O_2 .⁴⁰ Poly-cyclodextrin (poly- β -CD) was used to encapsulate a manganese porphyrin

complex through strong non-covalent interactions between the phenyl rings on the porphyrin ligand and cyclodextrin; the encapsulation prevents the dimerization of individual porphyrin moieties.⁴⁷ The relaxivity is further enhanced by the slower rotational motion (τ_R) resulting from the attachment of the Mn(II) complex to cyclodextrin. Poly-cyclodextrin was selected instead of the monomer for its larger effect on the rotational correlation time (τ_R) and its better stability.⁴⁸ It was found that the proton relaxation rate (r_1) decreases almost linearly as the O_2 concentration increases.

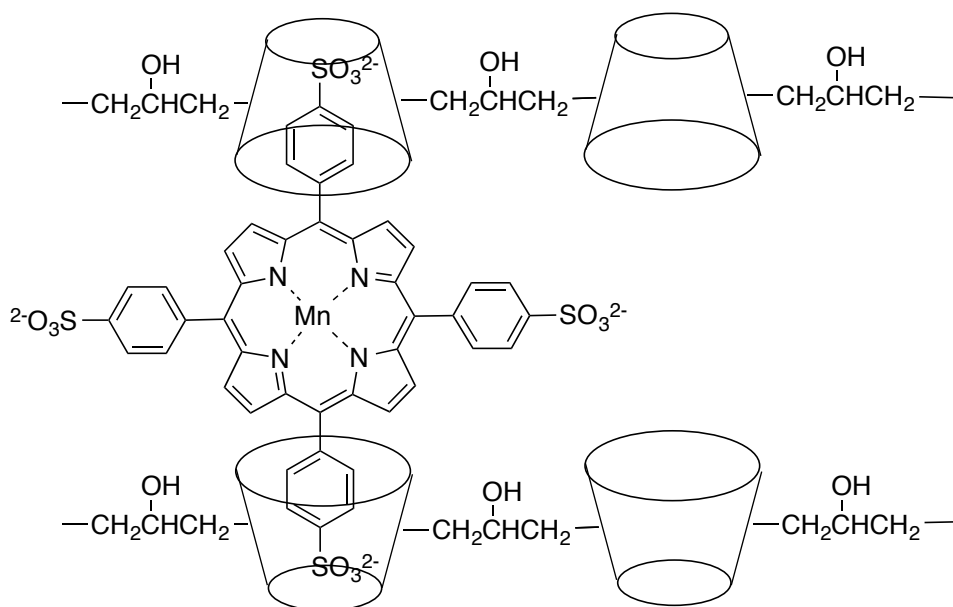


Figure 1.2 Schematic demonstration of supramolecular adduct between Mn^{II} tpps and poly- β -CD. Notice that one manganese porphyrin complex can bind with two cyclodextrin units at the same time.

Caravan and his group reported a manganese-based MRI contrast agent using the similar strategy.⁴¹ The HBET ligand contains three carboxylate groups and one phenolate group; these donor atoms can stabilize both the +2 and +3 oxidation states of manganese. Although the ligand features an acyclic structure that is less kinetically and thermodynamically stable compared to more commonly used cyclen and porphyrin derivatives, the complexes are adequately stable

under biological conditions. The Mn(III/II) redox potential was measured to be 356 mV (vs. NHE), allowing the probe to be oxidized and reduced by the biologically relevant H_2O_2 and glutathione, respectively. Upon reaction with two equivalents of H_2O_2 , approximately 70% of the Mn^{II} -HBET complex is oxidized to Mn^{III} -HBET within 4 min. This process can be reversed by adding glutathione (GSH). The individual T_1 relaxivities for Mn^{II} -HBET and Mn^{III} -HBET were measured to be 2.76 and 1.05 $\text{mM}^{-1} \text{s}^{-1}$ under a 1.4 T magnet. The Mn^{III} -HBET complex is still quite paramagnetic with $S = 2$. Although the paramagnetism is less than Mn^{II} -HBET ($S = 5/2$), it does not seem sufficient to explain the large change in relaxivity. The large relaxivity difference was also attributed to the presence of an inner-sphere bound water molecule for Mn^{II} -HBET that is lost upon its oxidation to a hexacoordinate Mn(III) complex.⁴¹

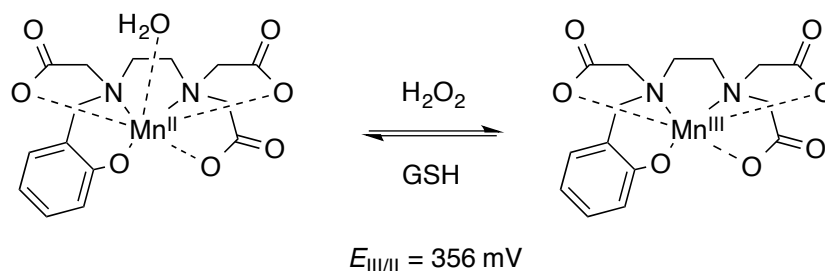


Figure 1.3 Structural representation of Mn^{II} -HBET and Mn^{III} -HBET complexes. Oxidation state of metal ion can be tuned by reacting with H_2O_2 and glutathione (GSH).

A gadolinium-based MRI contrast agent (5-HT-DOTA(Gd), Fig. 1.4) was synthesized by Weissleder and coworkers.⁴² The 5-hydroxytryptamide moiety will react with H_2O_2 in the presence of myeloperoxidase (MPO) and polymerize to form oligomers that are more paramagnetic than the monomeric form. Using glucose/glucose oxidase as the hydrogen peroxide source, it was observed that the r_1 increase by 30% and r_2 increase by 20% over 24 h. Weissleder speculated that 5-HT-DOTA(Gd) can be used for the specific detection of MPO enzyme activity.

Using the contrast agent for H₂O₂ detection is complicated by the fact that MPO has to be present as a co-analyte.

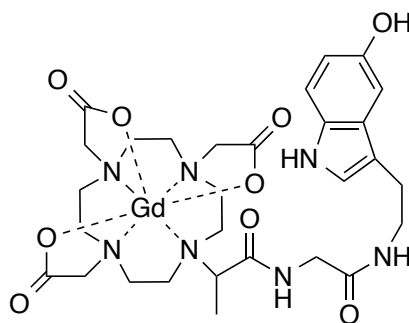


Figure 1.4 Structural demonstration of glycylylmethyl DOTA(Gd) 5-hydroxytryptamide (5-HT-DOTA(Gd), DOTA = 1,4,7,10-tetraazacyclododecane-1,4,7,10-tetraacetic acid).

Goldsmith's group recently reported a mononuclear manganese complex Mn^{II}-Htp1 capable of signaling H₂O₂ (Chapter 2).⁴³ The hexadentate Htp1 ligand contains three pyridine rings and one *para*-methylphenol group as shown in Fig. 1.5a. The manganese complex Mn^{II}-Htp1 dimerizes in the presence of excess H₂O₂. In this reaction, two mononuclear species link together through a new C-C bond that forms between the *ortho* carbons on the phenols. The oxidation state of the metal remains +2 (Fig. 5b). As anticipated, the dimerized product exhibits lesser paramagnetism per manganese unit (4.5 μ_B) compared to the monomer (5.8 μ_B).⁴⁹ Under a 3 T magnetic field provided by a clinical MRI scanner, the longitudinal relaxivity (*r*₁) was measured to be 4.39 mM⁻¹s⁻¹ for the monomeric form and 3.59 mM⁻¹s⁻¹ (per Mn) after the reaction with H₂O₂. Despite the relatively small relaxivity difference (0.8 mM⁻¹s⁻¹) and decrease (18%) in signal, the Mn(II) complex is notable for being able to directly and rapidly detect H₂O₂. Additionally, the Mn^{II}-Htp1 complex does not require a second analyte to catalyze the reaction and the Mn(II) center not only serves as a paramagnetic reporter but also facilitates the dimerization given that the ligand itself does not react with H₂O₂. The likely mechanism is that the H₂O₂ oxidizes Mn(II) to Mn(III). The transient Mn(III) intermediate captures an electron

from the phenol group to generate a phenoxy radical that can delocalize and reacts with another radical to give the product. The compound is also remarkable in that it exhibits excellent stability in aqueous and aerobic conditions; this is critical for the selective detection of H₂O₂ over O₂.

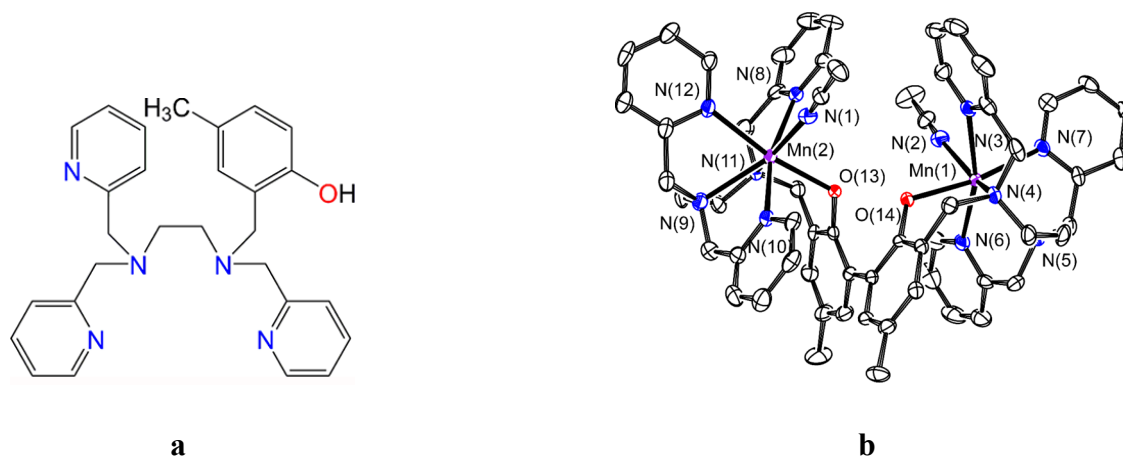


Figure 1.5 a, Ligand structure of Mn^{II}-Htp1. **b**, ORTEP representation of binuclear product [Mn₂(Htp1₂)(MeCN)₂]³⁺. Counteranions, hydrogen atoms and noncoordinated solvent molecules are omitted for clarity.⁴³

1.5.2 Hydration Number-Based Redox-Responsive MRI Contrast Agents

The relaxation rate is directly proportional to the number of bound water molecules (q), and increasing the q through redox-activated structural changes to the ligand is an alternative means to obtain a turn-on sensor. The major disadvantage is that increasing the hydration number by reducing the number of donor atoms from the ligand necessarily destabilizes the complex.³⁰ Other difficulties include tuning the magnitude of the spectroscopic response and ensuring that the metal does not get oxidized or reduced to a less paramagnetic form or to one that binds too weakly to the remaining donor atoms. Research has been focused on the development of highly hydrated MRI contrast agents with high relaxivity and excellent stability against transmetalation and decomposition.⁵⁰⁻⁵² In 2004, Meade's group reported an enzyme-responsive gadolinium contrast agent (α/β -EGadMe) that signals the analyte through an

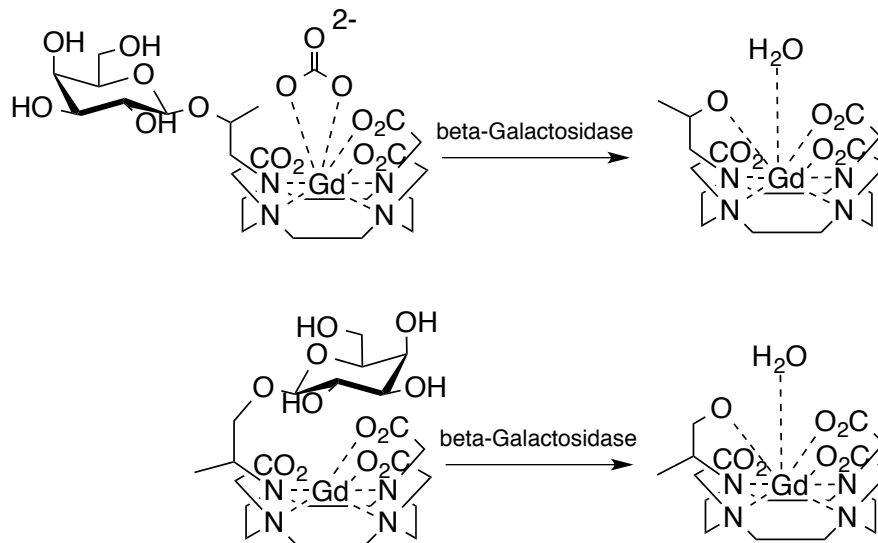
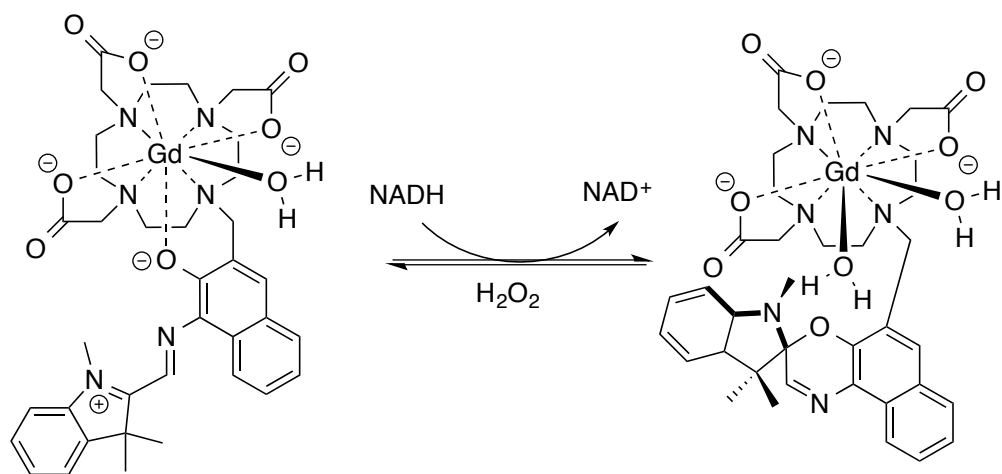


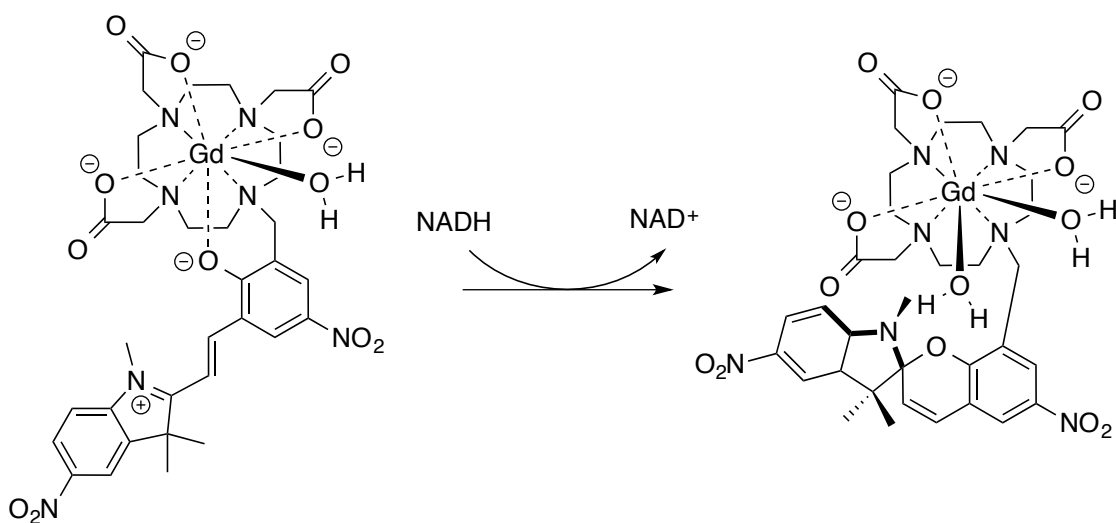
Figure 1.6 Schematic representations of proposed mechanisms of activation by β -galactosidase for β -EGadMe (first) and α -EGadMe (second).

increase in q .⁵³ Using DO3A (1,4,7-tricarboxymethylene-1,4,7,10-tetraazacyclododecane) as the parent ligand, a galactopyranose moiety was connected to the macrocycle by a two-carbon linker. The linkage can be cleaved in the presence of bovine liver β -galactosidase to yield 2-aminoethyl-GdDO3A (Fig. 1.6). The *R* and *S* isomers of β -EGadMe and the racemate of α -EGadMe were synthesized and characterized. The name α/β derives from the position of methyl group on the two-carbon linker. For the β -EGadMe compound shown in Fig. 1.6, Meade proposed that exogenous carbonate coordinates to the metal center as a bidentate ligand, resulting in an overall hydration number $q = 0$.⁵⁴ After cleavage by β -galactosidase, the hydroxyl group remaining from the sugar replaces the carbonate that allows an inner-sphere water to interact with Gd(III) accordingly ($q = 1$).⁵⁵ With the α -EGadMe isomer, conversely, the pendant galactopyranose group sterically blocks the water molecules from accessing the metal center and enzymatic cleavage allows the access. Though the MRI contrast agents here are not redox-responsive MRI sensors, they elegantly illustrate the hydration-number based strategy.

Louie's group reported the gadolinium contrast agent illustrated in Fig. 1.7a.⁵⁶ In this responsive contrast agent, the spironaphthoxazine molecule was attached to the Gd(DO3A) subunit. The complex exhibits a r_1 value of $(5.58 \pm 0.36) \text{ mM}^{-1} \text{ s}^{-1}$ with $q = 1.26 \pm 0.03$, slightly higher than that of Gd(DOTA) ($q = 1.1$), which was attributed to the weaker coordinating ability of the phenolate anion. Louie hypothesizes that the electrostatic interaction between Gd(III) and phenolate hinders the cyclization of the spironaphthoxazine moiety and stabilizes the acyclic structure.⁵⁷ After reaction with NADH, a key biological reducing agent, the spironaphthoxazine cyclizes to form a product with enhanced longitudinal relaxation $r_1 = 8.60 \pm 0.74 \text{ mM}^{-1} \text{ s}^{-1}$ and a higher hydration number ($q = 2.01 \pm 0.05$). The higher q results from the replacement of the phenolate oxygen by a water molecule. A more detailed mechanism for the relaxivity increase remains elusive. The cyclization process also disrupts the π -conjugated system, quenching the fluorescence of the spironaphthoxazine. The reduction can be reversed by H_2O_2 to restore the T_1 relaxation time and a portion of the fluorescence. The contrast agent displays a good relaxivity response to NADH (54%) and good biological compatibility in cell cultures. A similar example was reported using the slightly different ligand structure shown in Fig. 1.7b.⁵⁸ In this case, the open-ring isomer can cyclize to form the dinitrospiropyran product irreversibly in the presence of either NADH or visible light. The strong electron withdrawing nitro groups favor the closed-ring isomer thermodynamically.⁵⁸ In the closed-ring form, the spiropyran ring acts as an "indoline cap" and prevents water molecules from accessing the metal center.⁵⁸ As a result, the relaxivity decreases by 26% after adding NADH.



a



b

Figure 1.7 a. Transformation of complex between acyclic and cyclic forms triggered by NADH and H_2O_2 . **b.** Conversion of the open-ring form to spiropyran isomer by NADH.

Utilizing the same strategy, an O_2 -sensitive Gd(III) contrast agent was synthesized by Nagano's group.⁵⁹ Nitro groups are commonly used for redox-responsive sensing for their facile reduction to amino groups by nitroreductase under biological conditions. Represented in Fig. 1.8, complex $4\text{NO}_2\text{MeOSAGd}$ (Gadolinium(III) 1-[2'-(2-methoxy-4-nitrophenylsulfonylamino)ethyl]-4,7,10-tris(carboxymethyl)-1,4,7,10-tetraazacyclododecane) incorporates a

nitrobenzenesulfonamide moiety as the functional unit. Under biological conditions ($\text{pH} = 7.4$), the amide group will deprotonate and bind to the Gd(III) due to the strong electron-withdrawing capability of the nitro group. Under hypoxia, the nitro group can be reduced by nitroreductase to an electron-donating amino group.⁶⁰⁻⁶² As a consequence, the protonated amine group vacates a coordination site on the metal center, allowing an additional inner-sphere water and increasing the relaxivity. Nagano found that the r_1 relaxivity of $4\text{NO}_22\text{MeOSAGd}$ and its reduced form $4\text{NH}_22\text{MeOSAGd}$ are 2.1 and $3.6 \text{ mM}^{-1} \text{ s}^{-1}$, respectively, indicating a 1.8 fold relaxivity increase.

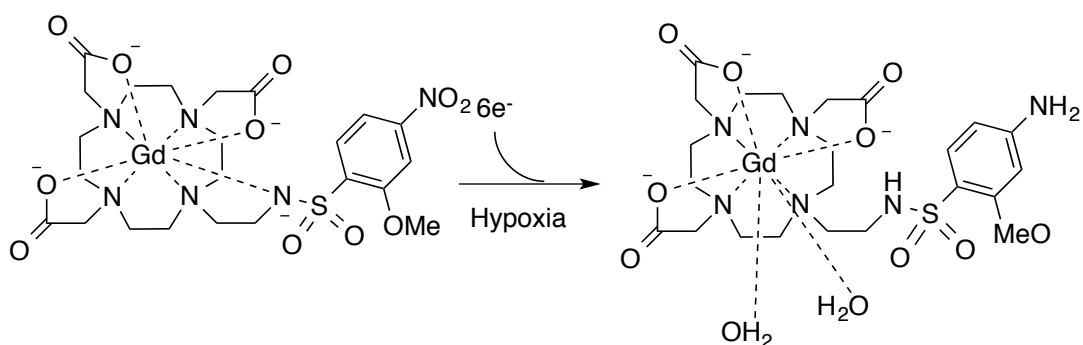


Figure 1.8 $4\text{NO}_22\text{MeOSAGd}$ reduced to $4\text{NH}_22\text{MeOSAGd}$ under hypoxia.

More recently, our group reported a Mn(II)-based MRI contrast agent ($\text{MnH}_2\text{qtp1}$) that is capable of detecting H_2O_2 through a relaxivity (r_1) increase (Chapter 3).⁶³ A quinol moiety is used as the redox-responsive unit. The Mn(II) complex is heptacoordinate according to the crystal structure with one coordinating MeCN molecule that can be displaced by water in aqueous solution. In the presence of H_2O_2 , the Mn(II) facilitates the oxidation of the quinol into a *para*-quinone that has weaker donating capability compared to a hydroxyl group (Fig. 1.9). Consequently, the H_2O_2 -induced structural change allows this portion of the ligand to be more readily displaced by water, increasing q and the relaxivity (r_1) from $4.73 \text{ mM}^{-1} \text{ s}^{-1}$ to $5.30 \text{ mM}^{-1} \text{ s}^{-1}$. We speculated that the quinol oxidation process is reversible based on experimental observations that may account for the small relaxivity increase. Despite the modest relaxivity

change ($0.8 \text{ mM}^{-1} \text{ s}^{-1}$), the compound shows promise in that it exhibits SOD activity that is comparable to those manganese porphyrin SOD mimics.⁶⁴ The complex and its variants could therefore potentially image and simultaneously treat oxidative stress.

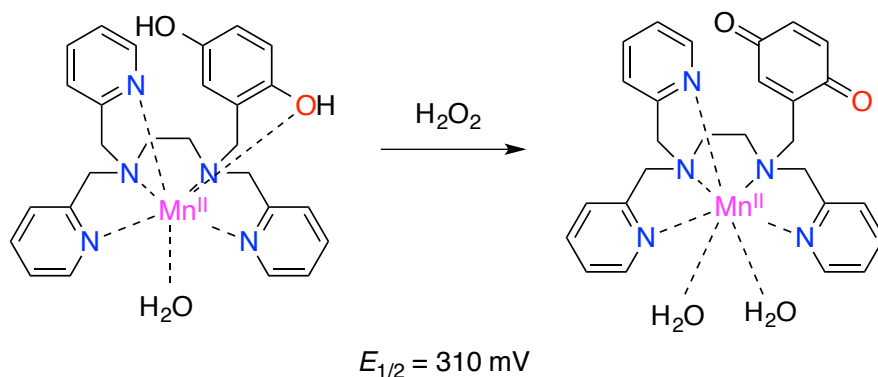


Figure 1.9 Proposed mechanism for H_2O_2 detection by $\text{MnH}_2\text{qtp1}$.

Disulfide bond linkage is commonly exploited in responsive MRI. Aime's group reported a Gd(III) based contrast agent (Gd-DO3AS-Act, Fig. 1.10) that signals the presence of thiol-containing compounds through changes in q .⁶⁵ Using DO3A as the parent ligand, a flexible linker with a terminal 2-pyridyl-dithio group was introduced. Upon reacting with thiols, the 2-pyridyl-dithio group can promptly form a disulfide bond and release 2-pyridine-thione as byproduct.⁶⁶ In the presence of glutathione, which contains abundant thiol groups, the adduct between glutathione and Gd(III) complex (Gd-DO3AS-SG) forms via a disulfide bond. As a consequence, the hydration number reduced from 2 to 1 due to the coordination of carboxylate group from the glutathione that is reflected by a significant drop in r_1 from $8.1 \text{ mM}^{-1} \text{ s}^{-1}$ to $4.1 \text{ mM}^{-1} \text{ s}^{-1}$.⁶⁷⁻⁶⁹ Moreover, the addition of β -cyclodextrin tends to enhance the relaxivity difference by restricting rotational mobility resulting from the favorable non-covalent interaction between β -CD and Gd-DO3AS-Act that is absent for the adduct.

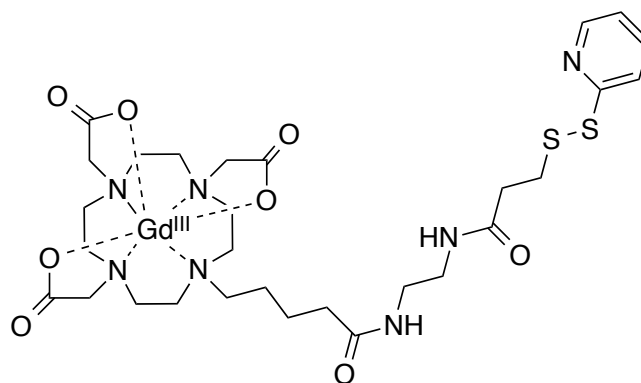


Figure 1.10 Structure of Gd-DO3AS-Act.

Almutairi and coworkers have developed a novel strategy for redox-responsive MRI contrast agents using polymer encapsulated ultrasmall gadolinium oxide nanoparticles.⁷⁰ Encapsulating Gd_2O_3 nanoparticles (NPs) with a hydrophobic polymer hinders both the inner-sphere and outer-sphere water interactions, resulting in a minimal T_1 -weighted signal (“OFF” state) (Fig. 1.11). Upon degradation of the polymer, the Gd_2O_3 nanoparticles are exposed to the

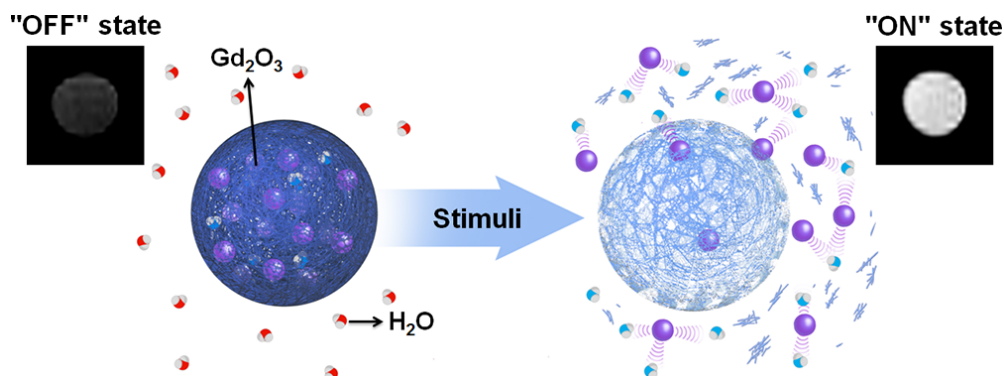


Figure 1.11 Schematic representation of the encapsulated Gd_2O_3 NPs “turned on” through polymer degradation.⁷¹

aqueous environment, with a concomitant strong signal increase (“ON” state). Using responsive polymers sensitive to various biological conditions such as pH or ROS (H_2O_2) produces responsive MRI contrast agents that are responsive to a wide array of analytes. For H_2O_2 detection, a polyester containing boronic ester groups that degrade upon exposure to H_2O_2 was

employed.⁷¹ The r_1 relaxivity is extremely low after encapsulation ($0.5 \text{ mM}^{-1} \text{ s}^{-1}$). In the presence of H_2O_2 (0-100 mM), a relaxivity increase as high as 11-fold was obtained.

1.5.3 Tumbling Rate-Based Redox-Responsive MRI Contrast Agents

Rotation, or the lack thereof, can strongly impact the relaxivity.³⁰ According to equation (5), the effective correlation time τ_{ci} is closely related with the rotational correlation time (τ_R) and various strategies have been developed to reduce the tumbling rate for better relaxivity. It is well known that suitable functionalized Gd-based contrast agents exhibit enhanced relaxivity in the presence of human serum albumin (HSA) due to higher τ_R resulting from non-covalent interactions between the protein and small molecule.^{72,73} Moreover, serum albumin, cysteine, and glutathione contain thiol groups capable of reversibly forming disulfide linkages to other thiols under oxidizing conditions (Fig. 1.12).⁷⁴ As a result, the change in relaxation time can reveal details about the local redox-environment, albeit indirectly, and the sensitivity correlates to the number of thiol groups on the target analyte. Furthermore, studies have shown that the length of thiol containing side chain in the ligand determines whether the binding mode is single-site or multisite and the binding constant decreases upon introduction of homocysteine as a competitive species.

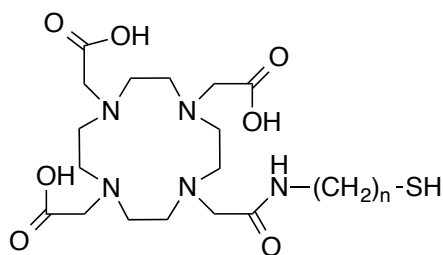


Figure 1.12 DOTA derivatives bearing thiol groups ($n = 3-9$).

Botta's group reported perthiolated β -cyclodextrin (β -CD)-based nanocapsules containing Gd(III) complexes as redox-responsive probes.⁷⁵ The β -CD units are linked together by disulfide bonds and the ligand of the encapsulated Gd(III) complexes contains a hydrophobic benzyl

moiety that fits into the cavity of β -CD units through non-covalent interaction.⁷⁶⁻⁷⁸ As expected, the nanocapsules exhibit a high longitudinal relaxivity ($r_1 = 19.3 \text{ mM}^{-1} \text{ s}^{-1}$, 4.7 T), which is substantially larger than the Gd(III) complex itself ($r_1 = 7.3 \text{ mM}^{-1} \text{ s}^{-1}$) and can be attributed to reduced tumbling. The high relaxivity also indicates the good water permeability of the macrostructure. In the presence of the reductant TCEP (tris(2-carboxyethyl)phosphine),⁷⁹ the disulfide bonds between β -CD units cleave to decompose the particles into smaller fragments, releasing the Gd(III) complexes with a concomitant decrease in relaxivity within a few hours. The decrease in r_1 is attributed to faster molecular tumbling (Fig. 1.13).

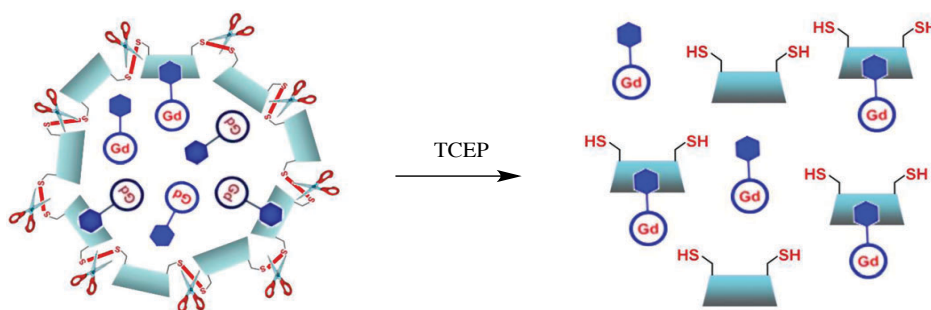


Figure 1.13 Schematic demonstration of Gd(III) complex included nanocapsules decompose through disulfide bond cleavage under reducing condition.⁷⁵

1.6 CEST-Derived Redox-Responsive MRI Contrast Agents

Chemical exchange saturation transfer (CEST) is an attractive complementary method to traditional relaxivity-based MRI contrast. CEST contrast agents generally possess protons that are in equilibrium with those from the bulk solvent water molecules. CEST contrast is achieved by applying a suitable MR radiofrequency to selectively saturate one of these exchangeable protons. After chemical exchange, the saturated magnetization will be transferred to the bulk water and the MR signal of water will subsequently decrease.^{80,81} Compared with T_1/T_2 -weighted MRI contrast techniques, CEST MRI is relatively insensitive and often requires high concentration of contrast agents and fast proton exchange in order to maximize the saturation

transfer to bulk water.³⁷ Although diamagnetic compounds can lead to CEST, paramagnetic CEST (PARACEST) contrast agents, including lanthanide or transition metal complexes are often used to maximize the energy gap between the water and exchangeable proton resonance frequencies. These ions shift the MR frequencies of the exchangeable protons, and the difference compared to the MR frequency of bulk water is called “chemical shift”. An important criterion for CEST contrast is that the water exchange rate constant between proton pools (k_{ex}) should be slower than the chemical shift between them ($\Delta\omega$). Large exchange rate constants lead to better CEST signals, and larger chemical shift in MR frequency facilitates CEST.⁸² Furthermore, a large chemical shift ($\Delta\omega$) minimizes the interference from magnetization transfer effect (MT) of tissue background.^{83,84} Normally, the CEST signal is described by the percent decrease of the bulk water signal intensity. The net magnetization (M_z/M_0) of water protons under steady state is given by equation (7), which assumes complete saturation of the exchangeable proton pool.^{82,83} c represents the concentration of CEST agent, q is the number of exchangeable protons (either from bound inner-sphere water or -NH, -OH groups with exchangeable protons), 55.5 corresponds to the molar concentration of water, T_1 is the longitudinal relaxation time of bulk water and τ_m corresponds to the chemical lifetime of the exchangeable proton ($1/\tau_m = k_{ex}$). Rational design of redox-responsive PARACEST agents can be achieved through incorporating protic groups like amines and alcohols with exchangeable protons that can be modified to display different chemical shift and exchange rates. Additionally, the electronic properties of the ligand and coordination geometry are critical determinants for τ_m when PARACEST agents contain bound water molecules with slow exchange rates.⁸⁵⁻⁸⁸ When the longitudinal relaxation time (T_1) of bulk water is shorter than τ_m at the exchangeable site, the magnetization will no

longer be saturated, attenuating the CEST effect.⁸⁹ Here, we divide redox-responsive PARACEST agents into two major categories: ligand-based and metal-based.

$$M_z/M_0(\%) = 100 (1 + cqT_1/55.5\tau_m)^{-1} \quad (7)$$

1.6.1 Ligand-Based Redox-Responsive PARACEST Agents

Sherry's group recently reported a Eu(III)-based PARACEST agent containing the NAD⁺/NADH mimic *N*-methylquinolinium moieties as the redox-responsive unit.⁸⁸ In the presence of β -NADH, the *N*-methylquinolinium moieties on the amide side arms can be reduced to dihydroquinoline. This changes the coordination environment around Eu(III) and thereby alters the exchange rate of the bound water molecule ($1/\tau_m$) (Fig. 1.14).⁸⁵⁻⁸⁷ According to the CEST spectra, the bound water molecule exhibits slower water exchange rate and larger chemical shift ($\Delta\omega$) after reduction. An analogous compound with two *N*-methylquinolinium moieties has a larger increase in signal intensity upon reduction (2% to 15%). The CEST signal for the oxidized form also displays an unusual dependence on pH.⁸³ The CEST peak for the Eu(III)-bound water broadens as the pH increases from 5 to 8. The author explained that the higher pH facilitates the deprotonation of amide NH group connected to the strong electron-withdrawing *N*-methylquinolinium group and thereby enhances the water exchange rate (k_{ex}).

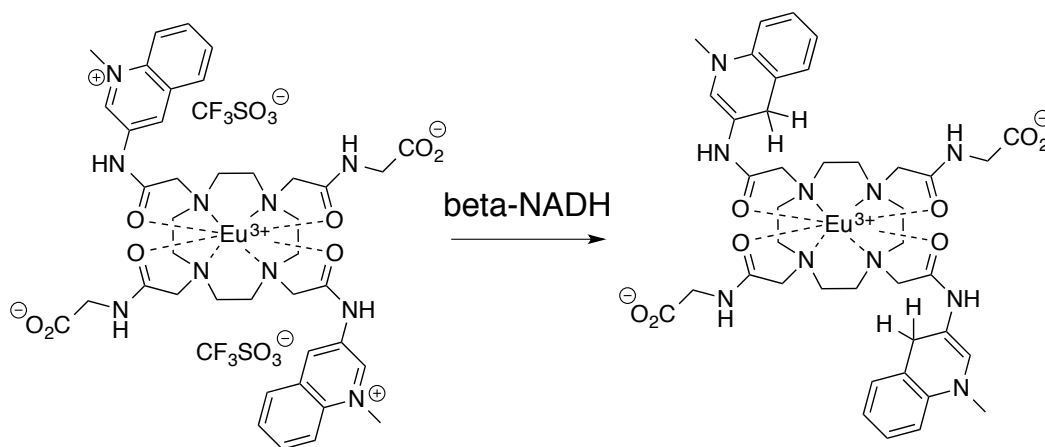


Figure 1.14 Representation of structural change induced by β -NADH.

The CEST signal intensity can also be tuned by changing the longitudinal relaxation time (T_1) of bulk water, although this approach is less common.⁹⁰ Nitroxides are persistent organic free radicals that can shorten the T_1 relaxation time of water. Nitroxides are commonly used as electron-spin resonance (ESR) probes for monitoring the redox status of tissues through either oxidation or reduction into diamagnetic species that are ESR silent.⁹¹ Incorporating two nitroxide radical groups into the ligand structure can effectively quench the CEST signal due to the shortening of T_1 according to equation (7). As expected, the nitroxide containing Eu(III) PARACEST agent exhibits only approximately 2% CEST signal with $T_1 = 0.2$ s at pH 7, 25 °C, 9.4 T. Adding 2 equiv. of L-ascorbic acid reduces the nitroxides to diamagnetic hydroxylamines, and the T_1 returns to its normal value (2.6 s). The CEST signal increases to ~20% while the water exchange lifetime (τ_m) remains essentially the same (85 μ s before, 81 μ s after). A similar experiment was conducted *in vivo* using bladder (organ that collects urine excreted by the kidneys), and the same CEST signal enhancement was observed after introducing L-ascorbic acid. The LnDOTA-tetra(amide nitroxide) derivatives therefore demonstrate a strategy to modify the CEST signal by T_1 relaxation time of bulk water and can potentially be used as redox-responsive PARACEST probes for imaging redox environments in biological samples.

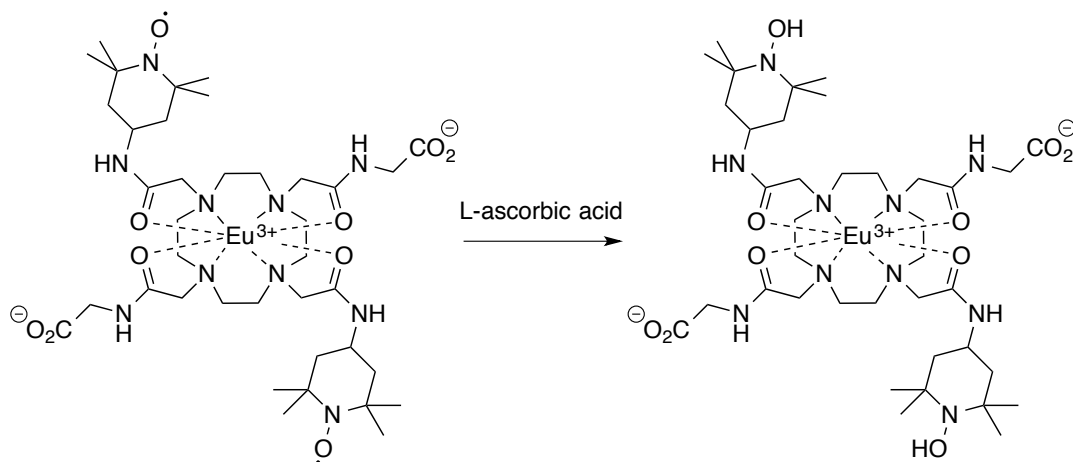


Figure 1.15 Reduction of nitroxide radical groups to hydroxylamines by L-ascorbic acid.

Liposomes have high water contents. The intraliposomal water molecules undergo limited exchange with extraliposomal water. When loaded with paramagnetic species containing lanthanide ions, selective saturation of the intraliposomal water resonance using the appropriate radiofrequency can decrease the CEST signal of extraliposomal water through chemical exchange. CEST agents based on liposomes have been made that have high sensitivity relative to more common CEST agents.⁹² After attaching Gd(III) complexes to the surface of liposome that significantly shortens the relaxation time (T_1), the CEST signal is quenched in a similar manner resembling the previous nitroxide example. Aime's group reported a lipoCEST agent that contains 3-(2-pyridyl)-dithio-propionate moieties at the end of polar head on the bilayer lipid that allows the attachment of Gd^{III}DOTA derivative through a disulfide (-S-S-) linkage (Fig. 1.16).⁸⁹ In the presence of the reducing agent TCEP, the disulfide bond was cleaved to release the Gd(III) complex and regenerate the CEST signal. Additionally, the probe can be modified for other applications beyond imaging redox status by tuning the activable linkage for various analytes.

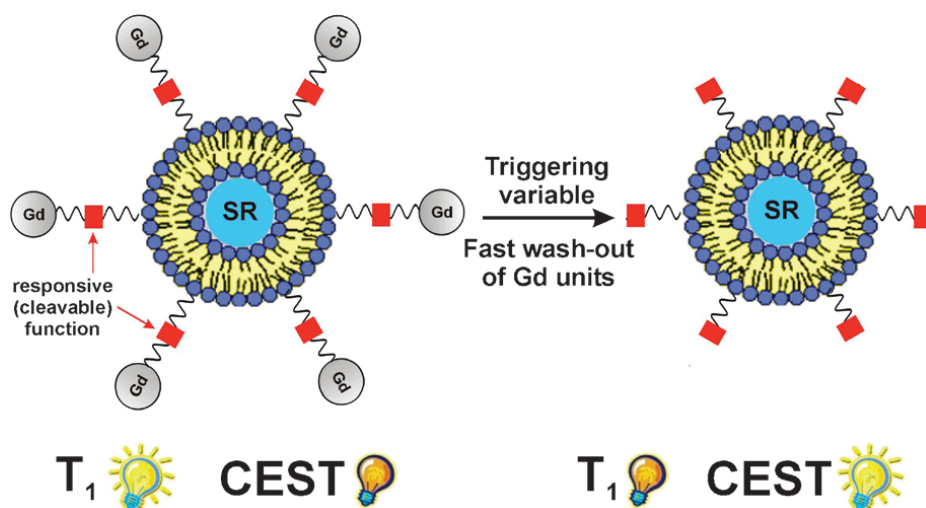


Figure 1.16 Mechanistic demonstration of responsive lipoCEST agent triggered by cleavage between the lipid core and Gd(III) complex (SR: paramagnetic Shift Reagent).⁸⁹

1.6.2 Metal-Based Redox-Responsive PARACEST Agents

Ligand-based redox-sensitive PARACEST agents generally contain lanthanide ions as the metal center for their magnetic properties and have a small influence on the longitudinal relaxation time of bulk water. Metal-based redox-sensitive PARACEST can be achieved by manipulating the oxidation states or spin states of the metal center; this requires that the metal ion possess multiple accessible oxidation states in aqueous conditions and precludes the use of lanthanides. However, certain transition metals, such as manganese, result in large line-broadening that renders the data analysis difficult, if not impossible. Morrow's group has explored several Ni^{2+} and Fe^{2+} complexes as potential PARACEST agents^{93, 94} and more recently reported a redox-activated cobalt complex that can switch between paramagnetic and diamagnetic states.⁹⁵ Specifically, TPT (1,4,7-tris(pyrazol-3-ylmethyl)-1,4,7-triazacyclononane) is a hexadentate ligand based on TACN (1,4,7-triazacyclononane) with three pyrazole pendant arms bearing NH groups with exchangeable protons. The $[\text{Co}(\text{TPT})]^{2+}$ complex contains a high-spin ($5.7 \pm 0.2 \mu_{\text{B}}$) octahedral Co(II) ion with three unpaired electrons and exhibits low T_1 and T_2 relaxivity (0.093 and $0.50 \text{ mM}^{-1} \text{ s}^{-1}$, respectively). This low relaxivity is ideal for PARACEST contrast. Notably, $[\text{Co}(\text{TPT})]^{2+}$ displays a sharp CEST signal at 135 ppm, which is assigned to the pyrazole NH protons based on NMR. The chemical shift ($\Delta\omega = 135 \text{ ppm}$) is the largest reported to date for transition metal PARACEST agents and greatly minimizes background noise from the interference of tissue magnetization transfer effects.⁸³ Not surprisingly, the CEST signal intensity exhibits a pH dependence that reaches its maximum at pH 6.9 due to base-catalyzed proton transfer. Further increasing the pH beyond 6.9 broadens the signal resulting from fast proton exchange rate (k_{ex}). Upon exposure to O_2 , the $[\text{Co}(\text{TPT})]^{2+}$ slowly oxidizes to $[\text{Co}(\text{TPT})]^{3+}$ with a second-order rate constant of $0.43 \text{ M}^{-1} \text{ s}^{-1}$. The Co(III) species is low-spin and has no CEST signal due to its diamagnetism (Fig. 1.17). The addition of a reducing agent such as

sodium dithionite or L-cysteine restores the CEST signal, consistent with reducing Co(III) back to Co(II). Furthermore, the cyclic voltammetry of $[\text{Co}(\text{TPT})]^{2+}$ exhibits a reversible feature with moderate negative potential (-107 ± 11 mV vs. NHE), which is amenable for oxidation and reduction by physiologically relevant species.⁹⁶

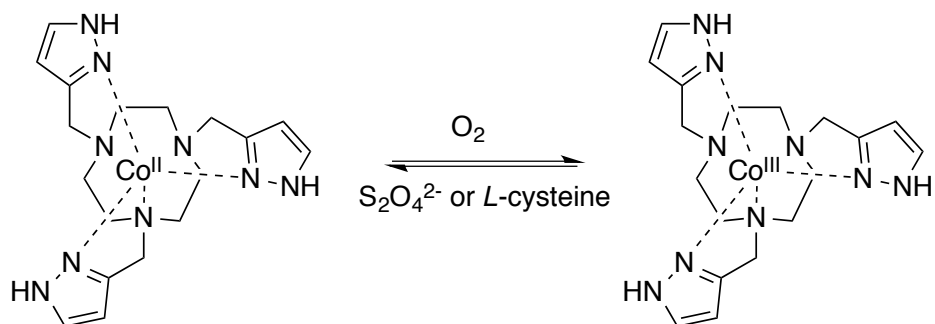


Figure 1.17 Structure of $[\text{Co}(\text{TPT})]^{2+}/[\text{Co}(\text{TPT})]^{3+}$ complexes.

References

- (1) Buttke, T. M.; Sandstrom, P. A. *Free Radical Res.* **1995**, *22*, 389–397.
- (2) Serrano, F.; Klann, E. *Ageing Res. Rev.* **2004**, *3*, 431–443.
- (3) Sundaresan, M.; Yu, Z. X.; Ferrans, V. J.; Irani, K.; Finkel, T. *Science* **1995**, *270*, 296–299.
- (4) Lyle, A. N. *Physiology* **2006**, *21*, 269–280.
- (5) Rhee, S. G. *Science* **2006**, *312*, 1882–1883.
- (6) Mosley, R. L.; Benner, E. J.; Kadiu, I.; Thomas, M. *Clin. Neurosci. Res.* **2006**, *6*, 261–281.
- (7) Fearon, I. M.; Faux, S. P. *J. Mol. Cell. Cardiol.* **2009**, *47*, 372–381.
- (8) Roberts, C. K.; Sindhu, K. K. *Life Sciences* **2009**, *84*, 705–712.
- (9) Gladden, J. D.; Ahmed, M. I.; Litovsky, S. H.; Schiros, C. G.; Lloyd, S. G.; Gupta, H.; Denney, T. S., Jr.; Darley-Usmar, V.; McGiffin, D. C.; Dell'Italia, L. J. *Am. J. Med. Sci.* **2011**, *342*, 114–119.
- (10) Eskici, G.; Axelsen, P. H. *Biochemistry* **2012**, *51*, 6289–6311.
- (11) Chan, J.; Dodani, S. C.; Chang, C. J. *Nature Chem.* **2012**, *4*, 973–984.
- (12) Lippert, A. R.; Van de Bittner, G. C. *Acc. Chem. Res.* **2011**, *44*, 793–804.
- (13) Chang, M.; Pralle, A.; Isacoff, E. Y. *J. Am. Chem. Soc.* **2004**, *126*, 15392–15393.
- (14) Lo, L. C.; Chu, C. Y. *Chem. Commun.* **2003**, *21*, 2728–2729.
- (15) Miller, E. W.; Tulyanthan, O.; Isacoff, E. Y.; Chang, C. J. *Nat. Chem. Biol.* **2007**, *3*, 263–267.
- (16) Du, L.; Li, M.; Zheng, S.; Wang, B. *Tetrahedron Lett.* **2008**, *49*, 3045–3048.
- (17) Dickinson, B. C.; Huynh, C.; Chang, C. J. *J. Am. Chem. Soc.* **2010**, *132*, 5906–5915.

- (18) Karton-Lifshin, N.; Segal, E.; Omer, L.; Portnoy, M.; Satchi-Fainaro, R.; Shabat, D. *J. Am. Chem. Soc.* **2011**, *133*, 10960–10965.
- (19) Abo, M.; Urano, Y.; Hanaoka, K.; Terai, T.; Komatsu, T.; Nagano, T. *J. Am. Chem. Soc.* **2011**, *133*, 10629–10637.
- (20) Koide, Y.; Urano, Y.; Kenmoku, S.; Kojima, H.; Nagano, T. *J. Am. Chem. Soc.* **2007**, *129*, 10324–10325.
- (21) Lim, M. H.; Xu, D.; Lippard, S. J. *Nat. Chem. Biol.* **2006**, *2*, 375–380.
- (22) Kim, H. N.; Lee, M. H.; Kim, H. J.; Kim, J. S.; Yoon, J. *Chem. Soc. Rev.* **2008**, *37*, 1465–1472.
- (23) Cho, D.-G.; Sessler, J. L. *Chem. Soc. Rev.* **2009**, *38*, 1647–1662.
- (24) Jun, M. E.; Roy, B.; Ahn, K. H. *Chem. Commun.* **2011**, *47*, 7583–7601.
- (25) Du, J.; Hu, M.; Fan, J.; Peng, X. *Chem. Soc. Rev.* **2012**, *41*, 4511–4535.
- (26) Ahn, H.-Y.; Fairfull-Smith, K. E.; Morrow, B. J.; Lussini, V.; Kim, B.; Bondar, M. V.; Bottle, S. E.; Belfield, K. D. *J. Am. Chem. Soc.* **2012**, *134*, 4721–4730.
- (27) Ambrose, W. P.; Goodwin, P. M.; Jett, J. H. *Chem. Rev.* **1999**, *99*, 2929–2956.
- (28) Johnson, K. S.; Needoba, J. A.; Riser, S. C. *Chem. Rev.* **2007**, *107*, 623–640.
- (29) Merbach, A.; Helm, L.; Tóth, É. *The Chemistry of Contrast Agents in Medical Magnetic Resonance Imaging*; 2nd ed.; Chichester, UK: Wiley: Chichester, UK, 2013.
- (30) Caravan, P.; Ellison, J. J.; McMurry, T. J.; Lauffer, R. B. *Chem. Rev.* **1999**, *99*, 2293–2352.
- (31) Lanza, G. M.; Winter, P. M.; Neubauer, A. M.; Caruthers, S. D.; Hockett, F. D.; Wickline, S. A. *Curr. Top. Dev. Biol.* **2005**, *70*, 57–76.

- (32) Reineri, F.; Viale, A.; Giovenzana, G.; Santelia, D.; Dastrù, W.; Gobetto, R.; Aime, S. *J. Am. Chem. Soc.* **2008**, *130*, 15047–15053.
- (33) Aime, S.; Caravan, P. *J. Magn. Reson. Imaging* **2009**, *30*, 1259–1267.
- (34) Que, E. L.; Chang, C. J. *Chem. Soc. Rev.* **2010**, *39*, 51–60.
- (35) Major, J. L.; Meade, T. J. *Acc. Chem. Res.* **2009**, *42*, 893–903.
- (36) De León-Rodríguez, L. M.; Lubag, A. J. M.; Malloy, C. R.; Martinez, G. V.; Gillies, R. J.; Sherry, A. D. *Acc. Chem. Res.* **2009**, *42*, 948–957.
- (37) Terreno, E.; Castelli, D. D.; Viale, A.; Aime, S. *Chem. Rev.* **2010**, *110*, 3019–3042.
- (38) Do, Q. N.; Ratnakar, J. S.; Kovacs, Z.; Sherry, A. D. *ChemMedChem* **2014**, *9*, 1116–1129.
- (39) Tsitovich, P. B.; Burns, P. J.; McKay, A. M.; Morrow, J. R. *J. Inorg. Biochem.* **2014**, *133*, 143–154.
- (40) Aime, S.; Botta, M.; Gianolio, E.; Terreno, E. *Angew. Chem. Int. Ed.* **2000**, *39*, 747–750.
- (41) Loving, G. S.; Mukherjee, S.; Caravan, P. *J. Am. Chem. Soc.* **2013**, *135*, 4620–4623.
- (42) Chen, J. W.; Pham, W.; Weissleder, R.; Bogdanov, A. *Magn. Reson. Med.* **2004**, *52*, 1021–1028.
- (43) Yu, M.; Beyers, R. J.; Gorden, J. D.; Cross, J. N.; Goldsmith, C. R. *Inorg. Chem.* **2012**, *51*, 9153–9155.
- (44) Jain, K. K. *Textbook of Hyperbaric Medicine*; 5th ed.; Hogrefe, 2009.
- (45) Harris, A. L. *Nat. Rev. Cancer.* **2002**, *2*, 38–47.
- (46) Krohn, K. A.; Link, J. M.; Mason, R. P. *J. Nucl. Med.* **2008**, *49*, 129S–148S.
- (47) Sur, S. K.; Bryant, R. G. *J. Phys. Chem.* **1995**, *99*, 7172–7179.
- (48) Szejtli, J. *Cyclodextrin Technology*; Springer, 1988.

- (49) Yushmanov, V. E.; Tominaga, T. T.; Borissevitch, I. E.; Imasato, H.; Tabak, M. *Magn. Reson. Imaging* **1996**, *14*, 255–261.
- (50) Kim, W. D.; Kiefer, G. E.; Maton, F.; McMillan, K.; Muller, R. N.; Sherry, A. D. *Inorg. Chem.* **1995**, *34*, 2233–2243.
- (51) Silvio Aime; Luisella Calabi; Camilla Cavallotti; Eliana Gianolio; Giovanni B Giovenzana; Pietro Losi; Alessandro Maiocchi; Giovanni Palmisano, A.; Sisti, M. *Inorg. Chem.* **2004**, *43*, 7588–7590.
- (52) Hajela, S.; Botta, M.; Giraud, S.; Xu, J. *J. Am. Chem. Soc.* **2000**, *122*, 11228–11229.
- (53) Urbanczyk-Pearson, L. M.; Femia, F. J.; Smith, J.; Parigi, G.; Duimstra, J. A.; Eckermann, A. L.; Luchinat, C.; Meade, T. J. *Inorg. Chem.* **2008**, *47*, 56–68.
- (54) Chang, C. A.; Francesconi, L. C.; Malley, M. F.; Kumar, K.; Gougoutas, J. Z.; Tweedle, M. F.; Lee, D. W.; Wilson, L. J. *Inorg. Chem.* **1993**, *32*, 3501–3508.
- (55) Duimstra, J. A.; Femia, F. J.; Meade, T. J. *J. Am. Chem. Soc.* **2005**, *127*, 12847–12855.
- (56) Tu, C.; Nagao, R.; Louie, A. Y. *Angew. Chem. Int. Ed.* **2009**, *48*, 6547–6551.
- (57) Kimura, K.; Yamashita, T.; Yokoyama, M. *J. Chem. Soc., Perkin Trans. 2* **1992**, 613–619.
- (58) Tu, C.; Osborne, E. A.; Louie, A. Y. *Tetrahedron* **2009**, *65*, 1241–1246.
- (59) Iwaki, S.; Hanaoka, K.; Piao, W.; Komatsu, T.; Ueno, T.; Terai, T.; Nagano, T. *Bioorg. Med. Chem. Lett.* **2012**, *22*, 2798–2802.
- (60) Kizaka-Kondoh, S.; Konse-Nagasawa, H. *Cancer Science* **2009**, *100*, 1366–1373.
- (61) Liu, Y.; Xu, Y.; Qian, X.; Liu, J.; Shen, L.; Li, J.; Zhang, Y. *Bioorg. Med. Chem.* **2006**, *14*, 2935–2941.

- (62) Nakata, E.; Yukimachi, Y.; Kariyazono, H.; Im, S.; Abe, C.; Uto, Y.; Maezawa, H.; Hashimoto, T.; Okamoto, Y.; Hori, H. *Bioorg. Med. Chem.* **2009**, *17*, 6952–6958.
- (63) Yu, M.; Ambrose, S. L.; Whaley, Z. L.; Fan, S.; Gorden, J. D.; Beyers, R. J.; Schwartz, D. D.; Goldsmith, C. R. *J. Am. Chem. Soc.* **2014**, *136*, 12836–12839.
- (64) Iranzo, O. *Bioorg. Chem.* **2011**, *39*, 73–87.
- (65) Carrera, C.; Digilio, G.; Baroni, S.; Burgio, D.; Consol, S.; Fedeli, F.; Longo, D.; Mortillaro, A.; Aime, S. *Dalton Trans.* **2007**, 4980–4987.
- (66) Carlsson, J.; Drevin, H.; Axen, R. *Biochem. J.* **1978**, *173*, 723–737.
- (67) Terreno, E.; Botta, M.; Boniforte, P.; Bracco, C.; Milone, L.; Mondino, B.; Uggeri, F.; Aime, S. *Chem. Eur. J.* **2005**, *11*, 5531–5537.
- (68) Aime, S.; Gianolio, E.; Terreno, E.; Giovenzana, G. B.; Pagliarin, R.; Sisti, M.; Palmisano, G.; Botta, M.; Lowe, M. P.; Parker, D. *J. Biol. Inorg. Chem.* **2000**, *5*, 488–497.
- (69) Terreno, E.; Botta, M.; Fedeli, F.; Mondino, B.; Milone, L.; Aime, S. *Inorg. Chem.* **2003**, *42*, 4891–4897.
- (70) Viger, M. L.; Sankaranarayanan, J.; de Gracia Lux, C.; Chan, M.; Almutairi, A. *J. Am. Chem. Soc.* **2013**, *135*, 7847–7850.
- (71) Gracia Lux, C.; Joshi-Barr, S.; Nguyen, T.; Mahmoud, E.; Schopf, E.; Fomina, N.; Almutairi, A. *J. Am. Chem. Soc.* **2012**, *134*, 15758–15764.
- (72) Aime, S.; Fasano, M.; Terreno, E. *Chem. Soc. Rev.* **1998**, *27*, 19–29.
- (73) Peters, J. A.; Huskens, J.; Raber, D. J. *Prog. Nucl. Magn. Reson. Spectrosc.* **1996**, *28*, 283–350.

- (74) Jagadish, B.; Guntle, G. P.; Zhao, D.; Gokhale, V.; Ozumerzifon, T. J.; Ahad, A. M.; Mash, E. A.; Raghunand, N. *J. Med. Chem.* **2012**, *55*, 10378–10386.
- (75) Martinelli, J.; Fekete, M.; Tei, L.; Botta, M. *Chem. Commun.* **2011**, *47*, 3144.
- (76) Aime, S.; Botta, M.; Panero, M.; Grandi, M.; Uggeri, F. *Magn. Reson. Chem.* **1991**, *29*, 923–927.
- (77) Aime, S.; Botta, M.; Frullano, L.; Crich, S. G.; Giovenzana, G. B.; Pagliarin, R.; Palmisano, G.; Sisti, M. *Chem. Eur. J.* **1999**, *5*, 1253–1260.
- (78) Aime, S.; Botta, M.; Fedeli, F.; Gianolio, E.; Terreno, E.; Anelli, P. *Chem. Eur. J.* **2001**, *7*, 5261–5269.
- (79) Burns, J. A.; Butler, J. C.; Moran, J.; Whitesides, G. M. *J. Org. Chem.* **1991**, *56*, 2648–2650.
- (80) Zhang, S.; Merritt, M.; Woessner, D. E.; Lenkinski, R. E.; Sherry, A. D. *Acc. Chem. Res.* **2003**, *36*, 783–790.
- (81) Ward, K. M.; Aletras, A. H.; Balaban, R. S. *J. Magn. Reson.* **2000**, *143*, 79–87.
- (82) Woessner, D. E.; Zhang, S.; Merritt, M. E.; Sherry, A. D. *Magn. Reson. Med.* **2005**, *53*, 790–799.
- (83) Viswanathan, S.; Kovacs, Z.; Green, K. N.; Ratnakar, S. J.; Sherry, A. D. *Chem. Rev.* **2010**, *110*, 2960–3018.
- (84) Li, A. X.; Suchy, M.; Li, C.; Gati, J. S.; Meakin, S.; Hudson, R. H. E.; Menon, R. S.; Bartha, R. *Magn. Reson. Med.* **2011**, *66*, 67–72.
- (85) Ratnakar, S. J.; Woods, M.; Lubag, A. J. M.; Kovacs, Z.; Sherry, A. D. *J. Am. Chem. Soc.* **2008**, *130*, 6–7.

- (86) Mani, T.; Tircsó, G.; Togao, O.; Zhao, P.; Soesbe, T. C.; Takahashi, M.; Sherry, A. D. *Contrast Media Mol. Imaging* **2009**, *4*, 183–191.
- (87) Viswanathan, S.; Ratnakar, S. Â. J.; Green, K. N.; Kovacs, Z.; Deâ LeÃ n-RodrÃ guez, L. M.; Sherry, A. Â. D. *Angew. Chem.* **2009**, *121*, 9494–9497.
- (88) Ratnakar, S. J.; Viswanathan, S.; Kovacs, Z.; Jindal, A. K.; Green, K. N.; Sherry, A. D. *J. Am. Chem. Soc.* **2012**, *134*, 5798–5800.
- (89) Terreno, E.; Boffa, C.; Menchise, V.; Fedeli, F.; Carrera, C.; Castelli, D. D.; Digilio, G.; Aime, S. *Chem. Commun.* **2011**, *47*, 4667.
- (90) Ratnakar, S. J.; Soesbe, T. C.; Lumata, L. L.; Do, Q. N.; Viswanathan, S.; Lin, C.-Y.; Sherry, A. D.; Kovacs, Z. *J. Am. Chem. Soc.* **2013**, *135*, 14904–14907.
- (91) Hyodo, F.; Matsumoto, K. I.; Matsumoto, A.; Mitchell, J. B.; Krishna, M. C. *Cancer Research* **2006**, *66*, 9921–9928.
- (92) Castelli, D. D.; Gianolio, E.; Crich, S. G.; Terreno, E. *Coord. Chem. Rev.* **2008**, *252*, 2424–2443.
- (93) Dorazio, S. J.; Tsitovich, P. B.; Sifers, K. E.; Sperryak, J. A.; Morrow, J. R. *J. Am. Chem. Soc.* **2011**, *133*, 14154–14156.
- (94) Olatunde, A. O.; Dorazio, S. J.; Sperryak, J. A.; Morrow, J. R. *J. Am. Chem. Soc.* **2012**, *134*, 18503–18505.
- (95) Tsitovich, P. B.; Sperryak, J. A.; Morrow, J. R. *Angew. Chem. Int. Ed.* **2013**, *52*, 13997–14000.
- (96) Comba, P.; Sickmüller, A. F. *Inorg. Chem.* **1997**, *36*, 4500–4507.

Chapter 2

**A Magnetic Resonance Imaging Contrast Agent Capable of
Detecting Hydrogen Peroxide***

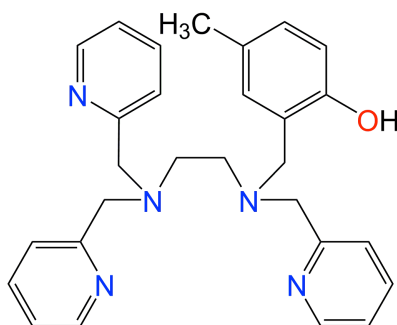
* This Chapter is a revision of a published paper: Meng Yu, Ronald J. Beyers, John D. Gorden, Justin N. Cross, Christian R. Goldsmith, *Inorganic Chemistry*, **2012**, *51*, 9153-9155. Reprint with permission. Copyright © 2012 by the American Chemical Society.

2.1 Introduction

Reactive oxygen species (ROSs) have been implicated in a seemingly myriad array of health disorders, including several major cardiovascular and neurological diseases.¹⁻⁶ Probing the role of ROSs in these conditions currently depends heavily on indirect methods, such as post-mortem analysis of protein oxidation. Most probes capable of directly detecting ROSs rely on changes in fluorescence or luminescence to signal the analyte.⁷⁻¹⁴ Although these probes offer high spatial resolution, the short wavelengths of excitation associated with most fluorophores render them unsuitable for imaging within intact organs or whole bodies. Magnetic resonance imaging (MRI), conversely, uses much longer wavelengths and is commonly used to visualize softer tissues within patients. In practice, a paramagnetic contrast agent is often administered to shorten the T_1 relaxation time of the excited protons and thereby improve the signal quality. Many recently reported contrast agents have been designed to convert into a species with a different relaxivity upon reaction with a target analyte, such as an enzyme or a metabolite.¹⁵⁻²² One previously reported target for these sensors is myeloperoxidase (MPO), which is involved in ROS metabolism.²⁰⁻²² Another recently developed MRI contrast agent responds to the reductant β -NADH.²³

In our efforts to develop a MRI contrast agent capable of more directly detecting the oxidative stress associated with ROSs, we prepared the redox-active ligand N-(2-hydroxy-5-methylbenzyl)-*N,N,N'*-tris(2-pyridinylmethyl)-1,2-ethanediamine (Htp1, Scheme 2.1) and its Mn(II) complex. The ligand is prepared in one step from the reaction between 2-hydroxy-5-methylbenzaldehyde and the previously reported *N,N,N'*-tris(2-pyridinylmethyl)-1,2-ethanediamine.²⁴ The yield of the Htp1 ligand is 60% after purification by column

chromatography. The subsequent complexation reaction between Htp1 and $\text{Mn}(\text{ClO}_4)_2$ in anaerobic acetonitrile (MeCN) provides $[\text{Mn}(\text{Htp1})(\text{MeCN})](\text{ClO}_4)_2$ in 90% yield.



Scheme 2.1 Structure of Htp1 ligand.

2.2 Experimental Section

Materials

All chemicals were acquired from Sigma-Aldrich and used as received except where noted otherwise. Deuterated dimethylsulfoxide ($\text{DMSO-}d_6$) was bought from Cambridge Isotopes. Diethyl ether (ether) and methanol (MeOH) were purchased from Fisher. Methylene chloride (CH_2Cl_2) was bought from Mallinckrodt Baker. The ligand precursor *N,N,N'*-tris(2-pyridinylmethyl)-1,2-ethanediamine was prepared through a previously described procedure.²⁴

Caution: Although no problems were encountered with the described research, perchlorate salts of metal complexes are potentially explosive. The dangers can be minimized by working with small quantities of these reagents, working in aqueous solutions, and using appropriate safety measures, such as protective shields, for the preparation and handling of these materials.

Instrumentation

^1H and ^{13}C NMR spectra were recorded on a 250 MHz or 400 MHz AV Bruker NMR spectrometer at 293 K. All reported resonances were referenced to internal standards. Electron paramagnetic resonance (EPR) spectra were collected on a Bruker EMX-6/1 X-band EPR spectrometer operated in the perpendicular mode and analyzed with the program EasySpin. Each

sample was run as a frozen solution in a quartz tube. A Johnson Matthey magnetic susceptibility balance (model MK I#7967) was used to measure the magnetic moments of solid samples. High resolution mass spectrometry (HR-MS) data were acquired at the Mass Spectrometer Center at Auburn University on a Bruker microflex LT MALDI-TOF mass spectrometer via direct probe analysis operated in the positive ion mode. Samples that were to be submitted for elemental analysis were crystallized and subsequently dried under vacuum before shipment to Atlantic Microlabs (Norcross, GA). This treatment appears to have removed the MeCN molecules observed in the crystals of $[\text{Mn}(\text{Hptp1})(\text{MeCN})](\text{ClO}_4)_2$.

X-Ray Crystallography

A crystal of $[\text{Mn}(\text{Hptp1})(\text{MeCN})](\text{ClO}_4)_2$ was mounted in paratone oil on a glass fiber and aligned on a Bruker SMART APEX CCD X-ray diffractometer. Intensity measurements were performed using graphite monochromated Mo $K\alpha$ radiation ($\lambda = 0.71073 \text{ \AA}$) from a sealed tube and monocapillary collimator. SMART (v 5.624) was used to determine the preliminary cell constants and regulate the data acquisition. The intensities of reflections of a sphere were collected through the compilation of three sets of exposures (frames). Each set had a different ϕ angle for the crystal, with each exposure spanning a range of 0.3° in ω . A total of 1800 frames were collected with exposure times of 40 s per frame. The data were corrected for Lorentz and polarization effects. Structures were solved using direct methods and expanded using Fourier techniques. All non-hydrogen atoms were refined anisotropically. Hydrogen atoms were included at idealized positions 0.95 \AA from their parent atoms prior to the final refinement. Further details regarding the data acquisition and analysis are included in Tables 2A.1-4.

A single crystal of $[\text{Mn}_2(\text{Hptp1}_2)(\text{MeCN})_2](\text{ClO}_4)_3$ was mounted on a cryoloop with viscous Krytox and optically aligned on a Bruker APEXII Quazar X-ray diffractometer using a

digital camera. Initial intensity measurements were performed using an I μ S X-ray source and a 30 W microfocused sealed tube (MoK α , $\lambda = 0.71073$ Å) with high-brilliance and high-performance focusing Quazar multilayer optics. Standard APEXII software was used for the determination of the unit cells and data collection control. The intensities of reflections of a sphere were collected by a combination of five sets of exposures (frames). Each set had a different ϕ angle for the crystal, and each exposure covered a range of 0.5° in ω . 1742 frames were collected with an exposure time of 40 s per frame. The SAINT software was used for data integration, including Lorentz and polarization corrections. Semi-empirical absorption corrections were applied using the program SADABS.

Measurement of Binding Affinity of Htp1 for Mn(II)

The $\log(K)$ was measured via a competitive binding assay between *N,N,N',N'*-tetrakis(2-pyridylmethyl)ethylenediamine (TPEN) and Htp1. Various amounts of TPEN were added to a solution of [Mn(Htp1)(MeCN)](ClO₄)₂ in MeCN-*d*₃. The resultant mixtures were analyzed by ¹H NMR. The ratio of uncoordinated TPEN to uncoordinated Htp1 was used to measure an equilibrium constant of 0.45 for the reaction:



This equilibrium constant was then combined with the known $\log(K)$ of 10.3 for TPEN²⁵ to obtain a $\log(K)$ of 10.6 for Htp1.

Magnetic Resonance Imaging (MRI)

All MRI data were collected at the Auburn University MRI Research Center (Auburn, AL) on a Siemens Verio open-bore 3-T MRI clinical scanner. A 15-channel knee coil was used

to simultaneously image 12-26 samples. An inversion recovery (IR) sequence was used that featured a non-selective adiabatic inversion pulse followed by a slice-selective gradient recalled echo (GRE) readout after a delay period corresponding to the inversion time (TI). The GRE was a saturation readout, such that only one line of k-space was acquired per repetition time (TR). This method was selected to maximize both the signal strength and the accuracy of the T_1 estimates. Specific imaging parameters were as follows: TR was set to 4 s, TI was varied from 4.8 to 2500 ms over 37 steps, the echo time (TE) was set to 3.6 ms, the flip angle equaled 90° , averages = 1, slice thickness = 5 mm, field of view = 140×140 mm, matrix = 128×128 , resulting in a pixel size of $1.1 \times 1.1 \times 5.0$ mm. All samples were run in 50 mM solutions of HEPES in water, buffered to pH 7.0 and kept at 22 °C. The manganese content was systematically varied from 0.10 to 1.00 mM. The inverses of the T_1 values were plotted versus the concentration of Mn(II) to obtain r_1 values. All reported r_1 values are derived from the results of two separate series of experiments. Each series of experiments used a different batch of $[\text{Mn}(\text{ptp}1)(\text{MeCN})](\text{ClO}_4)_2$.

MRI Data Analysis

Image analysis was performed using custom Matlab programs (Mathworks, Natick, MA). The initial TI = 4.8 ms image served as a baseline to determine the circular region of interest (ROI) boundaries for each sample; from these, the mean pixel magnitudes for each ROI were calculated. For each of the 36 subsequent TI images, the same ROI boundaries were applied and the mean pixel magnitude calculations were repeated. This gave consistent ROI spatial definitions and a corresponding time course of magnitudes for each of the samples over all the TI time points. Each sample's complex phase was used to correct the magnitude polarity to produce

a complete exponential T_1 inversion recovery curve. The Nelder-Mead simplex algorithm was applied to each sample's exponential curve to estimate its corresponding T_1 value.

Syntheses

***N*-(2-Hydroxy-5-methyl-benzyl)-*N,N',N'*-tris(2-pyridinylmethyl)-1,2-ethanediamine (Hptp1).**

N,N,N'-Tris(2-pyridinylmethyl)-1,2-ethanediamine (3.10 g, 9.3 mmol) was dissolved in 50 mL of 1,2-dichloroethane. 2-Hydroxy-5-methylbenzaldehyde (1.39 g, 10.2 mmol) was added to the resultant solution, followed by $\text{NaBH}(\text{OAc})_3$ (5.94 g, 27.9 mmol), which was introduced gradually over the course of 1 h. After the resultant mixture stirred for 24 h, 100 mL of saturated $\text{NaH}(\text{CO}_3)$ was added to quench the reaction. The reaction mixture stirred for 1 h, at which point the product was extracted with three 40 mL portions of CH_2Cl_2 . The combined organic layers were washed with three 20 mL aliquots of H_2O and dried over anhydrous Na_2SO_4 . The solvent was evaporated to yield the crude product. The crude was subsequently purified by chromatography (silica, 15:1 $\text{CH}_2\text{Cl}_2/\text{MeOH}$ elutant, product $R_f = 0.45$) to yield the product as a yellow oil (2.5 g, 60% yield). ^1H NMR (400 MHz, CDCl_3 , 293 K): δ 8.51 (d, $J = 4.9$ Hz, 1H), 8.47 (d, $J = 4.9$ Hz, 2H), 7.56 (m, 3 H), 7.48 (d, $J = 8.0$ Hz, 2H), 7.21 (d, $J = 8.0$ Hz, 1H), 7.12 (m, 3H), 6.94 (d, $J = 8.0$ Hz, 1H), 6.73 (m, 2H), 3.72 (s, 2H), 3.70 (s, 4H), 3.64 (s, 2H), 2.74 (s, 4H), 2.22 (s, 3H). ^{13}C NMR (400 MHz, CDCl_3 , 293 K): δ 159.17, 157.75, 155.13, 149.04, 148.86, 136.61, 136.45, 129.82, 129.23, 127.99, 123.49, 123.21, 122.31, 122.00, 121.97, 116.02, 60.35, 59.65, 57.45, 50.98, 50.81, 20.46. MS (ESI): Calcd for MH^+ , 454.2607; Found, 454.2530.

Acetonitrilo(*N*-(2-hydroxy-5-methyl-benzyl)-*N,N',N'*-tris(2-pyridinylmethyl)-1,2-ethanediamine)manganese(II) perchlorate ([Mn(Hptp1)(MeCN)](ClO_4) $_2$).

The ptp1 ligand (484 mg, 1.07 mmol) and $\text{Mn}(\text{ClO}_4)_2 \cdot \text{XH}_2\text{O}$ (400 mg, 1.10 mmol) were dissolved in 5 mL of MeCN under N_2 . The solution was allowed to stir at room temperature for 16 h, at which point the organic solvent was removed. The oily residue was dissolved in 1 mL of fresh MeCN. Ether (3 mL) was added to the solution, precipitating the product as a white powder upon cooling (724 mg, 90% yield). Crystals suitable for single crystal X-ray diffraction were grown from the slow diffusion of ether into a saturated MeCN solution of the Mn(II) complex. Solid-state magnetic susceptibility (295 K): $\mu_{\text{eff}} = 5.8 \mu_{\text{B}}$. EPR (77 K, 50 mM HEPES buffered to pH 7.0): $g_{\text{eff}} = 2.41$, $A = 49$. IR (KBr, cm^{-1}): 3373 (m), 3171 (m), 2951 (w), 2923 (w), 2860 (w), 2404 (w), 2303 (w), 2272 (w), 2255 (w), 2015 (w), 1985 (w), 1904 (w), 1869 (w), 1606 (s), 1572 (w), 1511 (w), 1482 (m), 1442 (m), 1400 (m), 1387 (w), 1370 (w), 1347 (w), 1313 (w), 1259 (m), 1211 (w), 1117 (s), 1094 (s), 1056 (s), 1013 (s), 977 (m), 949 (m), 931 (w), 917 (m), 898 (w), 849 (w), 823 (m), 768 (s), 730 (w), 624 (s), 560 (w), 541 (w), 526 (w). MS (ESI): Calcd for $[\text{Mn}(\text{ptp1})]^+$, 507.1830 and for $[\text{Mn}(\text{Hptp1})(\text{ClO}_4)]^+$, 607.1395; Found, 507.1410 and 607.1605. Elemental Analysis: Calcd for $\text{C}_{28}\text{H}_{31}\text{N}_5\text{MnCl}_2\text{O}_9 \cdot 2\text{H}_2\text{O}$: C, 45.23%; H, 4.75%; N, 9.42%; Found: C, 45.12%; H, 4.66%; N, 9.56%.

$[\text{Mn}_2(\text{Hptp1}_2)(\text{MeCN})_2](\text{ClO}_4)_3$.

$[\text{Mn}(\text{Hptp1})(\text{MeCN})](\text{ClO}_4)_2$ (200 mg, 0.268 mmol) was dissolved in 1.5 mL of MeCN. 36 mg (1.06 mmol) of H_2O_2 was added as a solution of 30% H_2O_2 in water. The mixture was stirred for 3 h, during which time a white solid precipitated. The precipitate was isolated through filtration and washed with cold MeCN to yield 74 mg of the product as a white powder (40% yield). Crystals suitable for X-ray diffraction were grown by slow evaporation of a concentrated solution of complex in a mixture of MeOH and MeCN. Solid-state magnetic susceptibility (295 K): $\mu_{\text{eff}} = 7.7 \mu_{\text{B}}$. EPR (77 K, 50 mM HEPES buffered to pH 7.0): $g_{\text{eff}} = 2.04$, $A = 44$. IR (KBr,

cm⁻¹): 3420 (s), 3183 (m), 2920 (w), 2857 (w), 2498 (w), 2362 (w), 2335 (w), 2273 (w), 2249 (w), 2207 (w), 2016 (w), 1869 (w), 1604 (m), 1572 (w), 1540 (w), 1480 (w), 1441 (m), 1401 (m), 1344 (w), 1307 (w), 1279 (w), 1262 (w), 1248 (w), 1144 (s), 1117 (s), 1111 (s), 1085 (s), 1011 (m), 982 (w), 938 (w), 900 (w), 865 (w), 847 (w), 767 (m), 729 (w), 690 (w), 669 (w), 652 (w), 626 (m), 593 (w), 579 (w), 565 (w), 549 (w), 539 (w). MS (ESI): Calcd for [Mn₂(ptp1₂)]⁺, 506.1741; Found, 506.1702. Elemental Analysis: Calcd for C₆₀H₆₅N₁₂Mn₂Cl₃O₁₄: C, 51.68%; H, 4.70%; N, 12.05%; Found: C, 51.52%; H, 5.00%; N, 12.44%.

2.3 Results and Discussion

Crystal Structure

Crystalline [Mn(Htp1)(MeCN)](ClO₄)₂ can be obtained from the slow diffusion of ethyl ether into a MeCN solution of the Mn(II) complex (Figure 2.1). The crystal structure reveals that the manganese is heptacoordinate, with six donor atoms originating from the Htp1 ligand. The overall geometry may be best described as a distorted pentagonal bipyramid, with the phenol and one of the pyridine rings in the axial positions. The heptacoordination and the metal-ligand bond distances are consistent with a +2 oxidation state for the manganese. This assignment is corroborated by the light color of the crystals and the 5.8 μ_B magnetic moment measured for the solid.

Unexpectedly, the phenol appears to retain its proton upon coordination, as assessed by the Mn-O and C-O bond lengths and the anion count. The 1.39 Å C-O bond length closely matches the 1.38 Å value for phenol.²⁶ The phenol oxygen is 2.60 Å away from the oxygen atom of an outer-sphere water molecule, suggesting a hydrogen bond interaction between the two. This hydrogen bond may stabilize the proton's continued presence on the phenol. Two hydrogen

atoms were located on the water, precluding the alternative assignment of an outer-sphere hydroxide anion and a deprotonated ligand (ptp1⁻).

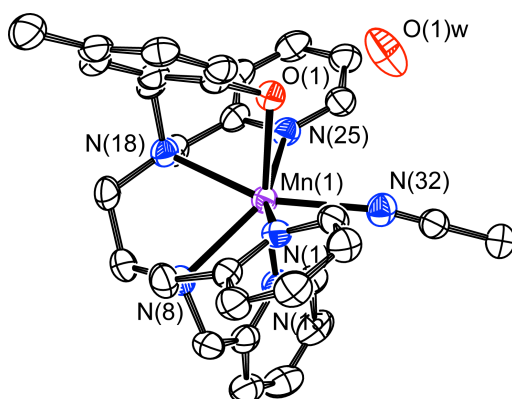


Figure 2.1. ORTEP representation of $[\text{Mn}(\text{Hptp1})(\text{MeCN})]^{2+}$. All hydrogen atoms, both ClO_4^- counteranions, and two solvated MeCN molecules have been omitted for clarity. All thermal ellipsoids are drawn at 50% probability. Further details about the structure are reported in the Appendix. (All the CIFs are available on the website of ACS publications free of charge)

Stability

Solutions of the Mn(II) complex are stable when exposed to air at 25 °C in both MeCN and H₂O. Under these conditions, no discoloration of the samples is observed over 24 h. The aqueous stability of the Hptp1-Mn(II) bonds is confirmed by ¹H NMR and EPR. No ligand resonances are observed in the spectrum of the Mn(II) compound in D₂O, and the EPR spectrum of the Mn(II) Hptp1 complex in water is distinct from that of $[\text{Mn}(\text{H}_2\text{O})_6]^{2+}$. The Hptp1 ligand can be displaced by a more strongly binding ligand; the addition of 1 equiv of EDTA removes the Mn(II) from the complex instantaneously. The log *K* for the binding of Hptp1 to Mn(II) is estimated to be 10.6, based on a competitive binding assay with *N,N,N',N'*-tetrakis(2-pyridinylmethyl)ethylenediamine (log *K* = 10.3).²⁵ Our preliminary results suggest that other metal ions do not rapidly substitute for the Mn(II) in the Hptp1 complex. In MeCN, 1 equiv of Fe(II) does not displace a noticeable amount of Mn(II) from the complex over the course of 1 h.

At 18 h, only 17% of the Mn(II) has been displaced, as assessed by UV/vis spectroscopy. It should be noted that the 0.10 mM concentration of free iron added at the beginning of this experiment is much higher than biologically relevant levels.

MRI Measurement

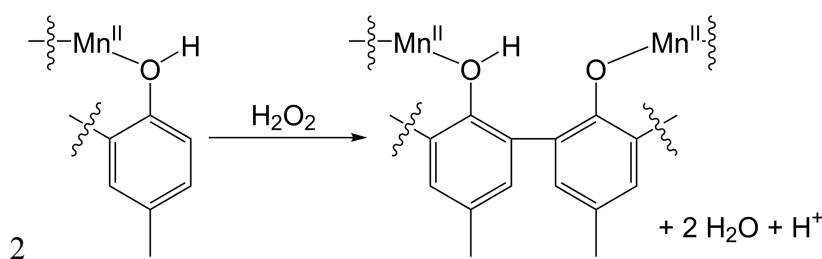
The $[\text{Mn}(\text{Htp1})(\text{MeCN})]^{2+}$ complex is a capable MRI contrast agent, with a measured relaxivity of $4.39 \text{ mM}^{-1} \text{ s}^{-1}$ in buffered aqueous solutions (3 T, 50 mM HEPES, pH 7.00, 25 °C). This r_1 value is relatively high for a mononuclear Mn(II) complex,²⁷⁻²⁹ but is lower than that measured for $[\text{Mn}(\text{H}_2\text{O})_6]^{2+}$ under identical conditions.²⁹ Upon dissolution in water, a molecule of H_2O likely displaces the MeCN, resulting in an aquation number $q = 1$. We speculate that the observed ability of the coordinated phenol to exchange protons with and hydrogen bond to outer-sphere water molecules may further increase the r_1 value of the Mn(II) Htp1 complex relative to those of other mononuclear Mn(II) complexes.

Reactivity with H_2O_2

Upon adding H_2O_2 to solutions of $[\text{Mn}(\text{Htp1})(\text{MeCN})]^{2+}$ in either MeCN or H_2O , their color changes to brown briefly before reverting back to pale yellow. These changes, which finish within seconds, are consistent with the temporary oxidation of the manganese. Mass spectrometric analysis of the solutions reveals m/z peaks consistent with a binuclear manganese complex. This species was subsequently crystallized from the slow evaporation of a MeCN/MeOH mixture (Figure 2.2) and identified as $[\text{Mn}_2(\text{Htp1}_2)(\text{MeCN})_2](\text{ClO}_4)_3$. The crystal structure reveals that the binuclear product results from the formation of a novel covalent bond between the 2-position carbons of the phenol groups from two $[\text{Mn}(\text{Htp1})(\text{MeCN})]^{2+}$ ions (Scheme 2.2). Such oxidative coupling of phenols has been observed in several transition metal systems, including some that contain manganese.^{30, 31} A Gd(III)-containing sensor reported by

Weissleder uses similar phenolic coupling chemistry to detect H_2O_2 .²² Weissleder's probe differs from ours in that it requires MPO to catalyze the coupling. The Mn(II) complex, conversely, does not need this co-analyte.

The coordination around each manganese ion in the oxidized product is similar to that in the mononuclear precursor. Each manganese ion in $[\text{Mn}_2(\text{Htp1}_2)(\text{MeCN})_2]^{3+}$ is heptacoordinate, and the averages of the metal-ligand bond distances for both complexes is 2.35 Å. These structural observations and the pale yellow color of the crystals are consistent with a +2 oxidation state for both metal ions. The bonds between the Mn(II) and the phenol oxygen atoms contract by over 0.2 Å upon oxidation, consistent with the deprotonation of at least one of the phenols. The IR spectrum of the binuclear complex has a feature at 3420 cm^{-1} , suggesting that the diphenol bridge within the coupled ligand retains a proton. The ligand is therefore best assigned as Htp1_2^- . The C-O bonds in $[\text{Mn}_2(\text{Htp1}_2)(\text{MeCN})_2]^{3+}$ are both 1.36 Å, which, although slightly shorter than the 1.39 Å C-O bond in $[\text{Mn}(\text{Htp1})(\text{MeCN})]^{2+}$, are atypical bond lengths for a fully deprotonated phenolate. We therefore believe that the proton in Htp1_2^- spans the two phenolic oxygens.



Scheme 2.2 Oxidative coupling of phenols in the presence of H_2O_2 .

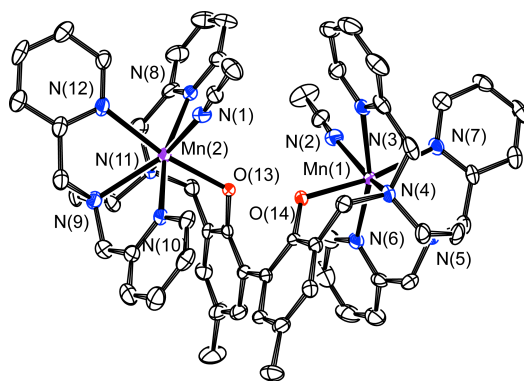


Figure 2.2. ORTEP representation of $[\text{Mn}_2(\text{Hptp1}_2)(\text{MeCN})_2]^{3+}$. All hydrogen atoms, ClO_4^- counteranions, and non-coordinated solvent molecules have been omitted for clarity. All thermal ellipsoids are drawn at 50% probability. Additional information about the structure is reported in the Appendix. (All the CIFs are available on the website of ACS publications free of charge)

MRI response to H_2O_2

When 10 mM of H_2O_2 is added to 0.10-1.00 mM solutions of $[\text{Mn}(\text{Hptp1})(\text{MeCN})]^{2+}$ in buffered aqueous solutions (3 T, 50 mM HEPES, pH 7.00, 25 °C), the r_1 per Mn(II) decreases from $4.39 \text{ mM}^{-1} \text{ s}^{-1}$ to $3.59 \text{ mM}^{-1} \text{ s}^{-1}$. As with the mononuclear precursor, H_2O likely exchanges for both inner-sphere MeCN molecules in the binuclear species. The isolated $[\text{Mn}_2(\text{Hptp1}_2)(\text{MeCN})_2](\text{ClO}_4)_3$ has a magnetic moment of $9.0 \mu_{\text{B}}$, or $4.5 \mu_{\text{B}}$ per Mn(II). The decrease in the overall paramagnetism associated with the formation of a binuclear product is known to reduce the relaxivity of other transition-metal MRI contrast agents.³² The r_1 value remains constant over 15 h, suggesting that no further chemical transformations occur after the initial oxidative coupling.

When H_2O_2 is added to $[\text{Mn}(\text{Hptp1})(\text{MeCN})]^{2+}$ in MeCN containing 2,4-dimethylphenol (DMP), mass spectrometry does not detect any $[\text{Mn}_2(\text{Hptp1}_2)(\text{MeCN})_2]^{3+}$. The DMP serves as a competitive substrate as indicated by the observation of m/z features consistent with the manganese complex's coupling to DMP. Reasoning that the phenolic residues of tyrosines may

also be competent coupling partners, we analyzed the MRI response of the $[\text{Mn}(\text{Htp1})(\text{MeCN})]^{2+}$ complex in buffered solutions containing 0.10 mM bovine serum albumin (BSA) with and without 10 mM of H_2O_2 . If the sensor were to oxidatively tether to BSA, the r_1 value would be anticipated to increase due to the slower rate of tumbling.³³ The addition of BSA increases the r_1 values of the reduced and oxidized forms to $5.20 \text{ mM}^{-1} \text{ s}^{-1}$ and $4.37 \text{ mM}^{-1} \text{ s}^{-1}$; these changes are consistent with non-covalent interactions between the proteins and the Mn(II) complexes.³² The $\sim 0.8 \text{ mM}^{-1} \text{ s}^{-1}$ response of the sensor to H_2O_2 is essentially unchanged in the presence of the protein. For BSA, the number of accessible tyrosine residues is apparently not high enough for the potential tyrosine-sensor reactivity to compete with the bimolecular coupling reaction between $[\text{Mn}(\text{Htp1})(\text{MeCN})]^{2+}$ ions. Other peptides, however, may be viable coupling partners.

2.3 Conclusions

The manganese-containing MRI contrast agent $[\text{Mn}(\text{Htp1})(\text{MeCN})]^{2+}$ exhibits a predictable and measurable response to H_2O_2 . The observed decrease in relaxivity is correlated to the oxidative coupling of the sensors, which results in a stable binuclear species that is less paramagnetic per Mn(II) than its mononuclear precursor. As such, the sensor provides a novel means of detecting oxidative activity under physiologically relevant conditions.

Appendix

as is

Meng_MnTPBEN_011212_2 13 (0.277) Cm (8:24)

1: TOF MS ES+
1.51e4

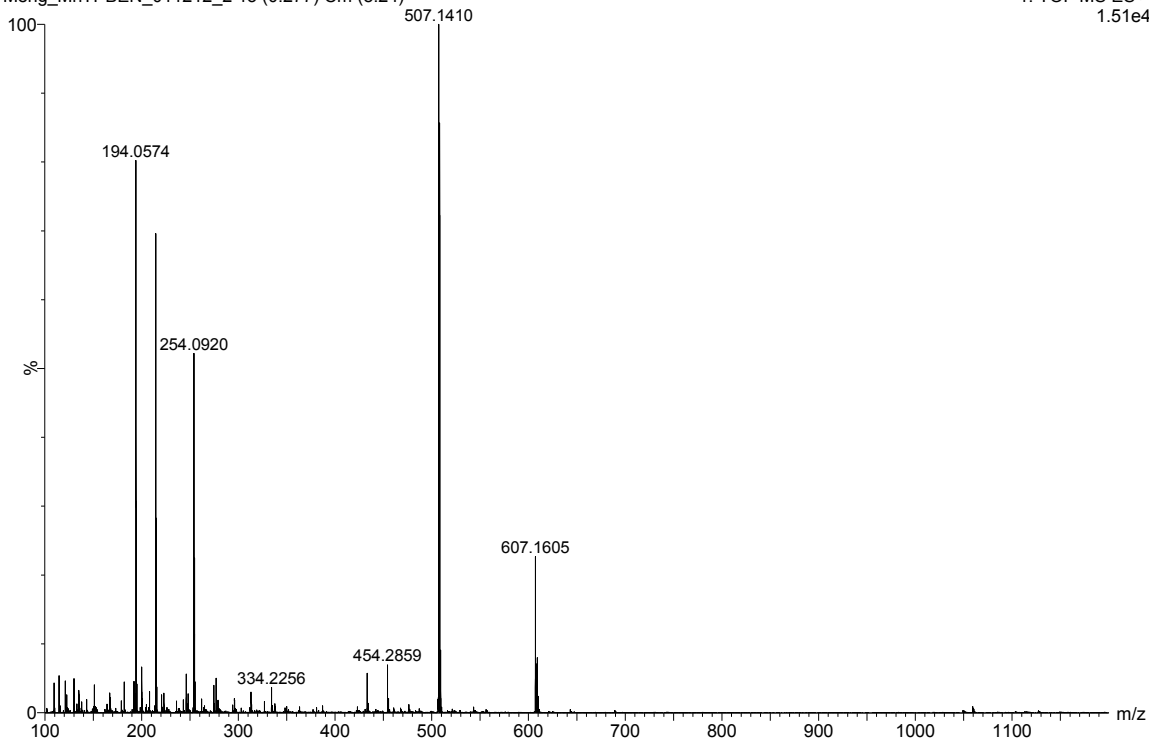


Figure 2A.1. Mass spectrum (ESI) for $[\text{Mn}(\text{Htp1})(\text{MeCN})](\text{ClO}_4)_2$ in MeCN. The 507.1410 m/z feature is assigned to $[\text{Mn}(\text{ptp1})]^+$, which features a deprotonated ptp1 ligand. The 607.1605 m/z feature is assigned to $[\text{Mn}(\text{Htp1})(\text{ClO}_4)]^+$.

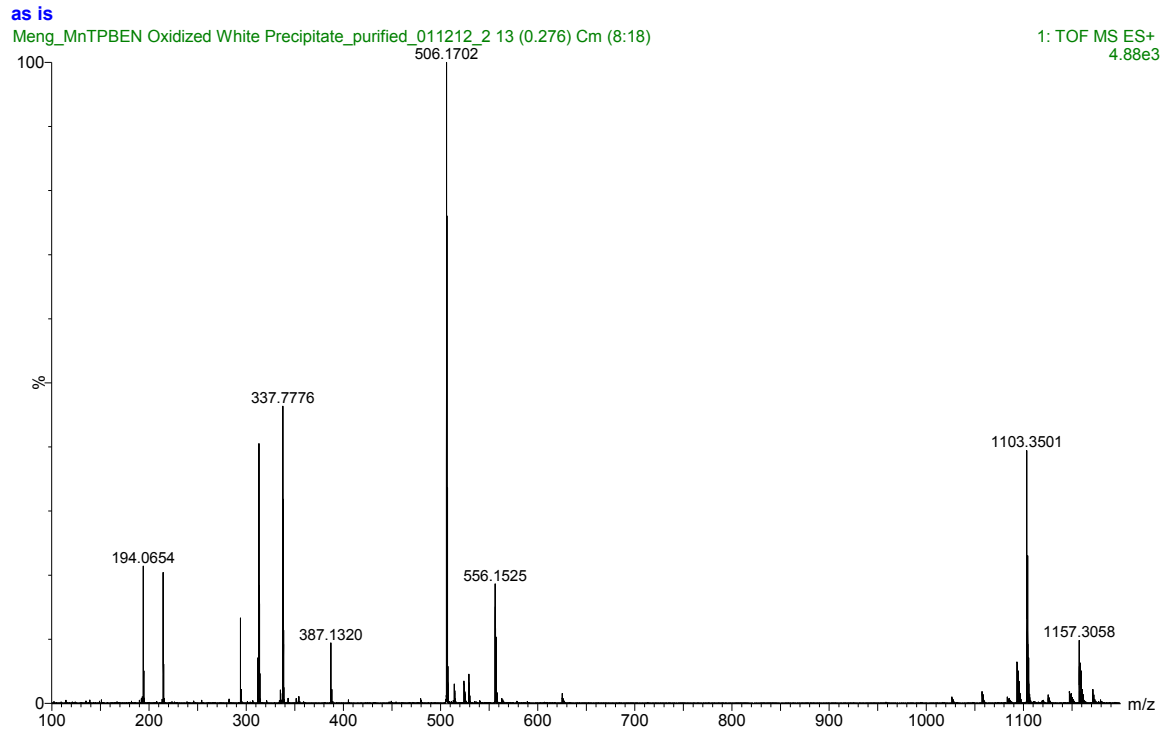


Figure 2A.2. Mass spectrum (ESI) for $[\text{Mn}_2(\text{Hptp}1_2)(\text{MeCN})_2](\text{ClO}_4)_3$ in MeCN. The coupled ligand is singly deprotonated. The 506.1702 m/z feature is assigned to $[\text{Mn}_2(\text{ptp}1_2)]^{2+}$, which features a doubly deprotonated coupled ligand. The 337.7776 m/z feature is assigned to $[\text{Mn}_2(\text{Hptp}1_2)]^{3+}$. The 556.1526 m/z feature is assigned to $[\text{Mn}_2(\text{Hptp}1_2)(\text{ClO}_4)]^{2+}$. The 1103.3501 and 1157.3058 m/z features are assigned to $[\text{Mn}_2(\text{Hptp}1_2)(\text{HCO}_2)_2]^+$ and $[\text{Mn}(\text{Hptp}1_2)(\text{ClO}_4)(\text{HCO}_2)]^+$, respectively; formic acid was present to ionize samples.

mild reaction

Meng_Mnptp1 in water plus H2O2_041312_4 9 (0.369) Cm (6:20)

1: TOF MS ES+
1.39e6

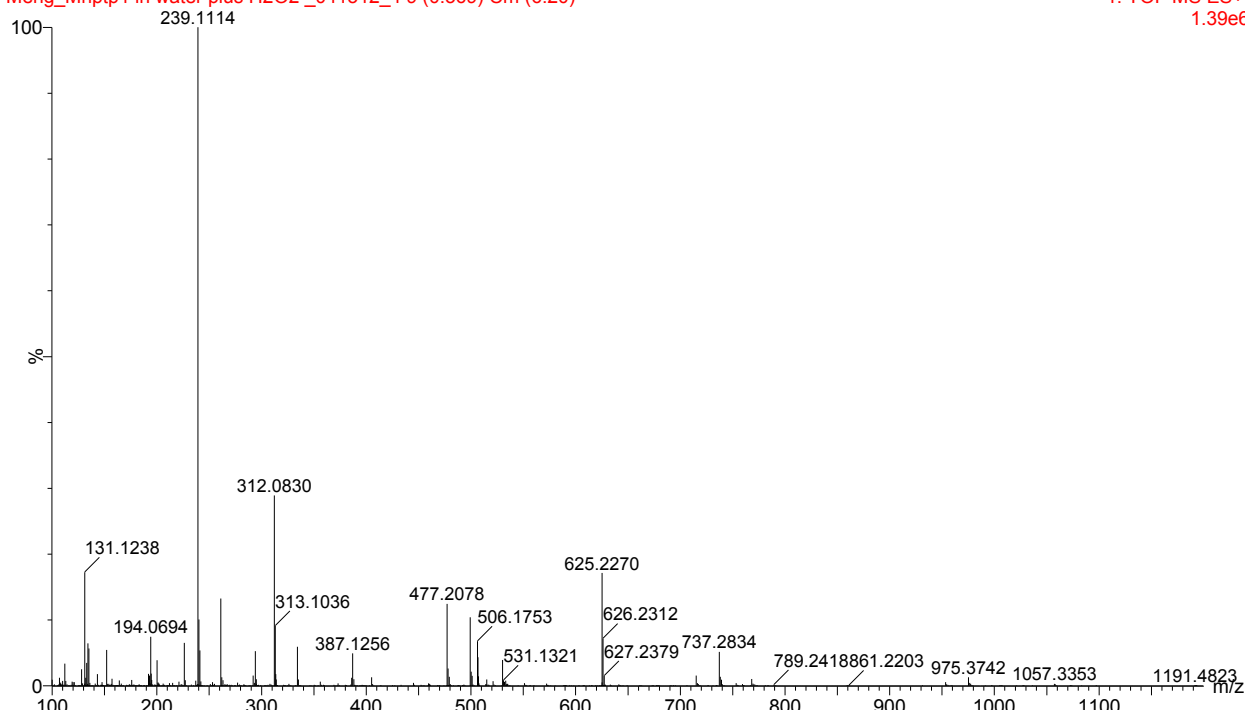


Figure 2A.3. Mass spectrum (ESI) of an aqueous solution containing 1.00 mM $[\text{Mn}(\text{Hptp1})(\text{MeCN})](\text{ClO}_4)_2$ and 10 mM H_2O_2 . The sample also contained 50 mM HEPES and was buffered to pH 7.00. The 506.1753 m/z feature is assigned to $[\text{Mn}_2(\text{ptp1}_2)]^{2+}$, which features a doubly deprotonated coupled ligand. The 625.2270 m/z feature is assigned to $[\text{Mn}_2(\text{Hptp1})(\text{HEPES})]^{2+}$, with both the coupled ligand and HEPES being singly deprotonated.

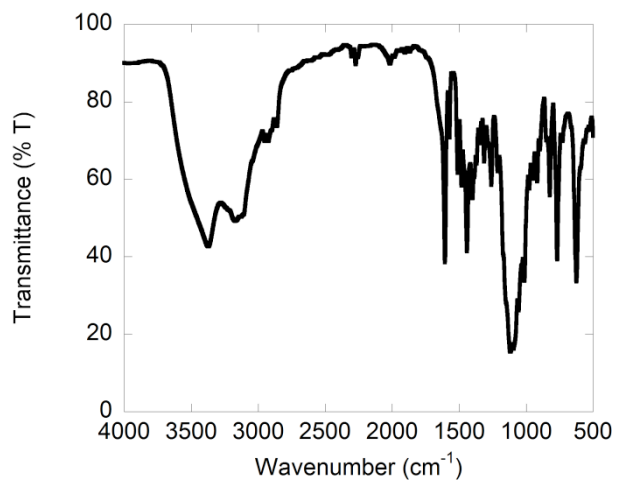


Figure 2A.4. IR spectrum of $[\text{Mn}(\text{Hptp1})(\text{MeCN})](\text{ClO}_4)_2$ (KBr).

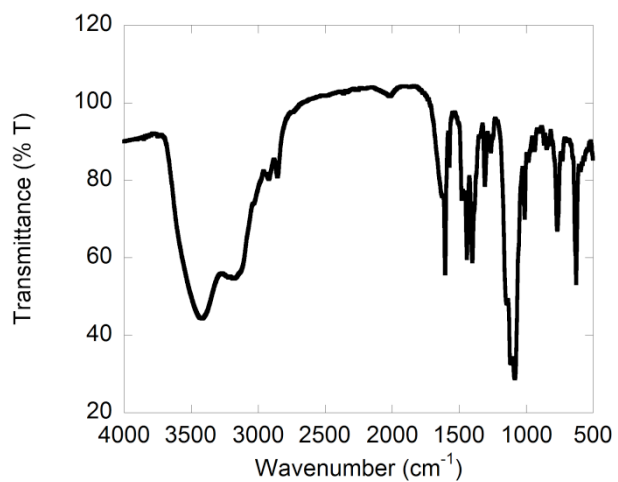


Figure 2A.5. IR spectrum of $[\text{Mn}_2(\text{Hptp1}_2)(\text{MeCN})_2](\text{ClO}_4)_3$ (KBr).

Table 2A.1. Selected crystallographic data for $[\text{Mn}(\text{Hptp1})(\text{MeCN})](\text{ClO}_4)_2$ and $[\text{Mn}_2(\text{Hptp1}_2)(\text{MeCN})_2](\text{ClO}_4)_3$.

Parameter	$[\text{Mn}(\text{Hptp1})(\text{MeCN})](\text{ClO}_4)_2 \cdot 2\text{MeCN} \cdot \text{H}_2\text{O}$	$[\text{Mn}_2(\text{Hptp1}_2)(\text{MeCN})_2](\text{ClO}_4)_3 \cdot \text{MeCN}$
Formula	$\text{C}_{34}\text{H}_{42}\text{Cl}_2\text{MnN}_8\text{O}_{10.15}$	$\text{C}_{62}\text{H}_{68}\text{Cl}_3\text{Mn}_2\text{N}_{13}\text{O}_{14}$
MW	851.04	1435.35
Crystal system	Monoclinic	Triclinic
Space group	$P_{21/m}$ (#60)	$P\bar{1}$ (#2)
a (Å)	12.8799(16)	11.5037(5)
b (Å)	19.833(3)	14.5093(6)
c (Å)	15.6275(19)	22.4086(10)
α (deg)	90	104.436(3)
β (deg)	94.077(3)	95.795(3)
γ (deg)	90	108.249(3)
V (Å ³)	3981.8(9)	3374.2(3)
Z	4	2
Cryst color	Colorless	Colorless
T (K)	183	296
Reflns collected	40149	47287
Unique reflns	7944	9319
R1 (F, I > 2 σ (I))	0.0537	0.0864
wR2 (F ² , all data)	0.1328	0.2434

$$R1 = \frac{\sum ||F_o| - |F_c||}{\sum |F_o|}; wR2 = [\frac{\sum w(F_o^2 - F_c^2)^2}{\sum w(F_o^2)^2}]^{1/2}.$$

Table 2A.2. Selected bond lengths (Å) and bond angles (°) for [Mn(Htp1)(MeCN)](ClO₄)₂.

Bond Length		Angle	
Mn-N(1) ^a	2.2894(18)	N(15)-Mn-O(1)	165.37(6)
Mn-N(8)	2.3902(19)	N(15)-Mn-N(8)	71.71(7)
Mn-N(15)	2.2938(19)	N(15)-Mn-N(18)	103.39(7)
Mn-N(18)	2.3761(18)	N(15)-Mn-N(25)	87.88(7)
Mn-N(25) ^a	2.3278(18)	N(15)-Mn-N(32)	79.79(7)
Mn-N(32) ^b	2.390(2)	N(25)-Mn-O(1)	79.29(6)
Mn-O(1)	2.3658(16)	N(25)-Mn-N(8)	135.33(7)
C(32)-O(1)	1.391(3)	N(25)-Mn-N(18)	72.36(7)
Angle		N(25)-Mn-N(32)	81.86(7)
N(1)-Mn-O(1)	78.30(6)	N(18)-Mn-N(8)	74.42(7)
N(1)-Mn-N(8)	71.45(6)	N(18)-Mn-N(32)	153.79(7)
N(1)-Mn-N(15)	111.70(7)	O(1)-Mn-N(8)	122.57(6)
N(1)-Mn-N(18)	118.77(6)	O(1)-Mn-N(18)	79.51(6)
N(1)-Mn-N(25)	152.30(7)	O(1)-Mn-N(32)	91.37(6)
N(1)-Mn-N(32)	82.62(7)	N(8)-Mn-N(32)	129.92(7)

^aBond between Mn(II) and a pyridine ring from the Htp1 ligand. ^bBond between Mn(II) and an MeCN molecule.

Table 2A.3. Selected bond lengths (Å) for [Mn₂(Htp1₂)(MeCN)₂](ClO₄)₃.

Bond	Length	Bond	Length
Mn(1)-N(2) ^a	2.313(5)	Mn(2)-N(1) ^a	2.299(5)
Mn(1)-N(3) ^b	2.362(4)	Mn(2)-N(8) ^b	2.379(4)
Mn(1)-N(4)	2.423(4)	Mn(2)-N(9)	2.401(4)
Mn(1)-N(5)	2.404(4)	Mn(2)-N(10) ^b	2.445(4)
Mn(1)-N(6)	2.451(4)	Mn(2)-N(11)	2.423(5)
Mn(1)-N(7) ^b	2.317(4)	Mn(2)-N(12)	2.303(4)
Mn(1)-O(14)	2.134(3)	Mn(2)-O(13)	2.156(3)
C(1)-O(14)	1.356(6)	C(2)-O(13)	1.363(6)

^aBond between Mn(II) and an MeCN molecule. ^bBond between Mn(II) and a pyridine ring from the Htp1₂⁻ ligand.

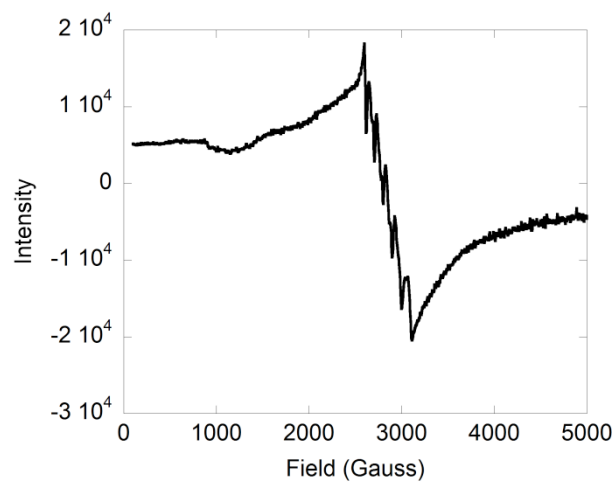


Figure 2A.6. X-Band electron paramagnetic resonance spectra of 1.0 mM $[\text{Mn}(\text{Htp1})(\text{MeCN})](\text{ClO}_4)_2$ in an aqueous solution containing 50 mM HEPES buffered to 7.0. The spectrum was acquired at 77 K. For the Mn(II) complex, the $g_{\text{eff}} = 2.41$, $A = 49$.

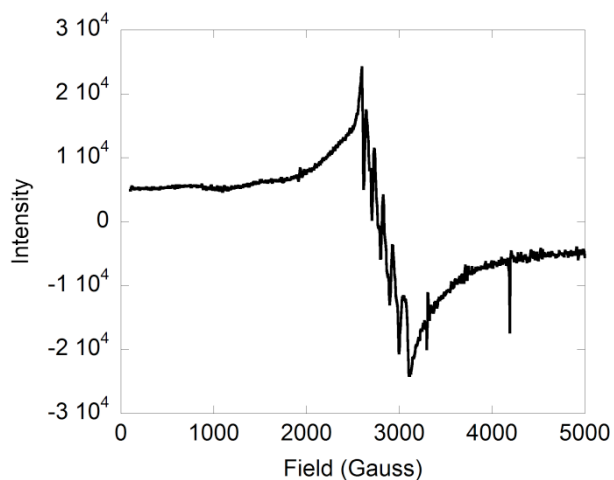


Figure 2A.7. X-Band electron paramagnetic resonance spectra of 0.50 mM $[\text{Mn}_2(\text{Hptp}1_2)(\text{MeCN})_2](\text{ClO}_4)_3$ in an aqueous solution containing 50 mM HEPES buffered to 7.0. The binuclear compound was generated from the reaction between 10 mM H_2O_2 and 1.0 mM $[\text{Mn}(\text{Hptp}1)(\text{MeCN})](\text{ClO}_4)_2$. The spectrum was acquired at 77 K. For the binuclear Mn(II) complex, the $g_{\text{eff}} = 2.04$, $A = 44$. The sharp features at ~ 3300 and 4195 gauss are due to nitrogen bubbles and are not reproducible. The signal intensity, calculated via the double integration of the above first-derivative spectrum, was within 5% of that measured for the reduced precursor in **Figure 2A.6**.

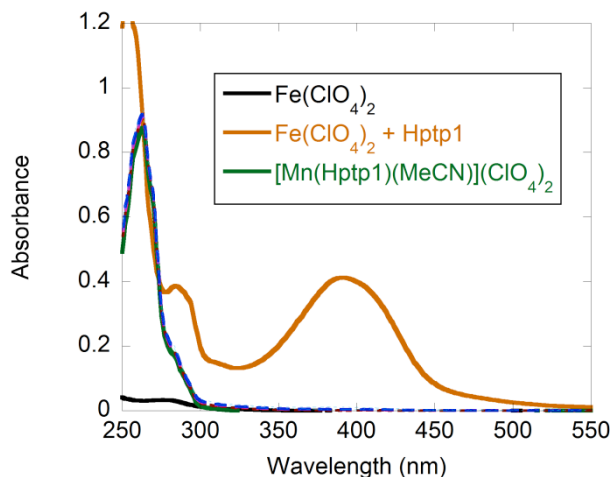


Figure 2A.8. Spectrophotometric analysis of the reaction between 0.10 mM $\text{Fe}(\text{ClO}_4)_2$ and 0.10 mM $[\text{Mn}(\text{Htp1})(\text{MeCN})](\text{ClO}_4)_2$ in MeCN at 25 °C. The UV/vis spectra of 0.10 $\text{Fe}(\text{ClO}_4)_2$ (black), the product of the reaction between 0.10 mM $\text{Fe}(\text{ClO}_4)_2$ and 0.10 mM Htp1 (orange), and $[\text{Mn}(\text{Htp1})(\text{MeCN})](\text{ClO}_4)_2$ (green) are provided for comparative purposes. Solid $\text{Fe}(\text{ClO}_4)_2$ was added to the solution of 0.10 mM $[\text{Mn}(\text{Htp1})(\text{MeCN})]^{2+}$; the mixture was scanned at 0 min (dashed red), 5 min (dashed pink), 10 min (dashed purple), 20 min (dashed dark blue), 30 min (dashed light blue), and 60 min (dashed blue). Over this time period, noticeable displacement of the Mn(II) by Fe(II) does not occur.

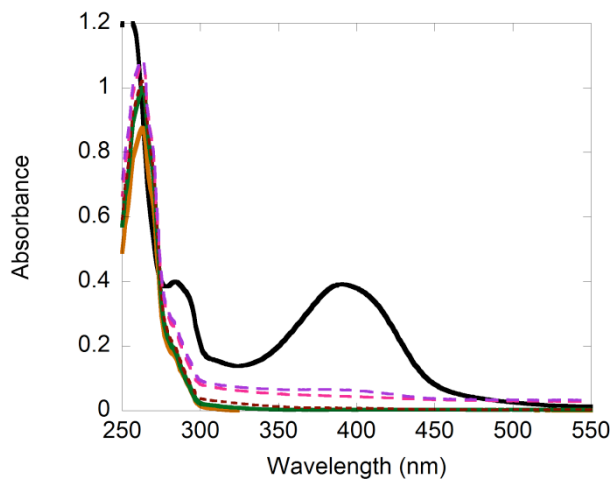


Figure 2A.9. Longer range analysis of the reaction between 0.10 mM $\text{Fe}(\text{ClO}_4)_2$ and 0.10 mM $[\text{Mn}(\text{Htp1})(\text{MeCN})]^{2+}$ in MeCN at 25 °C. The spectra correspond to the following time points: 0 min (green), 60 min (brown), 190 min (pink), 18 h (purple). The spectra of the Mn(II) (orange) and Fe(II) (black) complexes with Htp1 are again provided for reference. At 18 h, approximately 17% of the Mn(II) has been displaced by Fe(II).

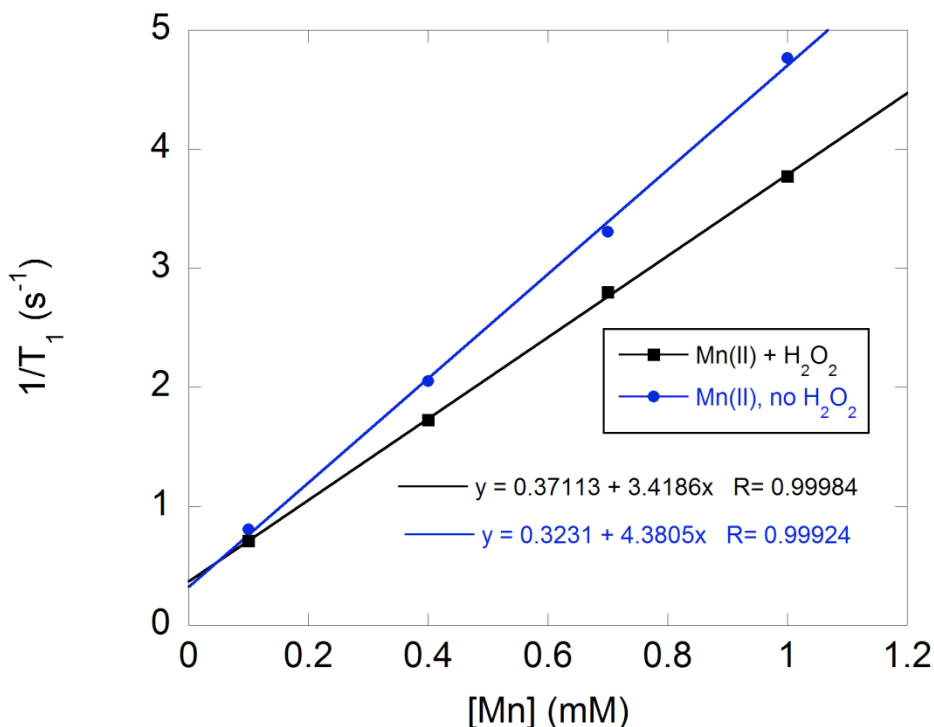


Figure 2A.10. Plots of $(1/T_1)$ as functions of Mn(II) concentration for $[\text{Mn}(\text{Htp1})(\text{MeCN})](\text{ClO}_4)_2$ in the presence (black) and absence (blue) of 10 mM H_2O_2 . All samples were run in aqueous solutions containing 50 mM HEPES buffered to pH 7.00. The data were fit to the indicated linear equations; the y-intercepts were within error of $1/T_1$ measurements associated with two samples that contained no Mn(II): (A) 10 mM H_2O_2 in 50 mM HEPES buffer and (B) pure 50 mM HEPES buffer (both 0.46 s^{-1}). A second series of experiments provided data consistent with r_1 values of $4.41 \text{ mM}^{-1} \text{ s}^{-1}$ and $3.76 \text{ mM}^{-1} \text{ s}^{-1}$ for the reduced and oxidized forms of the sensor, respectively.

as is

Meng_MnTPBEN 2,4-dimethylphenol Oxidized Solution_012712_4 6 (0.240) Cm (5:8)

1: TOF MS ES+
7.52e4

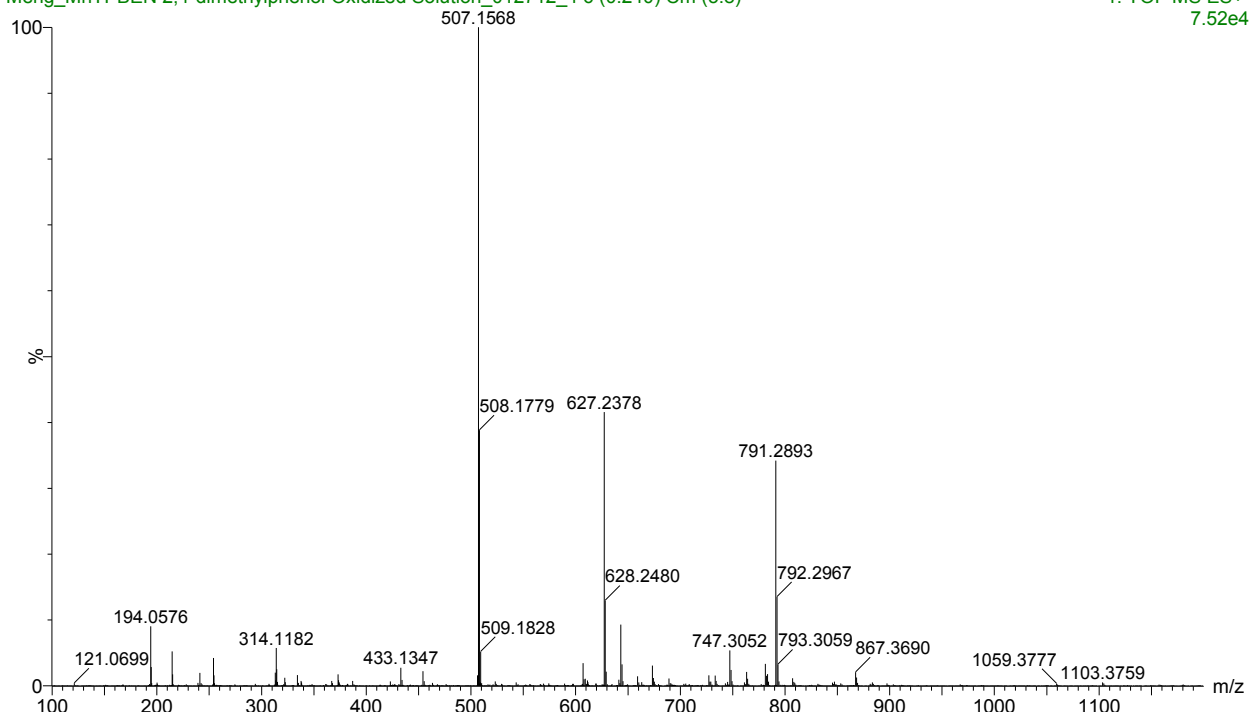


Figure 2A.11. Mass spectrum (ESI) for a sample containing 1.00 mM $[\text{Mn}(\text{Htp1})(\text{MeCN})](\text{ClO}_4)_2$, 1.50 mM H_2O_2 , and 1.00 mM 2,4-dimethylphenol (dmp) in MeCN. The 627.2378 m/z feature is assigned to $[\text{Mn}(\text{Htp1-dmp})]^+$, in which the Htp1 ligand is coupled to the dmp.

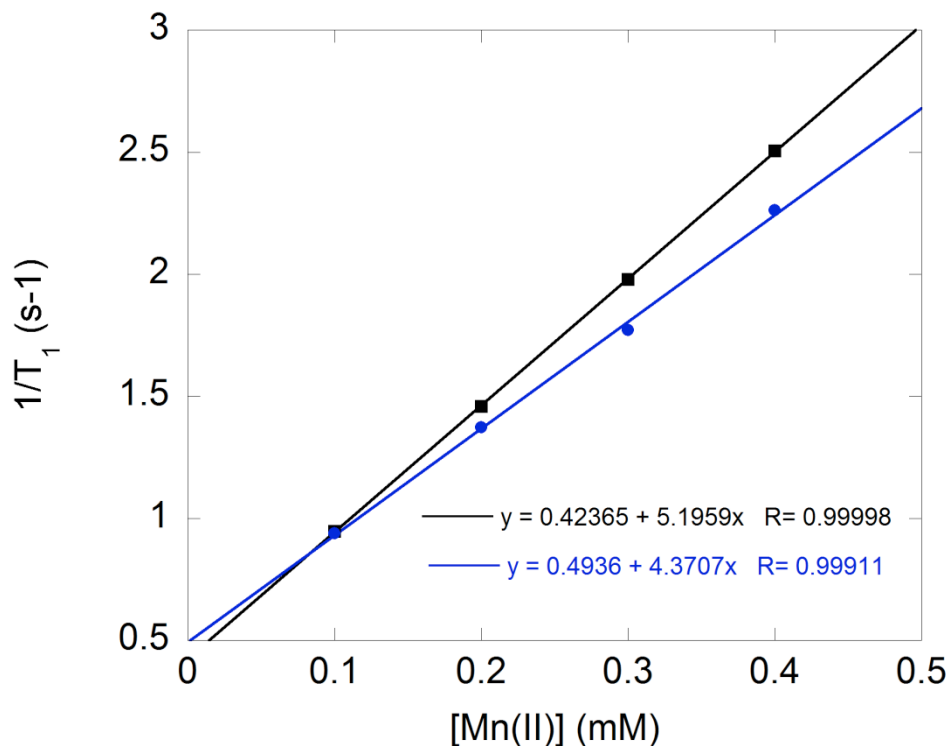


Figure 2A.12. Plots of $(1/T_1)$ as functions of Mn(II) concentration for $[\text{Mn}(\text{Htp1})(\text{MeCN})](\text{ClO}_4)_2$ in the presence (blue) and absence (black) of 10 mM H_2O_2 . All samples were run in aqueous solutions containing 50 mM HEPES buffered to pH 7.00 with 0.10 mM bovine serum albumin (BSA) present. The data were fit to the indicated linear equations; the y-intercepts were within error of $1/T_1$ measurements for three samples that contained no Mn(II): (A) 10 mM H_2O_2 in 50 mM HEPES buffer, (B) 10 mM H_2O_2 and 0.10 mM BSA in 50 mM HEPES buffer, and (C) pure 50 mM HEPES buffer (all 0.51 s^{-1}).

References

- (1) Fearon, I. M.; Faux, S. P. *J. Mol. Cell. Cardiol.* **2009**, *47*, 372-381.
- (2) Kinnula, V. L. *Curr. Drug Targets. Inflamm. Allergy* **2005**, *4*, 465-470.
- (3) Tretter, L.; Sipos, I.; Adam-Vizi, V. *Neurochem. Res.* **2004**, *29*, 569-577.
- (4) Mosley, R. L.; Benner, E. J.; Kadiu, I.; Thomas, M.; Boska, M. D.; Hasan, K.; Laurie, C.; Gendelman, H. E. *Clin. Neurosci. Res.* **2006**, *6*, 261-281.
- (5) Roberts, C. K.; Sindhu, K. K. *Life Sci.* **2009**, *84*, 705-712.
- (6) Wang, J.-Y.; Wen, L.-L.; Huang, Y.-N.; Chen, Y.-T.; Ku, M.-C. *Curr. Pharm. Des.* **2006**, *12*, 3521-3533.
- (7) Chang, M. C. Y.; Pralle, A.; Isacoff, E. Y.; Chang, C. J. *J. Am. Chem. Soc.* **2004**, *126*, 15392-15393.
- (8) Lim, M. H.; Xu, D.; Lippard, S. J. *Nat. Chem. Biol.* **2006**, *2*, 375-380.
- (9) Lippert, A. R.; Van de Bittner, G. C.; Chang, C. J. *Acc. Chem. Res.* **2011**, *44*, 793-804.
- (10) Maeda, H.; Yamamoto, K.; Nomura, Y.; Kohno, I.; Hafsi, L.; Ueda, N.; Yoshida, S.; Fukuda, M.; Fukuyasu, Y.; Yamauchi, Y.; Itoh, N. *J. Am. Chem. Soc.* **2004**, *127*, 68-69.
- (11) Miller, E. W.; Albers, A. E.; Pralle, A.; Isacoff, E. Y.; Chang, C. J. *J. Am. Chem. Soc.* **2005**, *127*, 16652-16659.
- (12) Page, S. E.; Wilke, K. T.; Pierre, V. C. *Chem. Commun.* **2010**, *46*, 2423-2425.
- (13) Ahn, H.-Y.; Fairfull-Smith, K. E.; Morrow, B. J.; Lussini, V.; Kim, B.; Bondar, M. V.; Bottle, S. E.; Belfield, K. D. *J. Am. Chem. Soc.* **2012**, *134*, 4721-4730.
- (14) Utsumi, H.; Yamada, K.-i.; Ichikawa, K.; Sakai, K.; Kinoshita, Y.; Matsumoto, S.; Nagai, M. *Proc. Nat. Acad. Sci., U. S. A.* **2006**, *103*, 1463-1468.
- (15) De Leon-Rodriguez, L. M.; Lubag, A. J. M.; Malloy, C. R.; Martinez, G. V.; Gillies, R. J.;

- Sherry, A. D. *Acc. Chem. Res.* **2009**, *42*, 948-957.
- (16) Duimstra, J. A.; Femia, F. J.; Meade, T. J. *J. Am. Chem. Soc.* **2005**, *127*, 12847-12855.
- (17) Major, J. L.; Meade, T. J. *Acc. Chem. Res.* **2009**, *42*, 893-903.
- (18) Szabó, I.; Geninatti Crich, S.; Alberti, D.; Kálmán, F. K.; Aime, S. *Chem. Commun.* **2012**, *48*, 2436-2438.
- (19) Zhang, X.; Lovejoy, K. S.; Jasonoff, A.; Lippard, S. J. *Proc. Natl. Acad. Sci., U. S. A.* **2007**, *104*, 10780-10785.
- (20) Breckwoldt, M. O.; Chen, J. W.; Stangenberg, L.; Aikawa, E.; Rodriguez, E.; Qiu, S.; Moskowitz, M. A.; Weissleder, R. *Proc. Nat. Acad. Sci., U. S. A.* **2008**, *105*, 18584-18589.
- (21) Querol, M.; Chen, J. W.; Bogdanov, A. A., Jr. *Org. Biol. Chem.* **2006**, *4*, 1887-1895.
- (22) Chen, J. W.; Pham, W.; Weissleder, R.; Bogdanov, A., Jr. *Magn. Reson. Med.* **2004**, *52*, 1021-1028.
- (23) Ratnakar, S. J.; Viswanathan, S.; Kovacs, Z.; Jindal, A. K.; Green, K. N.; Sherry, A. D. *J. Am. Chem. Soc.* **2012**, *134*, 5798-5800.
- (24) Mialane, P.; Nivorojkine, A.; Pratviel, G.; Azéma, L.; Slany, M.; Godde, F.; Simaan, A.; Banse, F.; Kargar-Grisel, T.; Bouchoux, G.; Sainton, J.; Horner, O.; Guilhem, J.; Tchertanova, L.; Meunier, B.; Girerd, J.-J. *Inorg. Chem.* **1999**, *38*, 1085-1092.
- (25) Smith, R. M.; Martell, A. E. *Critical Stability Constants*, 1st ed.; Plenum Press: New York, NY, 1975; Vol. 2, pp 249.
- (26) Lampert, H.; Mikenda, W.; Karpfen, A. *J. Phys. Chem. A* **1997**, *101*, 2254-2263.
- (27) Rocklage, S. M.; Cacheris, W. P.; Quay, S. C.; Hahn, F. E.; Raymond, K. N. *Inorg. Chem.* **1989**, *28*, 477-485.
- (28) Wang, S.; Westmoreland, T. D. *Inorg. Chem.* **2009**, *48*, 719-727.

- (29) Zhang, Q.; Gorden, J. D.; Beyers, R. J.; Goldsmith, C. R. *Inorg. Chem.* **2011**, *50*, 9365-9373.
- (30) Tanaka, H.; Sakata, I.; Senju, R. *Bull. Chem. Soc. Jpn.* **1970**, *43*, 212-215.
- (31) Bandyopadhyaya, A. K.; Sangeetha, N. M.; Maitra, U. *J. Org. Chem.* **2000**, *65*, 8239-8244.
- (32) Yushmanov, V. E.; Tominaga, T. T.; Borissevitch, I. E.; Imasato, H.; Tabak, M. *Magn. Reson. Imaging* **1996**, *14*, 255-261.
- (33) Caravan, P.; Ellison, J. J.; McMurry, T. J.; Lauffer, R. B. *Chem. Rev.* **1999**, *99*, 2293-2352.

Chapter 3

A Mononuclear Manganese(II) Complex Demonstrates a Strategy to Simultaneously Image and Treat Oxidative Stress*

* This Chapter is a revision of a published paper: Meng Yu, Stephen L. Ambrose, Zachary L. Whaley, Sanjun Fan, John D. Gordon, Ronald J. Beyers, Dean D. Schwartz, Christian R. Goldsmith, *Journal of American Chemical Society*, **2014**, *136*, 12836-12839. Reprint with permission. Copyright © 2014 by the American Chemical Society.

3.1 Introduction

The over-production of reactive oxygen species (ROSs), such as H_2O_2 , $\text{O}_2^{\bullet-}$, and hydroxyl radicals, has been associated with several lethal and debilitating health conditions. Heightened oxidative damage to proteins and other biomolecules has been observed in the biopsies and post-mortem examinations of patients suffering from a wide variety of cardiovascular and neurological diseases.¹⁻⁴ Understanding the roles that ROSs play in the progressions of these and other conditions requires probes that can monitor their production and traffic within biological systems. Currently, most sensors capable of directly detecting ROSs rely on either fluorescent or luminescent outputs.⁵⁻⁹ Although these probes provide high spatial resolution, the short wavelengths of light needed to excite the reporter make imaging activity in samples other than thin tissues and cell cultures difficult.

Magnetic resonance imaging (MRI), conversely, uses radio-frequency photons to excite the hydrogen nuclei in water molecules and is commonly used to visualize tissues and organs deep within thicker biological samples. Most small molecule MRI contrast agents shorten the longitudinal relaxation times (T_1) of excited protons, allowing sharper contrast between regions with high and low water contents. The ability to accelerate these relaxations defines the relaxivity (r_1) of the contrast agent. A molecule that displays a different r_1 value upon the addition of an analyte can serve as a sensor when monitored by MRI. Several such MRI contrast agent sensors have been developed,¹⁰⁻¹² but few have been directed towards imaging oxidative activity.¹³⁻¹⁸ The probes capable of detecting oxidants often either require a co-analyte¹³ or display a similar response to O_2 ¹⁴ or another analyte.¹⁸ Recently, our research group reported a mononuclear manganese complex capable of directly detecting H_2O_2 ; notably, the complex lacks a chemical response to O_2 .¹⁶ Upon oxidation, the mononuclear complexes irreversibly couple

into binuclear Mn(II) species. The reaction with H₂O₂ decreases the relaxivity per manganese ion; that the response is a reduction in contrast enhancement limits the probe's ability to resolve different levels of H₂O₂. In the current work, we report a novel manganese-containing MRI contrast agent that responds to H₂O₂ with an altogether different molecular mechanism that results in an increase in the r_1 . As with our prior sensor, the oxidation is directed to the organic portion. This differs from a complex recently reported by Caravan's group in which the manganese reporter toggles between the +2 and +3 oxidation states, depending on the local redox environment; due to the lessened paramagnetism, this sensor has a turn-off response to biologically relevant oxidants.¹⁷

3.2 Experimental Section

Materials

Except where stated otherwise, all chemicals were purchased from Sigma-Aldrich and used as received. 2,2-Diphenyl-1-picryl-hydrazyl hydrate (DPPH) was bought from EMD Millipore. Deuterated acetonitrile (MeCN-*d*₃) was bought from Cambridge Isotopes. Diethyl ether (ether) and methanol (MeOH) were purchased from Fisher. Methylene chloride (CH₂Cl₂) was bought from Mallinckrodt Baker. The H₂qtp1 ligand precursor *N,N,N'*-tris(2-pyridinylmethyl)-1,2-ethanediamine was prepared as described previously.¹⁹ The complex [Mn(Htp1)(MeCN)](ClO₄)₂ (**2**) was synthesized through a previously reported protocol.¹⁷

Instrumentation

All ¹H and ¹³C NMR spectra were recorded on a 400 MHz AV Bruker NMR spectrometer; all reported resonances were referenced to internal standards. Electron paramagnetic resonance (EPR) spectra were collected using a Bruker EMX-6/1 X-band EPR spectrometer operated in the perpendicular mode. The acquired data were analyzed with the

program EasySpin. Each sample was run as a frozen solution in a quartz tube. High-resolution mass spectrometry (HR-MS) data were obtained at the Mass Spectrometer Center at Auburn University on a Bruker microflex LT MALDI-TOF mass spectrometer via direct probe analysis operated in the positive ion mode. IR data were collected using a Shimadzu IR Prestige-21 FT-IR spectrophotometer. A Johnson Matthey magnetic susceptibility balance (model MK I#7967) was used to measure the magnetic properties of the Mn(II) complex with H₂qtp1; the reported μ_{eff} value was the average of those measured for two independently prepared solid samples. Atlantic Microlabs (Norcross, GA) performed the elemental analyses (C, H, N). All samples submitted for elemental analysis were crystallized and dried under vacuum prior to their shipment. All cyclic voltammetry was performed under N₂ at 294 K using an Epsilon electrochemistry workstation (Bioanalytical System, Inc.), a gold working electrode, a platinum wire auxiliary electrode, and a Ag/AgCl reference electrode.

X-Ray Crystallography

The structural data were obtained at the University of Alabama, Birmingham using an Enraf Nonius CAD4 single-crystal diffractometer. After the data were corrected for Lorentz and polarization effects, the structures were solved using direct methods and expanded using Fourier techniques. All non-hydrogen atoms were refined anisotropically. Hydrogen atoms were included at idealized positions 0.95 Å from their parent atoms prior to the final refinement. Further details regarding the data acquisition and analysis are included on Table 3A.1.

Measurement of H₂qtp1 Binding Affinity for Mn(II)

The log(*K*) was measured via a competitive binding assay between *N,N,N',N'*-tetrakis(2-pyridylmethyl)ethylenediamine (TPEN) and H₂qtp1. Various amounts of TPEN were added to solutions of [Mn(H₂qtp1)(MeCN)](OTf)₂(**1**) in MeCN-*d*₃ and D₂O. The ratios of free TPEN to

free H₂qtp1 were assessed by ¹³H NMR. From these data, equilibrium constants of 0.4 were assigned for the reactions in both water and MeCN:



Given the known log(*K*) of 10.3²² for TPEN's binding to Mn(II), a log(*K*) of 10.7 was thereby assigned for the coordination of H₂qtp1 to Mn(II). Given the similarity of the values, we can assume that preferential protonation of either the TPEN or H₂qtp1 ligand does not occur to an extent large enough to impact the competitive binding of Mn(II).

Magnetic Resonance Imaging (MRI)

All MRI data were collected at the Auburn University MRI Research Center (Auburn, AL) on a Siemens Verio open-bore 3-T MRI clinical scanner. A 15-channel knee coil was used to simultaneously image 12-26 samples. An inversion recovery (IR) sequence was used that featured a non-selective adiabatic inversion pulse followed by a slice-selective gradient recalled echo (GRE) readout after a delay period corresponding to the inversion time (TI). The GRE was a saturation readout, such that only one line of k-space was acquired per repetition time (TR). This method was selected to maximize both the signal strength and the accuracy of the *T*₁ estimates. Specific imaging parameters were as follows: TR was set to 4 s, TI was varied from 4.8 to 2500 ms over 37 steps, the echo time (TE) was set to 3.6 ms, the flip angle equaled 90°, averages = 1, slice thickness = 5 mm, field of view = 140 × 140 mm, matrix = 128 × 128, resulting in a pixel size of 1.1 × 1.1 × 5.0 mm. All samples were run in 50 mM solutions of HEPES in water, buffered to pH 7.0 and kept at 22 °C. The manganese content was systematically varied from 0.10 to 1.00 mM. The inverses of the *T*₁ values were plotted versus the concentration of Mn(II) to obtain *r*₁ values. All reported *r*₁ values are averages from the

results of two separate series of experiments. Each series of experiments used a different batch of **1**.

MRI Data Analysis

Image analysis was performed using custom Matlab programs (Mathworks, Natick, MA). The initial TI = 4.8 ms image served as a baseline to determine circular region of interest (ROI) boundaries for each sample; from these, the mean pixel magnitudes for each ROI were calculated. For each of the 36 subsequent TI images, the same ROI boundaries were applied and the mean pixel magnitude calculations were repeated. This gave consistent ROI spatial definitions and a corresponding time course of magnitudes for each of the samples over all the TI time points. Each sample's complex phase was used to correct the magnitude polarity to produce a complete exponential T_1 inversion recovery curve. The Nelder-Mead simplex algorithm was applied to each sample's exponential curve to estimate its corresponding T_1 value.

Analysis of Anti-Oxidant Properties of Mn(II) Complexes

Superoxide was produced *in situ* from a reaction between xanthine and xanthine oxidase. The subsequent reaction of the O_2^- with lucigenin provided a spectroscopic signal that can be used to provide a qualitative measure of an anti-oxidant's ability to degrade O_2^- . The copper/zinc superoxide dismutase isolated from bovine erythrocytes (0.001-100 U/ml, Calbiochem) was used as a positive control. The assay was carried out in a total volume of 1 mL containing 50 mM tris (pH 8.0), hypoxanthine (50 μ M), xanthine oxidase (0.005 U/ml, Calbiochem) and dark adapted lucigenin (5 μ M) in the presence of either **1** or **2** (0.1 nM – 10 μ M) or their vehicle. Reactions were carried out at room temperature and were initiated by the addition of xanthine oxidase to the hypoxanthine-containing solution. Luminescence was measured using a TD-20/20 (Turner Designs) luminometer and expressed as relative light units (RLU). Luminescence was measured

for four 10 s integrations after an initial delay of 3 s. The four RLU values were averaged, and each concentration was expressed as a percent of that produced in the presence of vehicle. Each assay data point was performed in duplicate and assays were repeated three times.

An alternative assessment of the Mn(II) complexes' anti-oxidant properties relied upon the DPPH assay. Aqueous solutions of either **1**, **2**, or ascorbic acid were added to a solution of 0.10 mM DPPH in MeOH, such that the final reaction volume was 0.2 mL. Samples were incubated in the dark for 30 min at room temperature. Spectrophotometric measurements were subsequently performed at 517 nm using a Molecular Devices Spectramax Plus. This wavelength corresponds to the λ_{max} of the reduced product. Experiments were performed in triplicate and repeated twice.

Cytotoxicity Studies.

H9c2 cells were obtained from the American Tissue Type Collection (Manassas, VA, USA) and grown at 37 °C with 95% humidity and 5% CO₂. Cells were grown in Dulbecco's modified eagles medium (DMEM) supplemented with 10% fetal bovine serum. Experiments were performed at 70-80% confluence. All experiments were performed in DMEM in the absence of fetal bovine serum. To determine the cytotoxic effects of **1** and **2**, the H9c2 cells were exposed to increasing concentrations of these reagents or their vehicle in DMEM for either 4 or 24 h. The cell number was assessed using the CyQUANT Cell Proliferation Assay Kit (Life Technologies Corporation, Carlsbad, CA) per manufacturer's instructions. Cell number was expressed as a percentage of that measured for the vehicle-treated cells. Values are expressed as mean and SEM (standard error of the mean) and represent three experiments performed in triplicate.

Syntheses

***N*-(2,5-Dihydroxybenzyl)-*N,N',N'*-tris(2-pyridinylmethyl)-1,2-ethanediamine.**

N,N,N'-Tris(2-pyridinylmethyl)-1,2-ethanediamine (2.31 g, 6.93 mmol) and 2,5-dihydroxybenzaldehyde (1.05 g, 7.63 mmol) were dissolved in 40 mL of 1,2-dichloroethane. Subsequently, NaBH(OAc)₃ (4.43 g, 20.8 mmol) was added as a solid over 1 h. The resultant mixture was stirred for 24 h, at which point 80 mL of saturated NaHCO₃ solution were added to quench the reaction. The crude product was extracted with three 40 mL portions of CH₂Cl₂. The combined extracts were washed with one 40 mL portion of H₂O then dried over anhydrous Na₂SO₄. Evaporation of the solvent yielded the crude product, which was further purified via precipitation from a MeOH/ether mixture to yield a pale yellow powder (1.25 g, 40% yield). ¹H NMR (400 MHz, CDCl₃, 293 K): δ 8.53 (1H, d, *J* = 4.8 Hz), 8.49 (2H, d, *J* = 4.8 Hz), 7.59 (3H, m), 7.50 (2H, d, *J* = 8.0 Hz), 7.23 (1H, d, *J* = 8.0 Hz), 7.13 (3H, m), 6.68 (2H, m), 6.48 (1H, d, *J* = 4.8 Hz), 3.73 (6H, s), 3.59 (2H, s), 2.74 (4H, s). ¹³C NMR (400 MHz, CDCl₃, 293 K): δ 159.11, 157.68, 148.91, 148.83, 136.82, 136.60, 123.51, 123.29, 123.01, 122.43, 122.08, 116.87, 116.34, 115.67, 60.24, 59.53, 56.94, 50.71, 50.66. IR (KBr, cm⁻¹): 3380 (m), 3148 (s), 3126 (s), 2929 (m), 2879 (w), 2718 (w), 2617 (w), 1655 (w), 1596 (m), 1569 (m), 1490 (s), 1435 (s), 1400 (s), 1368 (s), 1249 (m), 1204 (w), 1147 (w), 1009 (w), 936 (w), 860 (w), 826 (w), 817 (w), 760 (s), 713 (w). MS (ESI): Calcd for MH⁺ 456.2400; Found, 456.2341.

Acetonitrilo(*N*-(2,5-dihydroxy-benzyl)-*N,N',N'*-tris(2-pyridinylmethyl)-1,2-ethanediamine)manganese(II) triflate ([Mn(H₂qtp1)(MeCN)](OTf)₂, 1).

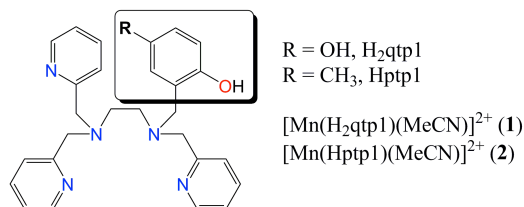
The H₂qtp1 ligand (500 mg, 1.10 mmol) and Mn(OTf)₂ (388 mg, 1.10 mmol) were dissolved in 2 mL of MeCN under N₂. The solution was allowed to stir at room temperature for 16 h. After this time, 2 mL of ether were added to the solution, and the mixture was transferred

to a $-40\text{ }^{\circ}\text{C}$ freezer. The product deposited as a white powder over several hours (660 mg, 74% yield). Crystals suitable for single crystal X-ray diffraction were grown from the diffusion of ether into a saturated solution of the powder in MeCN. Solid-state magnetic susceptibility (295 K): $\mu_{\text{eff}} = 5.6\ \mu_{\text{B}}$. UV/vis (H_2O , 294 K): 262 nm ($9370\ \text{M}^{-1}\ \text{cm}^{-1}$), 292 nm ($2550\ \text{M}^{-1}\ \text{cm}^{-1}$). MS (ESI): Calcd for $[\text{Mn}(\text{L}-\text{H})]^+$, 509.1624 and for $[\text{Mn}(\text{L})(\text{OTf})]^+$, 659.1222; Found, 509.1630 and 659.1226. IR (KBr, cm^{-1}): 3384 (m), 2957 (w), 2858 (w), 2697 (w), 1695 (w), 1605 (s), 1573 (w), 1505 (m), 1483 (m), 1445 (m), 1368 (m), 1346 (m), 1606 (s), 1294 (s), 1249 (s), 1224 (s), 1203 (s), 1170 (s), 1154 (s), 1076 (m), 1030 (s), 1011 (m), 1259 (m), 976 (w), 963 (w), 940 (w), 882 (w), 854 (w), 827 (w), 771 (m), 638 (s), 917 (m), 574 (m), 516 (m), 412 (w). EPR (H_2O , 77 K): $g_{\text{eff}} = 1.98$. Elemental Analysis: Calcd for $\text{C}_{29}\text{H}_{29}\text{N}_5\text{MnF}_6\text{O}_8\text{S}_2 \cdot 2\text{H}_2\text{O}$: C, 41.24%; H, 3.94%; N, 8.29%; Found: C, 41.08%; H, 3.97%; N, 8.28%.

3.3 Results and Discussion

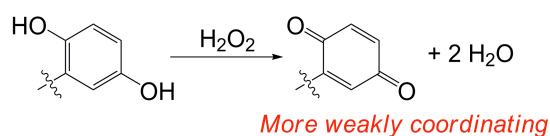
Ligand and Synthesis

For the organic component of the sensor, we synthesized the hexadentate ligand *N*-(2,5-dihydroxybenzyl)-*N,N',N'*-tris(2-pyridinylmethyl)-1,2-ethanediamine ($\text{H}_2\text{qtp1}$, Scheme 3.1). The $\text{H}_2\text{qtp1}$ ligand is prepared in one step from a reaction between the readily synthesized *N,N,N'*-tris(2-pyridinyl-methyl)-1,2-ethanediamine¹⁹ and commercially available 2,5-dihydroxybenzaldehyde. Pure $\text{H}_2\text{qtp1}$ can be obtained through precipitation of the crude from methanol/ether (40% yield).



Scheme 3.1. Ligand structure of **1** and **2**.

At first glance, H₂qtp1 strongly resembles the Hptp1 ligand used for our prior sensor; the latter molecule has a methyl group installed *para* to the phenol hydroxyl group.¹⁶ The substitution of a hydroxyl group for the methyl, however, enables a fundamentally different chemical response to oxidants. The redox-active portion of H₂qtp1 is a quinol, which is anticipated to oxidize to a more weakly metal-coordinating *para*-quinone upon exposure to H₂O₂ (Scheme 3.2) instead of oxidatively coupling to other phenols like Hptp1.¹⁶ Although manganese was not previously known to catalyze quinol oxidation, other redox-active transition metal ions have been reported to do so.^{20, 21} The manganese therefore serves as both the paramagnetic reporter for the contrast agent and the catalyst for the oxidation of the ligand.



Scheme 3.2. Demonstration of quinol oxidation by H₂O₂.

Crystal Structure

The reaction between H₂qtp1 and manganese(II) triflate in anaerobic acetonitrile yields [Mn(H₂qtp1)(MeCN)](OTf)₂ (**1**, MeCN = acetonitrile, OTf⁻ = triflate). In a typical workup, the complex is crystallized from MeCN/Et₂O mixtures in 82% yield. The crystal structure of **1** reveals that the manganese center is heptacoordinate, with six donor atoms from the H₂qtp1 ligand and one from the coordinated MeCN (Figure 3.1). The overall geometry is best described as a distorted face-capped octahedron, with the quinol O-donor and the three pyridine rings' N-donors defining a pseudo-plane. The heptacoordination and the metal-ligand bond distances are both consistent with a +2 oxidation state for the manganese. This assignment is supported by the lack of charge-transfer bands in the optical spectrum and the 5.6 μ_B magnetic moment measured for the solid. The bound quinol remains fully protonated, as evidenced by the anion count and the

Mn–O and C–O bond lengths. The C–O bond distances are both 1.38 Å, closely matching those found for quinols encapsulated in clathrates.²² Each hydroxyl group on the hydroquinone is in close proximity to an O atom from a OTf[−] anion; the O–O distances (2.66 Å for O1, 2.71 Å for O2) are consistent with hydrogen bonding interactions.

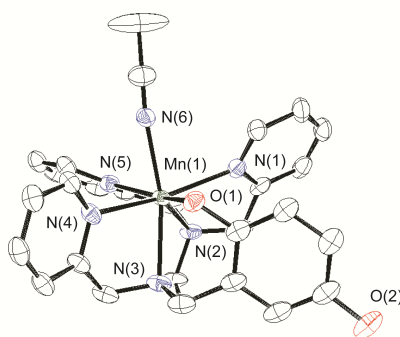


Figure 3.1. Structure of $[\text{Mn}(\text{H}_2\text{qtp1})(\text{MeCN})]^{2+}$. All hydrogen atoms and both triflate counteranions are omitted for clarity. All thermal ellipsoids are drawn at 50% probability. Further details about the structure are provided in the Appendix. (All the CIFs are available on the website of ACS publications free of charge)

Stability

Complex **1** is sufficiently stable in aerobic water solutions to allow MRI measurements. The H₂qtp1 ligand does not dissociate from Mn(II) to a noticeable degree, as assessed by the lack of ¹H NMR resonances in solutions of **1** in D₂O. The log(*K*) for the complexation of H₂qtp1 to Mn(II) was determined through a titration with the metal-scavenging agent TPEN (*N,N,N',N'*-tetrakis(2-pyridinylmethyl)ethylenediamine, log *K* = 10.3).²² The log(*K*) of 10.7 is nearly identical to the 10.6 value measured for a related ligand from our laboratory that contains a *para*-methylphenol group in place of the H₂qtp1's quinol.¹⁶ Solutions of **1** in H₂O or MeCN are slightly sensitive towards oxygen, with the solutions slowly discoloring from light yellow to purple over 12 h. Over this time, collected UV/vis spectra display changes in the region between

200 nm and 300 nm which are consistent with the oxidation of the quinol to a *para*-quinone.²³ Past 24 h, the solution begins to turn brown, consistent with oxidation of the manganese to Mn(III) and/or Mn(IV).

Reaction with H₂O₂

The reactivity between **1** and H₂O₂, conversely, is rapid. In MeCN, the reaction between **1** and excess H₂O₂ turns purple within a few minutes. The corresponding mass spectrum shows new *m/z* peaks at 454.22 and 657.10, which correspond to the oxidized form of the ligand (qtp1) and its manganese complex respectively. The IR spectrum of the solid isolated from the reaction has an intense new absorption at 1658 cm⁻¹, the energy of which is consistent with a carbonyl stretch for a non-metal-coordinated *p*-quinone.^{24, 25} The reactivity is faster in methanol and water than in acetonitrile, with the spectroscopic changes occurring in seconds, rather than minutes.

EPR and UV/vis spectroscopy demonstrate that the oxidation state of manganese doesn't change after adding H₂O₂. The EPR spectra of **1** and its oxidized product are highly similar, with features consistent with high-spin Mn(II). The EPR signal intensity of the Mn(II) in the oxidized product is actually slightly greater than that of an identical concentration of **1**. Upon oxidation, no distinct features are observed in the 350-500 nm region where Mn(III)-related LMCT bands are normally observed.^{26, 27} The lack of ligand resonance peaks in the NMR of the oxidized material in D₂O suggests that the oxidized ligand remains bound to the Mn(II) after the reaction.

Analysis of the oxidized product by ¹H NMR indicates that the ligand does not oxidize to completion, even with excess H₂O₂. The addition of Zn(ClO₄)₂ to MeOH solutions of **1** and its oxidized product leads to rapid metal ion exchange, allowing the visualization of diamagnetic Zn(II)-H₂qtp1 and Zn(II)-qtp1 adducts. Using HQ-COSY spectroscopy, we were able to assign two singlet peaks at 6.56 and 7.09 ppm to the hydroxyl protons of H₂qtp1. Upon oxidation in

MeOH, these peaks decrease in intensity by approximately 45% but do not vanish completely, as would be anticipated from the complete oxidation of the ligand in the sample. The decrease in these features is invariant and seemingly not correlated to the amount of H₂O₂ added past a stoichiometric amount.

MRI Measurement

The relaxivity of complex **1** in an aqueous solution of 50 mM HEPES buffered to pH 7.00 was found to be 4.73 mM⁻¹ s⁻¹ (3 T field, 25 °C). This r_1 value is higher than the 4.39 mM⁻¹ s⁻¹ value measured for the Mn(II) complex with the structurally related Htp1 ligand under identical conditions (Htp1 = *N*-(2-hydroxy-5-methylbenzyl)-*N,N',N'*-tris(2-pyridinylmethyl)-1,2-ethanediamine).¹⁶ The enhanced relaxivity of **1** relative to [Mn(Htp1)(MeCN)](ClO₄)₂ (**2**) may be due to additional interactions with outer-sphere water molecules made possible by the presence of the second hydroxyl group on the quinol.

Upon the addition of 10 mM H₂O₂, the relaxivity per manganese increases from 4.73 mM⁻¹ s⁻¹ to 5.30 mM⁻¹ s⁻¹. Although the change is modest, this represents the first instance of a turn-on response by a mononuclear MRI contrast agent to H₂O₂. We attribute the increase of the relaxivity to the oxidation of the hydroquinone moiety to more weakly coordinating *p*-benzoquinone. In aqueous solution, water molecules should more readily displace the quinone portion of the ligand, resulting in a transiently greater aquation number, which in turn would increase the r_1 .²⁸ This is difficult to ascertain experimentally, given that the broadening of ¹⁷O signals may be attributed to both inner-sphere and outer-sphere interactions with the Mn(II) and that the sensor is only partially oxidized. The partial oxidation also explains the modest r_1 response.

That the same amount of ligand oxidation is observed, even with exceedingly high concentrations of H₂O₂, may suggest that the Mn(II)-qtp1 adduct formed upon oxidation may react with a second equiv. of ROS to return to the reduced state, analogous to a superoxide dismutase (SOD) or catalase enzyme. Evidence does suggest that **1** can catalytically degrade ROSs and behave as an anti-oxidant (*vide infra*). Complex **1** can be fully oxidized by 2,3-dichloro-5,6-dicyano-1,4-benzoquinone (DDQ). The addition of 1 equiv. of DDQ to a solution of **1** is sufficient to completely oxidize the quinol portion of H₂qtp1 to the quinone, as assessed by ¹H NMR. The r_1 value for the fully oxidized sensor is 5.56 mM⁻¹ s⁻¹. The addition of 2 mM KO₂ to **1** likewise triggers a stronger response ($r_1 = 5.52$ mM⁻¹ s⁻¹). The chemical change responsible for the MRI response, however, is not identical to those in the H₂O₂ and DDQ experiments, as confirmed by UV/vis analysis of the reaction. The addition of 10 mM NaClO to solutions of **1**, conversely, does not trigger any changes in the spectroscopic features, and the r_1 value (4.82 mM⁻¹ s⁻¹) remains essentially equal to that of non-oxidized **1**.

Reversibility of Oxidation

There is limited evidence that the oxidation of the sensor can be reversed by reductants. The addition of sodium dithionite to a H₂O₂-oxidized solution of **1** in MeOH changes the color from purple to light yellow; the UV/vis spectrum, however, has a much more intense band around 300 nm, which suggests the formation of a different coordination compound. Further analysis suggests that the ligand's oxidation has been reversed. The IR spectrum of the product lacks the 1658 cm⁻¹ feature indicative of the quinone, and the organic isolated from the reaction mixture appears to be entirely H₂qtp1 on the basis of its ¹H NMR spectrum.

Electrochemistry

Cyclic voltammetry (CV) of **1** in an aqueous solution of phosphate buffered to pH 7.2 reveals two redox features. The lower potential of the two has an $E_{1/2}$ of 115 mV vs. Ag/AgCl and is highly reversible ($\Delta E = 75$ mV, 100 mV/s). Since a comparable redox process is observed in the CV of a Zn(II)-H₂qtp1 adduct, this feature can be firmly assigned to the oxidation and reduction of the H₂qtp1 ligand. This potential translates to 310 vs. NHE, which is both comparable to the M(III)/M(II) reduction potentials of iron and manganese SODs²⁹ and within error of the 300 mV value that is generally accepted to be ideal for the dismutation of O₂⁻.^{30,31} The higher potential feature at 680 mV vs. Ag/AgCl (880 mV vs. NHE) is irreversible. Since an analogous feature is not observed with the zinc analog, we have assigned this to the oxidation of Mn(II) to Mn(III).

Anti-oxidant Properties

As anticipated from the electrochemistry, **1** behaves as a potent SOD mimic (Figure 3.2). The previously prepared **2** was also tested for this activity. The SOD mimicry was assessed using an established procedure that uses xanthine oxidase to produce O₂⁻.^{32,33} Both Mn(II) compounds are extremely effective at degrading O₂⁻, with IC₅₀ values of 11.3 nM (**1**) and 7.7 nM (**2**). These values compare well with those of the best reported mimics for SOD, which are all manganese complexes with electronically modified porphyrin ligands.³²

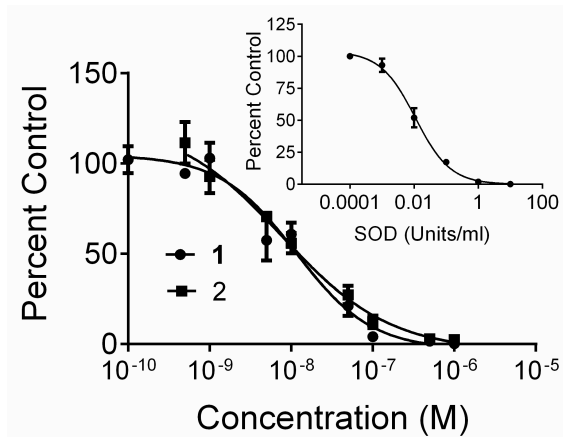


Figure 3.2. Superoxide scavenging effects of **1** and **2**. The Mn(II) complexes are identified by their ligand. Superoxide was generated using a hypoxanthine-xanthine oxidase reaction and detected using the chemiluminescent probe lucigenin. Reactions were carried out in 50 mM Tris-HCl (pH 8.0) containing either **1**, **2**, or Cu/Zn SOD from bovine erythrocytes (insert). Data for the various concentrations of **1**, **2**, and SOD are expressed as a percentage of luminescence in the presence of vehicle.

The anti-oxidant properties of **1** and **2** were also assessed using the DPPH assay (DPPH = 2,2-diphenyl-1-picrylhydrazyl radical hydrate), which evaluates the ability of a compound to donate hydrogen atoms to DPPH to yield the corresponding hydrazine.³⁴⁻³⁶ Although **1** and **2** are similar with respect to their abilities to intercept O_2^- prior to its reaction with lucigenin, the DPPH assay suggests that **1** is the superior anti-oxidant (Figure 3.3). The IC_{50} value for **1** was found to be 6.6 mM; by this measure, it bests the well-known anti-oxidant ascorbic acid (IC_{50} = 22.3 mM). The Hptp1 complex, conversely, fails to reduce DPPH to a noticeable degree.

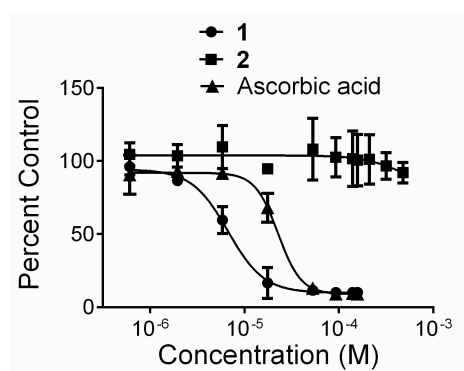


Figure 3.3. DPPH free radical scavenging assay of **1**, **2**, and ascorbic acid. The anti-oxidants were added to DPPH and incubated in the dark for 30 min at room temperature. Spectroscopic measurements were performed at 517 nm. The data were normalized to the absorbance in the presence of vehicle. All experiments were performed in triplicate and repeated twice.

Biological Study

One concern that has limited the application of redox-active metals in biological imaging is that they can elevate ROS concentrations. The results here demonstrate that the opposite can be true and that there exists the potential to simultaneously image and mitigate the oxidative stress caused by aberrantly high concentrations of ROSs. The cytotoxicities of **1** and **2** have been assessed with H9c2 cells. The cells can tolerate 10 mM doses of both compounds for 4 h and a 1.0 mM dose of **1** for 24 h. Higher dosages and/or longer incubation times do trigger noticeable cell death. We currently speculate that the cell death results from the loss of the Mn(II) from the ligand over time.

We attempted to see if **1** could be used to detect and treat oxidative stress in RAW264.7 mouse macrophage and H9C2 rat cardiac cells. Regrettably, the probe does not appear to enter either type of cell. The T_1 values of cells that were treated with **1**, rinsed, then suspended in Hanks Balanced Salt Solution (HBSS) were within error to those for cells that had not been exposed to the probe. EPR analysis of the rinses confirmed that most of the sensor remained in the extracellular fluid. We then attempted to use **1** to detect oxidative stress in the extracellular fluid, but the addition of 200 μM H_2O_2 did not increase the T_1 values of H9C2 cells that were suspended in HBSS containing 100 μM **1**. The results suggest that the sensor will need to be further stabilized and rendered cell permeant before successful *in vivo* imaging or treatment of oxidative stress can be accomplished.

3.4 Conclusions

In summary, we have synthesized a MRI contrast agent that uses a redox-active ligand to signal the presence of H_2O_2 . Unlike our prior sensor, the ligand oxidation appears to be reversible, which may allow related sensors to distinguish highly oxidizing regions within biological samples. We speculate that the ligand oxidation results in a more weakly coordinating

ligand, and that the increase in r_1 results from greater aquation of the manganese. Although the relaxivity change is modest, the results demonstrate the feasibility of this strategy for H_2O_2 detection. Additionally, the $\text{H}_2\text{qtp1}$ complex is a potent anti-oxidant, as assessed by two common assays for such activity. Related compounds may therefore be able to serve as theranostic agents for oxidative stress.

Appendix

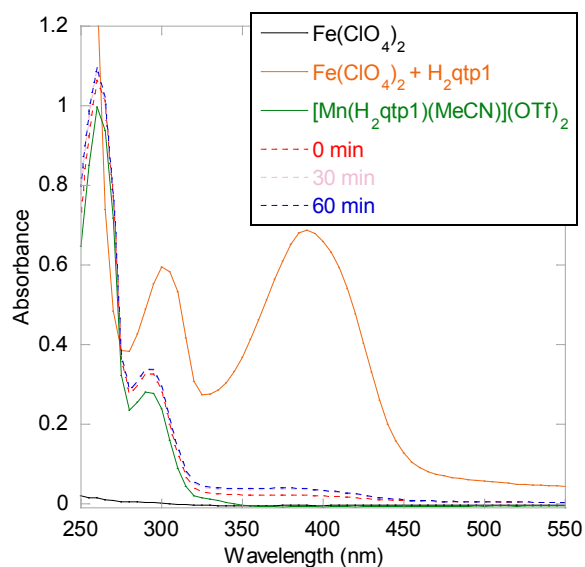


Figure 3A.1. Spectrophotometric analysis of the reaction between 0.10 mM $\text{Fe}(\text{ClO}_4)_2$ and 0.10 mM $[\text{Mn}(\text{H}_2\text{qtp1})(\text{MeCN})](\text{OTf})_2$ in MeCN at 25 °C. The UV/vis spectra of 0.10 mM $\text{Fe}(\text{ClO}_4)_2$ (black), the product of the reaction between 0.10 mM $\text{Fe}(\text{ClO}_4)_2$ and 0.10 mM $\text{H}_2\text{qtp1}$ (orange), and 0.1 mM $[\text{Mn}(\text{H}_2\text{qtp1})(\text{MeCN})](\text{OTf})_2$ (green) are provided for comparative purposes. The $\text{Fe}(\text{ClO}_4)_2$ solution was added to a MeCN solution containing 0.10 mM $[\text{Mn}(\text{H}_2\text{qtp1})(\text{MeCN})]^{2+}$; the mixture was scanned at 0 min (dashed red), 30 min (dashed pink), and 60 min (dashed blue). Over this time period, there was negligible displacement of the Mn(II) by Fe(II).

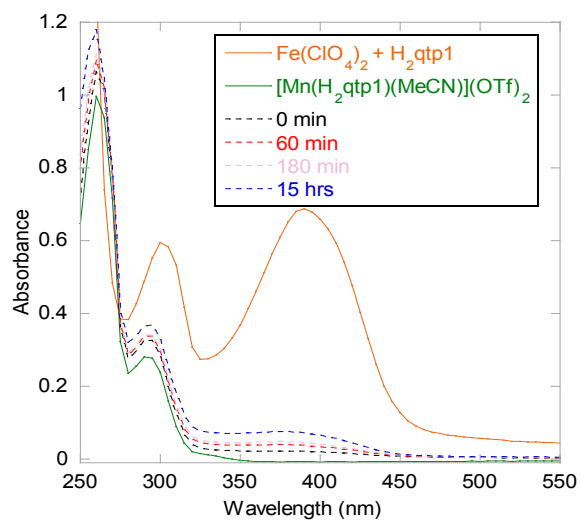


Figure 3A.2. Longer range analysis of the reaction between 0.10 mM $\text{Fe}(\text{ClO}_4)_2$ and 0.10 mM $[\text{Mn}(\text{H}_2\text{qtp1})(\text{MeCN})](\text{OTf})_2$ in MeCN at 25 °C. The spectra correspond to the following time points: 0 min (black), 60 min (red), 180 min (pink), 15 h (blue). The spectra of the $[\text{Mn}(\text{H}_2\text{qtp1})(\text{MeCN})](\text{OTf})_2$ (blue) and Fe(II) (orange) complexes with $\text{H}_2\text{qtp1}$ are again provided for reference. At 15 h, approximately 11% of the Mn(II) has been displaced by Fe(II).

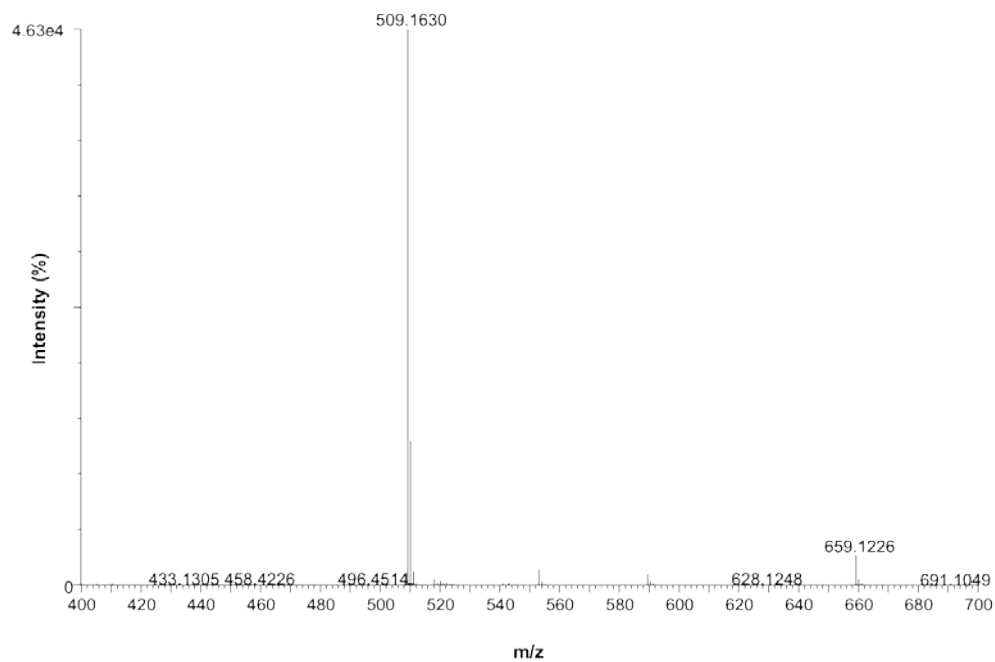


Figure 3A.3. Mass spectrum (ESI) for $[\text{Mn}(\text{H}_2\text{qtp1})(\text{MeCN})](\text{OTf})_2$ (**1**) in MeCN. The 509.1630 m/z feature is assigned to $[\text{Mn}(\text{Hqtp1})]^+$ (calculated m/z = 509.1624). The 659.1226 m/z feature is assigned to $[\text{Mn}(\text{H}_2\text{qtp1})(\text{OTf})]^+$ (calculated m/z = 659.1222).

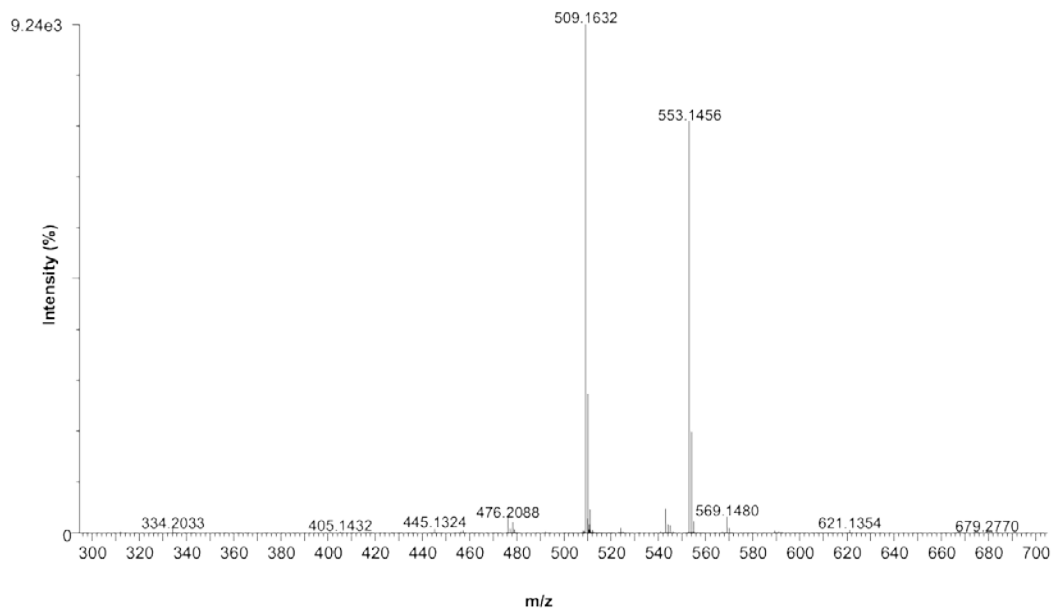


Figure 3A.4. Mass spectrum (ESI) for **1** in MeCN after reaction with 10 equiv of H₂O₂ for 30 min. The 509.1632 m/z feature is assigned to [Mn(Hqtp1)]⁺ (calculated m/z = 509.1624). The 553.1456 m/z feature is assigned to [Mn(qtp1)(HCOO)]⁺ (calculated m/z = 553.1522), where qtp1 is the oxidized quinone form of the H₂qtp1 ligand. Formic acid was present to ionize samples and is the source of the formate.

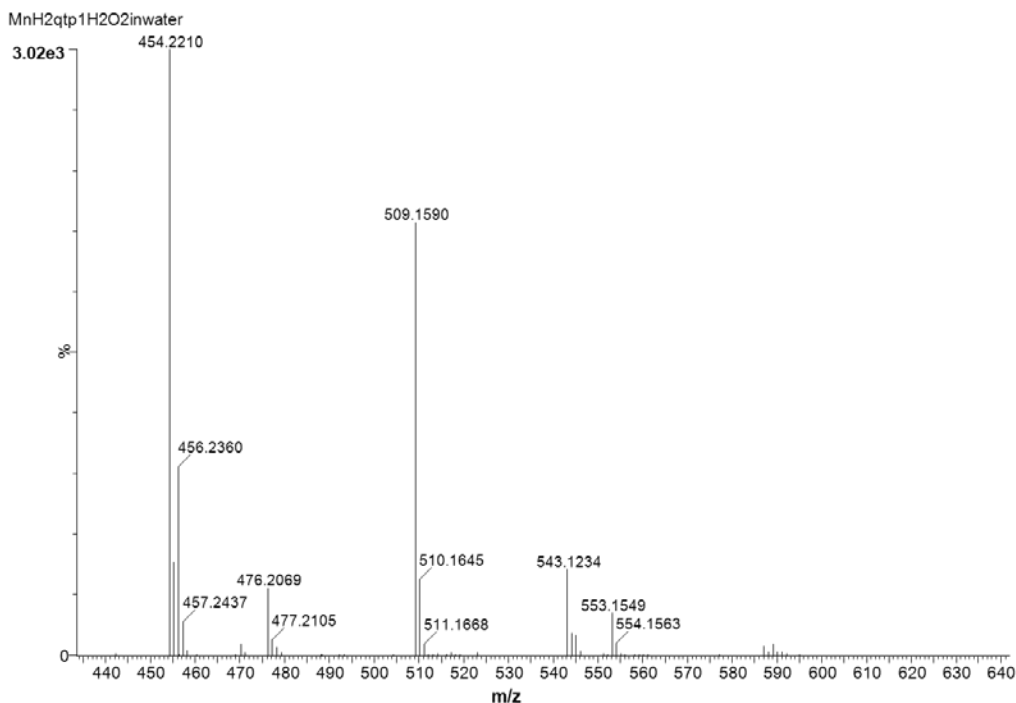


Figure 3A.5. Mass spectrum (ESI) for **1** in H₂O after reaction with 4 equiv. of H₂O₂ for 30 min.

The 454.2210 m/z feature is assigned to (qtp1)⁺ (calculated m/z = 454.2243), where qtp1 is the oxidized (quinone) form of the H₂qtp1 ligand. The 456.2360 m/z feature is assigned to (H₃qtp1)⁺ (calculated m/z = 456.2400). The 476.2069 m/z feature is assigned to (Naqtp1)⁺ (calculated m/z = 476.2063). The 509.1590 m/z feature is assigned to [Mn(Hqtp1)] (calculated m/z = 509.1624). The 553.1549 m/z feature is assigned to [Mn(qtp1)(HCOO)]⁺ (calculated m/z = 553.1522). Formic acid was present to ionize samples and is the source of the formate.

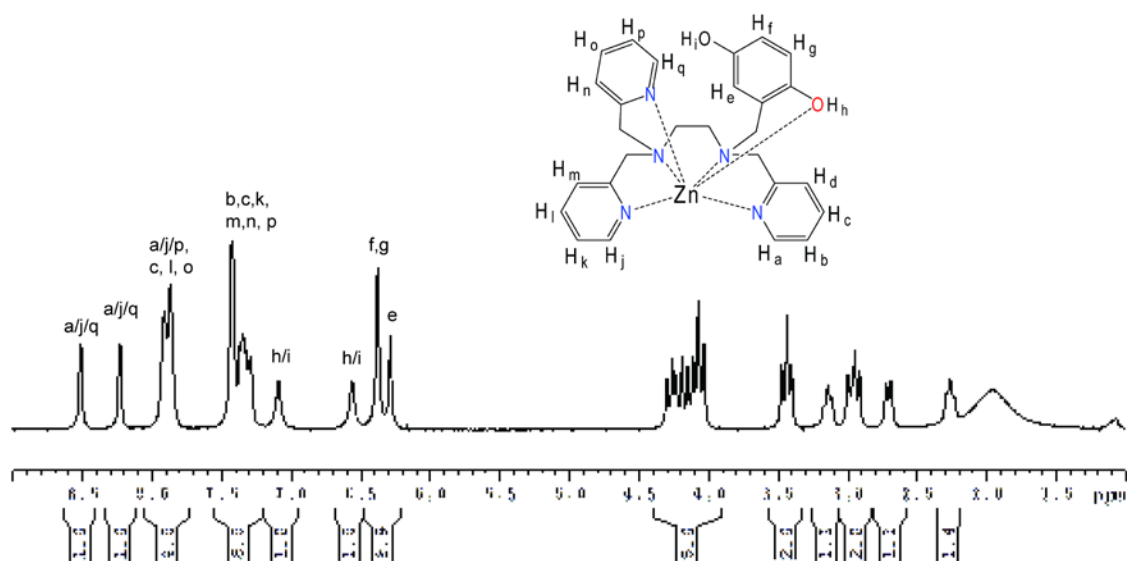


Figure 3A.6. ^1H NMR spectrum of the diamagnetic product from the reaction between 10 mM **1** and 2 equiv of $\text{Zn}(\text{ClO}_4)_2$ in $\text{MeCN-}d_3$. The reaction was given 2 h to equilibrate. Assignments were made with the aid of **Figures 3A.7** and **3A.8**. The two singlets at 7.09 and 6.56 ppm have been assigned to the two protons of the quinol's hydroxyl groups.

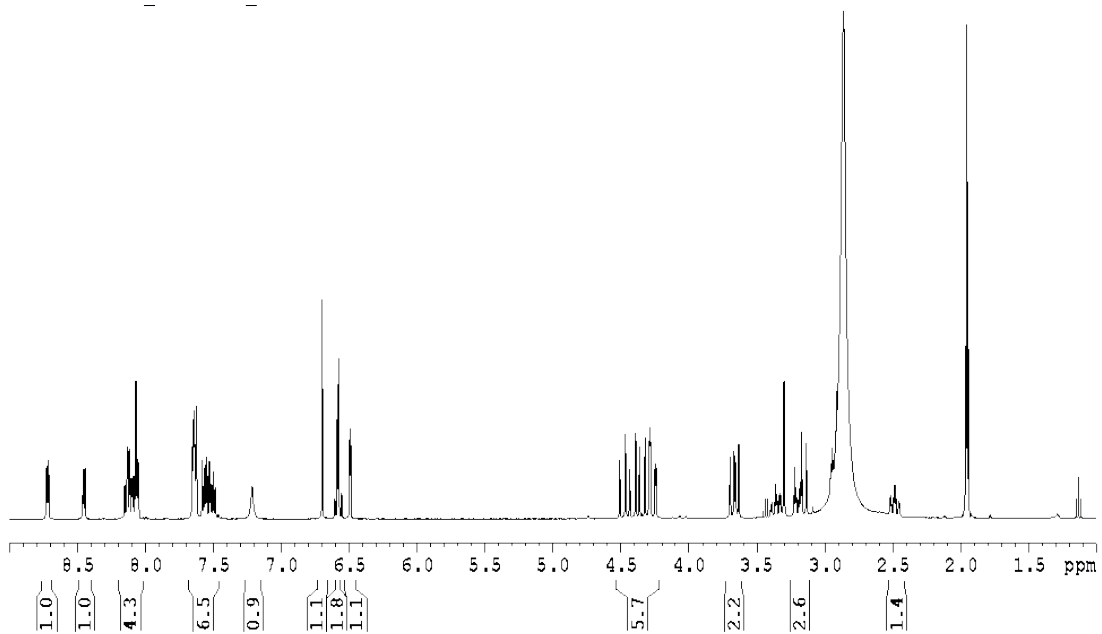


Figure 3A.7. ^1H NMR spectrum of the complex formed from the reaction between 10 mM $\text{H}_2\text{qtp1}$ and 10 mM $\text{Zn}(\text{ClO}_4)_2$ in $\text{MeCN-}d_3$. The two singlets at 7.22 and 6.70 ppm correspond to the protons of the quinol's hydroxyl groups.

Mengyu_02282013_ZnHqtp 2D COSY

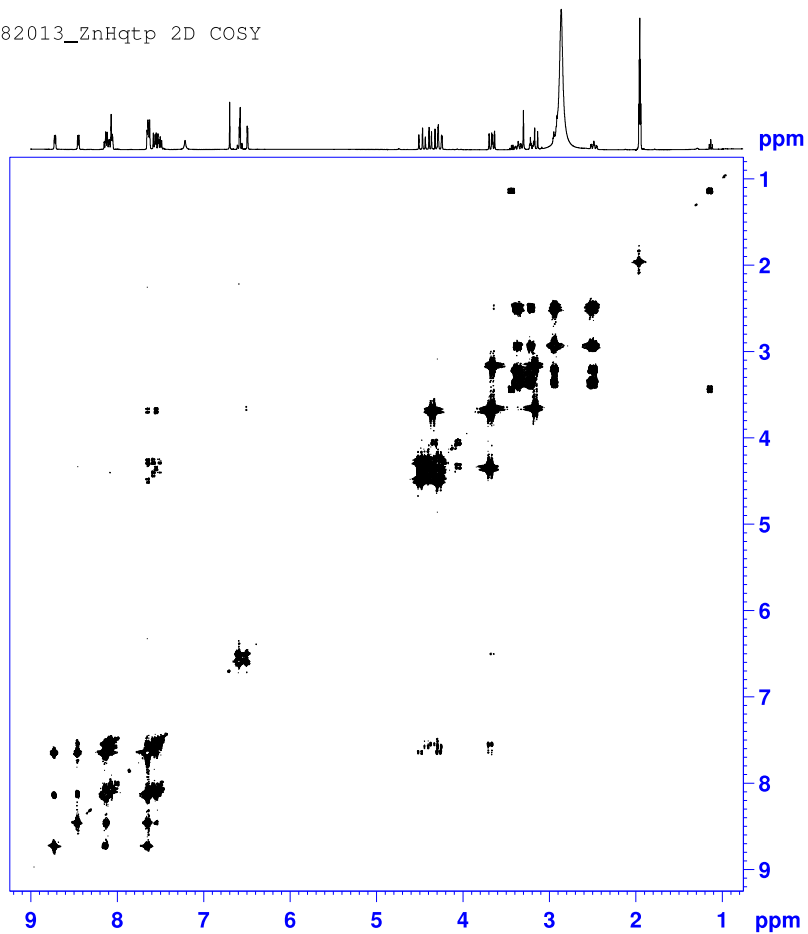


Figure 3A.8. HQ-COSY NMR of the Zn(II)-H₂qtp1 complex from **Figure 3A.7**. The absence of coupling partners for the singlets at 7.22 and 6.70 ppm suggests that they correspond to hydroxyl protons.

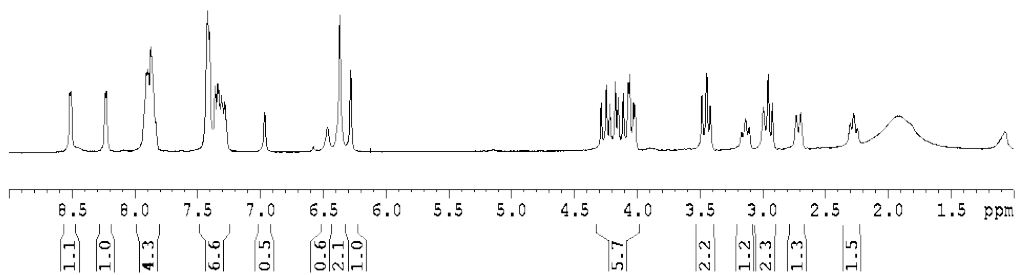


Figure 3A.9. ¹H NMR spectrum of reaction between 10 mM **1** and 4.0 equiv of H₂O₂ in MeCN-*d*₃. After 30 min, 20 mM of Zn(ClO₄)₂ was added to obtain diamagnetic peaks for ¹H NMR. The integrated intensities of the quinol peaks at 6.97 and 6.47 ppm are 0.54 and 0.57, suggesting ~ 55% oxidation of the H₂qtp1 ligand.

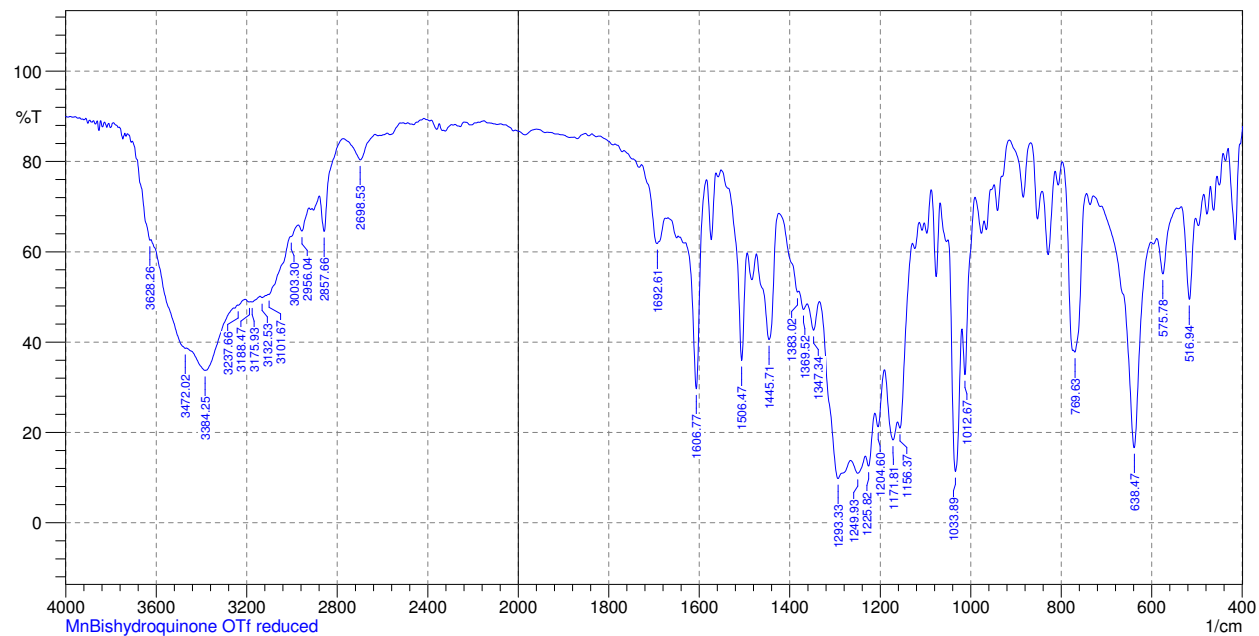


Figure 3A.10. IR spectrum of **1** (KBr). The 3384 and 3472 cm^{-1} features are assigned to the O-H stretches of the $\text{H}_2\text{qtp1}$ quinol. The 1607 cm^{-1} feature is assigned to the C-N stretches for the coordinated pyridine rings.

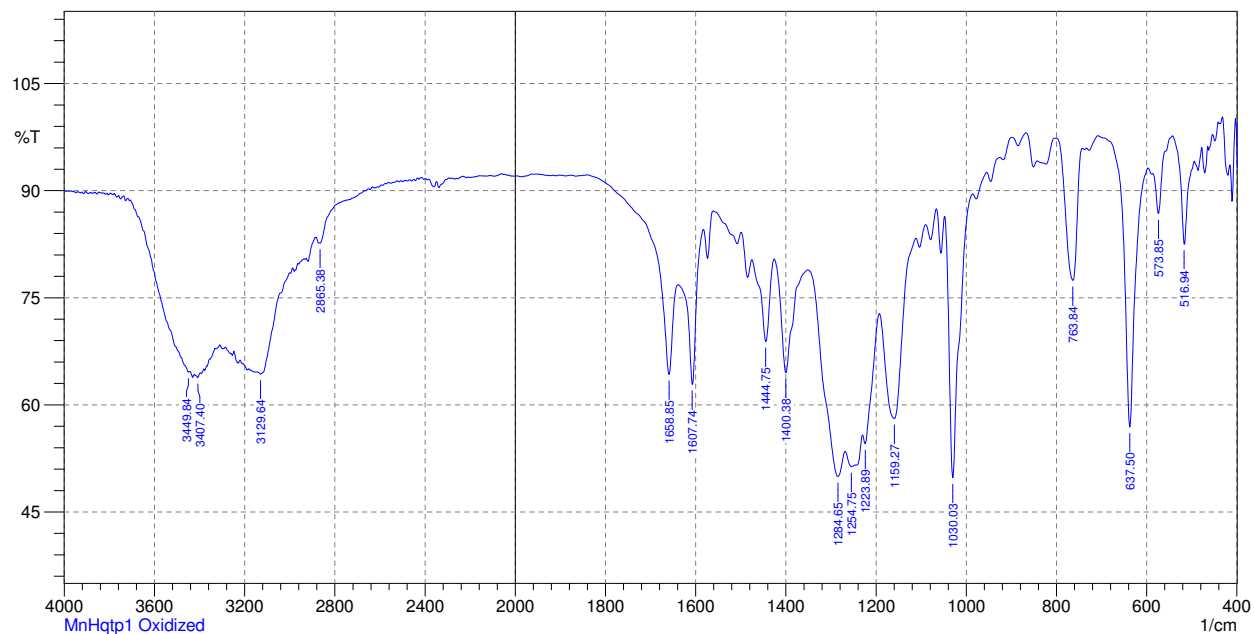


Figure 3A.11. IR spectrum of the crude product from the reaction between 1.0 mM **1** and 4.0 mM H₂O₂ in MeOH. After allowing 1 h to react, the solvents were stripped, yielding the solid used to prepare the sample (KBr). The peak at 1659 cm⁻¹ is assigned to a C=O stretch for the quinone formed upon oxidation.

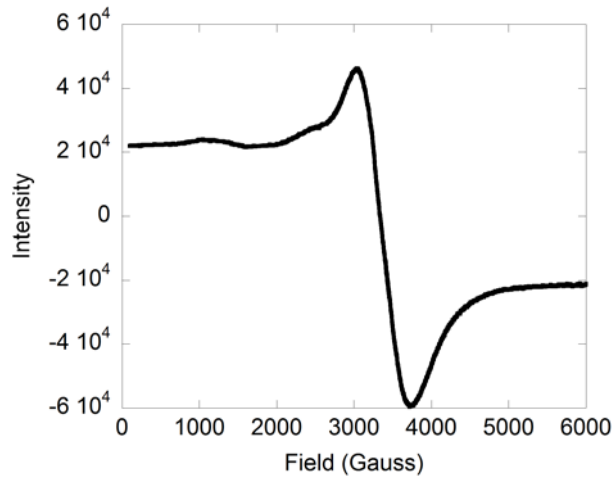


Figure 3A.12. X-band EPR spectrum of a water solution containing 1.0 mM of **1**. The spectrum was acquired at 77 K. $g_{eff} = 1.98$.

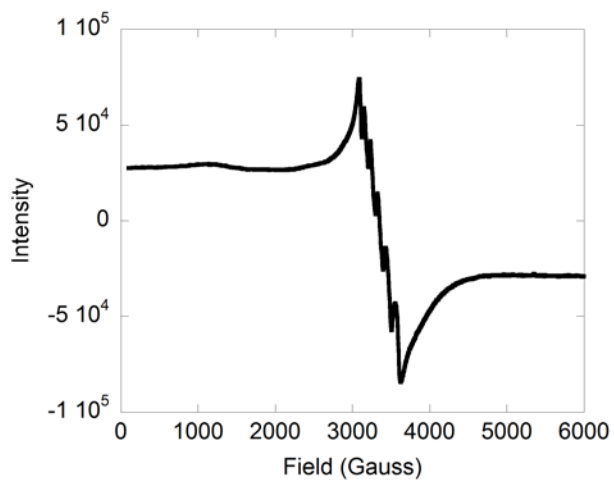


Figure 3A.13. X-band EPR spectrum of the reaction between 1.0 mM **1** and 10 mM H_2O_2 in water. The spectrum was acquired at 77 K. $g_{eff} = 2.00$, $A = 93$ Gauss.

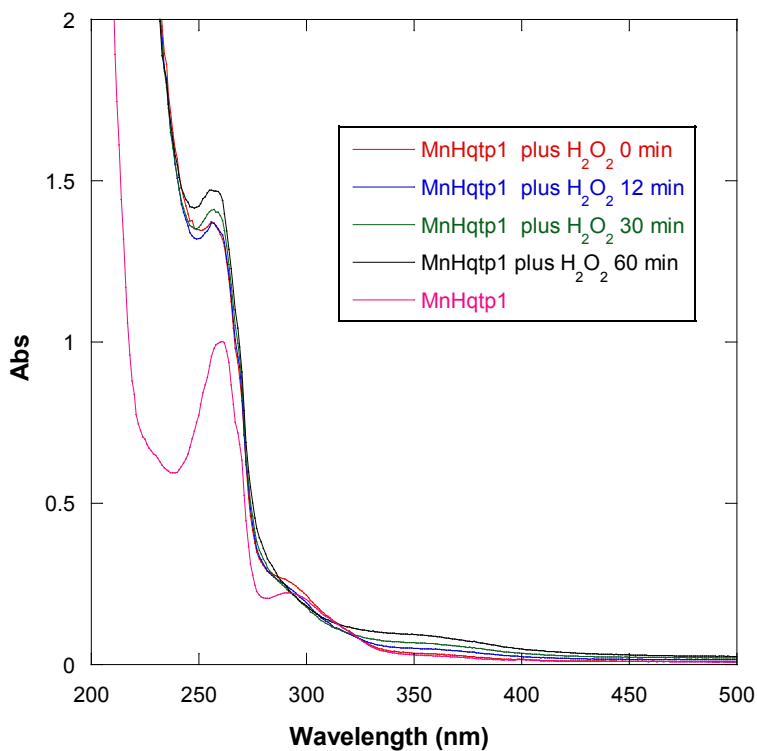


Figure 3A.14. UV/Vis spectra depicting the reaction between 0.10 mM **1** and 10 mM H₂O₂ in H₂O. The reaction was scanned immediately after the addition of H₂O₂, then 12, 30, and 60 min thereafter. The 292 nm feature in the non-oxidized material is typical of a quinol functional group.

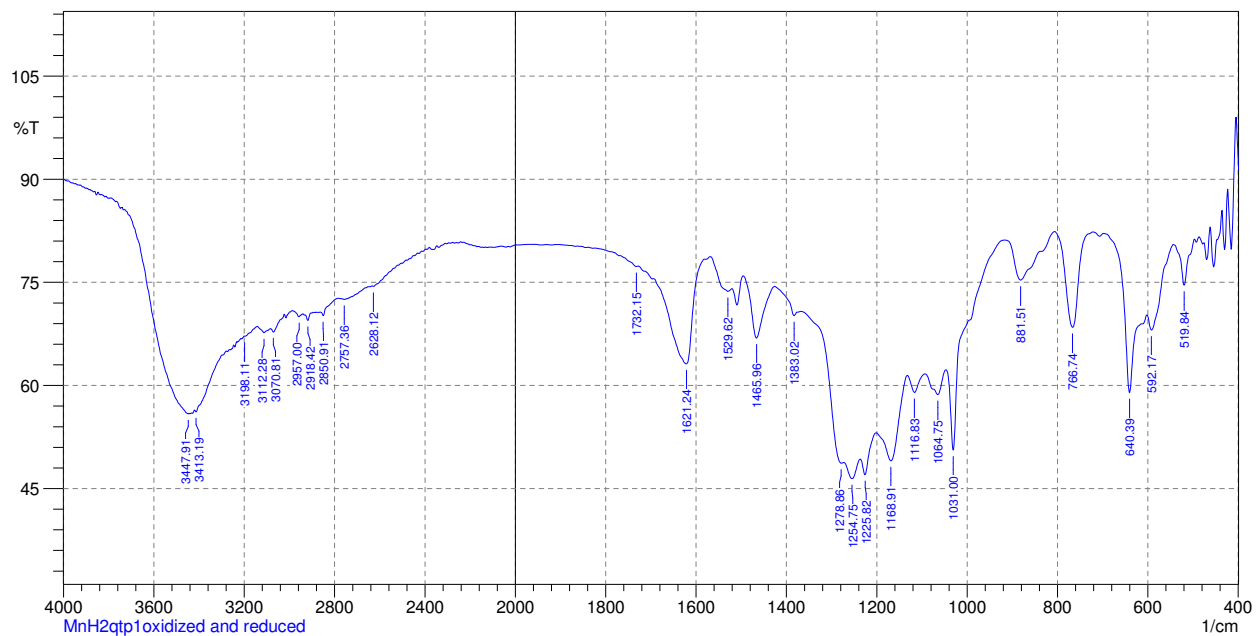


Figure 3A.15. IR spectrum of the product of the reaction between dithionite and the oxidized form of **1**. The sample was prepared by first reacting 10 mM **1** with 40 mM H₂O₂ for 1 h in MeOH then 40 mM of sodium dithionite for 30 min in MeOH. The solvent was stripped to yield the solid product for the KBr pellet.

Table 3A.1. Selected crystallographic data for **1**.

Parameter	[Mn(H ₂ qtp1)(MeCN)](OTf) ₂
Formula	C ₃₁ H ₃₁ F ₆ MnN ₆ O ₈ S ₂
MW	848.70
Crystal system	Monoclinic
Space group	<i>P2₁/n</i> (#14)
a (Å)	13.08640(10)
b (Å)	19.3897(2)
c (Å)	14.42960(10)
α (deg)	90
β (deg)	96.1260(10)
γ (deg)	90
V (Å ³)	3640.48(5)
Z	4
Cryst color	Colorless
T	100
Reflns collected	21924
Unique reflns	5605
R1 (F, I > 2σ(I))	0.1098
wR2 (F ² , all data)	0.3183

$$R1 = \frac{\sum ||F_o| - |F_c||}{\sum |F_o|}; wR2 = [\frac{\sum w(F_o^2 - F_c^2)^2}{\sum w(F_o^2)^2}]^{1/2}.$$

Table 3A.2. Selected bond lengths for **1**.

Bond	Length (Å)	Bond	Length (Å)
Mn-N(1)	2.299(5)	Mn-N(6)	2.284(5)
Mn-N(2)	2.401(5)	Mn-O(1)	2.319(5)
Mn-N(3)	2.306(5)	C(27)-O(1)	1.379(8)
Mn-N(4)	2.325(5)	C(24)-O(2)	1.363(9)
Mn-N(5)	2.382(5)		

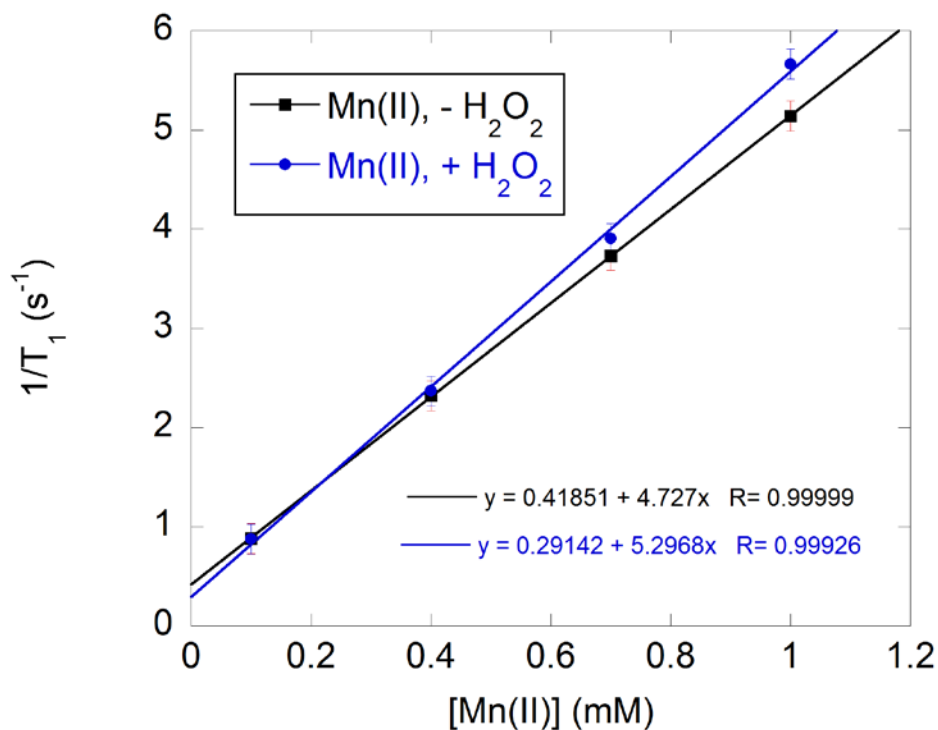


Figure 3A.16. Plots of $(1/T_1)$ versus Mn(II) concentration for **1** in the presence (blue) and absence (black) of 10 mM H_2O_2 . All samples were run in 298 K aqueous solutions containing 50 mM HEPES buffered to pH 7.00, using a 3 T field provided by a clinical MRI scanner. The data were fit to the indicated linear equations; the y-intercepts were within error of $1/T_1$ measurements associated with two control samples that contained no Mn(II): (A) 10 mM H_2O_2 in 50 mM HEPES buffer and (B) pure 50 mM HEPES buffer (both 0.46 s^{-1}). A second series of experiments using a different batch of **1** provided r_1 values of $4.73\text{ mM}^{-1}\text{ s}^{-1}$ and $5.30\text{ mM}^{-1}\text{ s}^{-1}$ for the reduced and oxidized forms of the sensor; these are identical within error to those found for the above experiment.

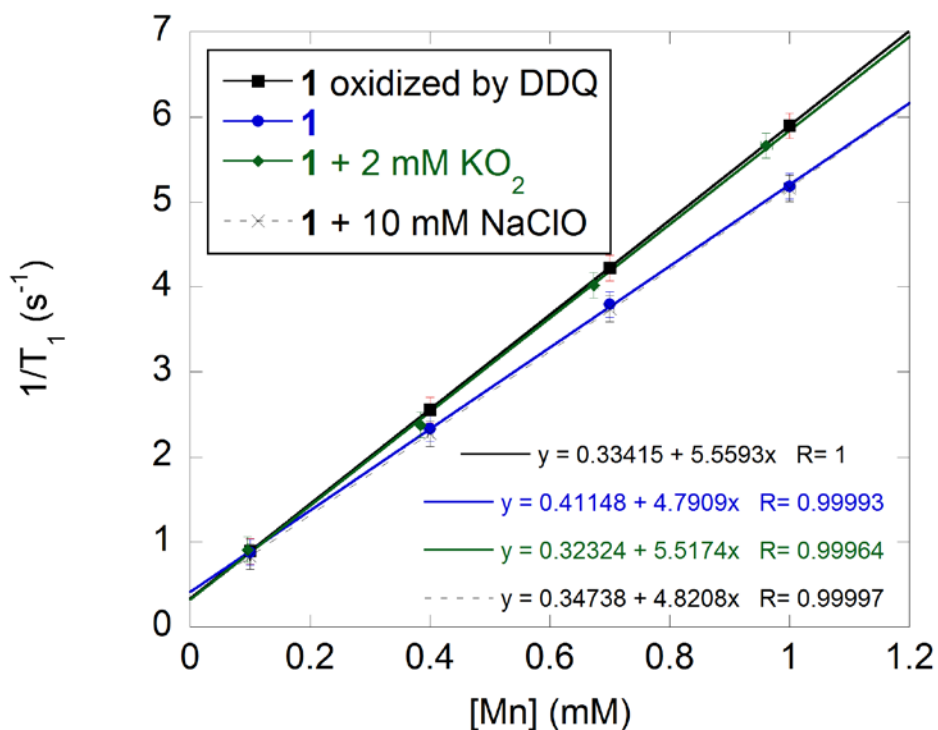


Figure 3A.17. Plots of $(1/T_1)$ versus Mn(II) concentration for **1** in the presence of various oxidants. All samples were run in 298 K aqueous solutions containing 50 mM HEPES buffered to pH 7.00, using a 3 T field provided by a clinical MRI scanner. The data were fit to the indicated linear equations; the y-intercepts were within error of $1/T_1$ measurements associated with two control samples that contained no Mn(II): (A) 10 mM H_2O_2 in 50 mM HEPES buffer and (B) pure 50 mM HEPES buffer (both $0.46 s^{-1}$). The oxidation of **1** by 2,3-dichloro-5,6-dicyano-1,4-benzoquinone (DDQ) occurred in CH_2Cl_2 . After the reaction occurred, the 2,3-dichloro-5,6-dicyanoquinol product was removed via filtration, the CH_2Cl_2 was removed, and the sample was dissolved in HEPES buffer for MRI analysis. The other oxidation reactions occurred entirely in HEPES buffer. The addition of KO_2 and DDQ resulted in enhanced relaxivity; the addition of $NaClO$, conversely, did not trigger a MRI response.

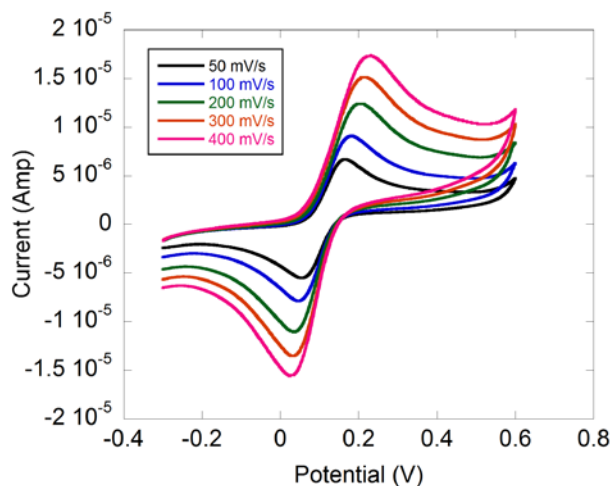


Figure 3A.18. Cyclic voltammetry of an aqueous solution containing 1.0 mM **1** and 0.10 M phosphate ($\text{NaH}_2\text{PO}_4/\text{Na}_2\text{HPO}_4$) buffered to pH 7.2. The starting and end potentials have been chosen to focus on the ligand-derived redox features. The measured $E_{1/2}$ and ΔE with the 100 mV/s scan rate were 115 mV vs. Ag/AgCl and 135 mV, respectively.

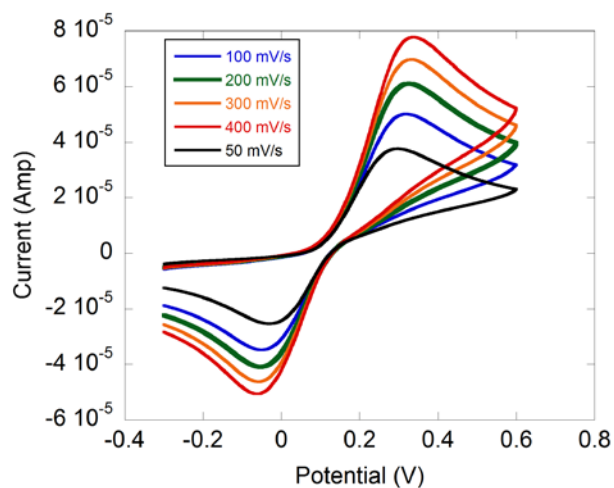


Figure 3A.19. Cyclic voltammetry of an aqueous solution containing 1.0 mM $\text{H}_2\text{qtp1}$, 1.0 mM $\text{Zn}(\text{ClO}_4)_2$, and 0.10 M phosphate ($\text{NaH}_2\text{PO}_4/\text{Na}_2\text{HPO}_4$) buffered to pH 7.2. The starting and end potentials have been chosen to focus on the ligand-derived redox features; no other redox features were observed outside of this range. The measured $E_{1/2}$ with the 100 mV/s scan rate was 135 mV vs. Ag/AgCl.

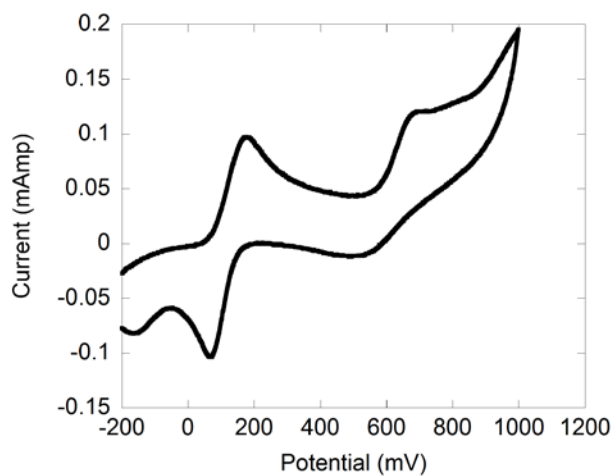


Figure 3A.20. Cyclic voltammetry of an aqueous solution containing 1.0 mM **1** and 0.10 M phosphate ($\text{NaH}_2\text{PO}_4/\text{Na}_2\text{HPO}_4$) buffered to pH 7.2. The scan rate was 100 mV/s. The measured E_{pc} for the metal oxidation was 680 mV vs. Ag/AgCl.

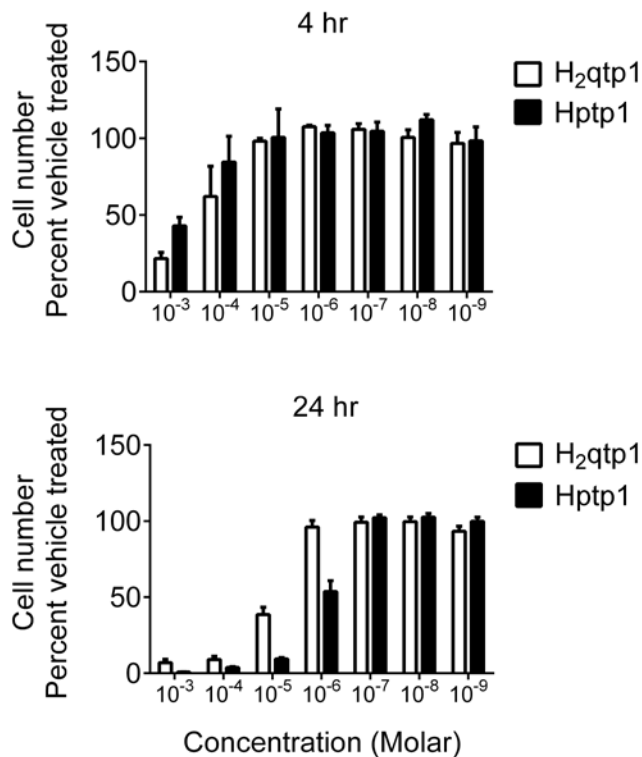


Figure 3A.21. Cytotoxic effects of **1** and **2** on H9c2 cells. The cells were treated with various dosages of **1** and **2** in DMEM for either 4 or 24 h in a cell culture incubator set to 37 °C. Cell number was determined using the CyQuant Cell Proliferation Assay. The data are expressed as a percentage of the cells exposed to the vehicle. Assays were performed in triplicate and repeated three times.

References

- (1) Dexter, D. T.; Carter, C. J.; Wells, F. R.; Javoy-Agid, F.; Agid, Y.; Lees, A.; Jenner, P.; Marsden, C. D. *J. Neurochem.* **1989**, *52*, 381-389.
- (2) Viappiani, S.; Schulz, R. *Am. J. Physiol. Heart Circ. Physiol.* **2006**, *290*, H2167-H2168.
- (3) Shishehbor, M. H.; Aviles, R. J.; Brennan, M. L.; Fu, X.; Goormastic, M.; Pearce, G. L.; Gokce, N.; Keaney, J. F., Jr.; Penn, M. S.; Sprecher, D. L.; Vita, J. A.; Hazen, S. L. *J. Am. Med. Assoc.* **2003**, *289*, 1675-1680.
- (4) Askenov, M. Y.; Askenova, M. V.; Butterfield, D. A.; Geddes, J. W.; Markesbery, W. R. *Neurosci.* **2001**, *103*, 373-383.
- (5) Lippert, A. R.; Van de Bittner, G. C.; Chang, C. J. *Acc. Chem. Res.* **2011**, *44*, 793-804.
- (6) Maeda, H.; Yamamoto, K.; Nomura, Y.; Kohno, I.; Hafsi, L.; Ueda, N.; Yoshida, S.; Fukuda, M.; Fukuyasu, Y.; Yamauchi, Y.; Itoh, N. *J. Am. Chem. Soc.* **2005**, *127*, 68-69.
- (7) Koide, Y.; Urano, Y.; Kenmoku, S.; Kojima, H.; Nagano, T. *J. Am. Chem. Soc.* **2007**, *129*, 10324-10325.
- (8) Soh, N. *Anal. Bioanal. Chem.* **2006**, *386*, 532-543.
- (9) Chen, X.; Tian, X.; Shin, I.; Yoon, J. *Chem. Soc. Rev.* **2011**, *40*, 4783-4804.
- (10) Caravan, P. *Acc. Chem. Res.* **2009**, *42*, 851-862.
- (11) Esqueda, A. C.; López, J. A.; Andreu-de-Riquer, G.; Alvarado-Monzón, J. C.; Ratnakar, J.; Lubag, A. J. M.; Sherry, A. D.; De León-Rodríguez, L. M. *J. Am. Chem. Soc.* **2009**, *131*, 11387-11391.
- (12) Major, J. L.; Parigi, G.; Luchinat, C.; Meade, T. J. *Proc. Natl. Acad. Sci., U. S. A.* **2007**, *104*, 13881-13886.
- (13) Chen, J. W.; Pham, W.; Weissleder, R.; Bogdanov, A., Jr. *Magn. Reson. Med.* **2004**, *52*,

- 1021-1028.
- (14) Raghunand, N.; Jagadish, B.; Trouard, T. P.; Galons, J.-P.; Gillies, R. J.; Mash, E. A. *Magn. Reson. Med.* **2006**, *55*, 1272-1280.
- (15) Ratnakar, S. J.; Viswanathan, S.; Kovacs, Z.; Jindal, A. K.; Green, K. N.; Sherry, A. D. *J. Am. Chem. Soc.* **2012**, *134*, 5798-5800.
- (16) Yu, M.; Beyers, R. J.; Gorden, J. D.; Cross, J. N.; Goldsmith, C. R. *Inorg. Chem.* **2012**, *51*, 9153-9155.
- (17) Loving, G. S.; Mukherjee, S.; Caravan, P. *J. Am. Chem. Soc.* **2013**, *135*, 4620-4623.
- (18) Viger, M. L.; Sankaranarayanan, J.; de Gracia Lux, C.; Chan, M.; Almutairi, A. *J. Am. Chem. Soc.* **2013**, *135*, 7847-7850.
- (19) Mialane, P.; Nivorojkine, A.; Pratviel, G.; Azéma, L.; Slany, M.; Godde, F.; Simaan, A.; Banse, F.; Kargar-Grisel, T.; Bouchoux, G.; Sainton, J.; Horner, O.; Guilhem, J.; Tchertanova, L.; Meunier, B.; Girerd, J.-J. *Inorg. Chem.* **1999**, *38*, 1085-1092.
- (20) Maurya, M. R.; Sikarwar, S. *J. Mol. Catal. A* **2007**, *263*, 175-185.
- (21) Owsik, I.; Kolarz, B. *J. Mol. Catal. A* **2002**, *178*, 63-71.
- (22) Smith, R. M.; Martell, A. E. *Critical Stability Constants*, 1st ed.; Plenum Press: New York, NY, 1975; Vol. 2, pp 249.
- (23) Chan, T.-L.; Mak, T. C. W. *J. Chem. Soc., Perkin Trans. 2* **1983**, *0*, 777-781.
- (24) Glick, M. D.; Dahl, L. F. *J. Organomet. Chem.* **1965**, *3*, 200-221.
- (25) Meyerson, M. L. *Spectrochim. Acta A* **1985**, *41*, 1263-1267.
- (26) Goldsmith, C. R.; Cole, A. P.; Stack, T. D. P. *J. Am. Chem. Soc.* **2005**, *127*, 9904-9912.
- (27) Hubin, T. J.; McCormick, J. M.; Alcock, N. W.; Busch, D. H. *Inorg. Chem.* **2001**, *40*, 435-444.

- (28) Caravan, P.; Ellison, J. J.; McMurry, T. J.; Lauffer, R. B. *Chem. Rev.* **1999**, *99*, 2293-2352.
- (29) Miller, A.-F. *Acc. Chem. Res.* **2008**, *41*, 501-510.
- (30) Batinic-Haberle, I.; Rajic, Z.; Tovmasyan, A.; Reboucas, J. S.; Ye, X.; Leong, K. W.; Dewhirst, M. W.; Vujaskovic, Z.; Benov, L.; Spasojevic, I. *Free Rad. Biol. Med.* **2011**, *51*, 1035-1053.
- (31) Aitken, J. B.; Shearer, E. L.; Giles, N. M.; Lai, B.; Vogt, S.; Reboucas, J. S.; Batinic-Haberle, I.; Lay, P. A.; Giles, G. I. *Inorg. Chem.* **2013**, *52*, 4121-4123.
- (32) Iranzo, O. *Bioorg. Chem.* **2011**, *39*, 73-87.
- (33) McCord, J. M.; Fridovich, I. *J. Biol. Chem.* **1969**, *244*, 6049-6055.
- (34) Kedare, S. B.; Singh, R. P. *J. Food Sci. Technol.* **2011**, *48*, 412-422.
- (35) Blois, M. S. *Nature* **1958**, *181*, 1199-1200.
- (36) Milaeva, E. R.; Shpakovsky, D. B.; Gracheva, Y. A.; Orlova, S. I.; Maduar, V. V.; Tarasevich, B. N.; Meleshonkova, N. N.; Dubova, L. G.; Shevtsova, E. F. *Dalton Trans.* **2013**, *42*, 6817-6828.

Chapter 4

Adding a Second Quinol to a Redox-Responsive MRI Contrast

Agent Improves its Relaxivity Response to H₂O^{*}

^{*} This Chapter is a revision of a submitted manuscript: Meng Yu, Ronald J. Beyers, Stephen, L. Ambrose, Zachary L. Whaley, T. Miller Bradford, John D. Gorden, Sanjun Fan, Russell C. Cattley, Dean D. Schwartz, and Christian R. Goldsmith.

4.1 Introduction

Reactive oxygen species (ROSs), including H_2O_2 , O_2^- , and hydroxyl radicals, are produced in small quantities during regular cellular metabolism. Of these, H_2O_2 is the least reactive, and most researchers believe that it accumulates at higher concentrations. ROSs are increasingly being identified as signaling agents and have been found to regulate several diverse physiological processes.¹⁻⁵ In spite of these beneficial functions, ROSs are perhaps better known for their deleterious effects. In a healthy organism, ROS levels are strictly regulated by enzymes such as catalase and superoxide dismutase. The over-accumulation of ROSs, also known as oxidative stress, has been implicated in many lethal and debilitating health conditions including cardiovascular disease, neurological disorders, and cancer.⁶⁻¹⁰

The exact roles of ROSs in these diverse health conditions remain poorly understood, and the desire to clarify these roles has motivated extensive efforts to develop imaging techniques capable of differentiating normal from aberrant redox activity in biological samples. Probes based on fluorescence and luminescence have been widely used in cell imaging; typically, these compounds react with ROSs to yield more highly emissive species.¹¹⁻¹⁷ Although these probes are highly sensitive towards the analytes and offer the ability to follow ROS generation and traffic at the cellular level, the short wavelength of light needed to excite the sensor and the tendency of probes to undergo autoxidation upon irradiation greatly limit their application in the non-invasive imaging of whole-body subjects.

Magnetic resonance imaging (MRI) is commonly used as a non-invasive diagnostic tool in medicine. In this technique, radio frequency (RF) photons are used to excite ^1H nuclei. Since the bulk of the body's ^1H nuclei are from water molecules, MRI differentiates tissues on the basis of their water content. Contrast agents are often added to accelerate the relaxation of the

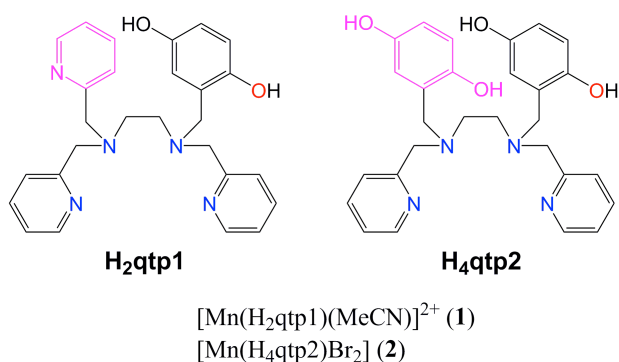
excited ^1H nuclei back to the ground state; this increases the amount of RF radiation that can be absorbed, thereby enhancing the contrast between water-rich and water-deficient regions. Either spin-lattice (T_1) or spin-spin (T_2) relaxation times can be monitored, but small molecule contrast agents generally induce larger changes in T_1 .¹⁸ The use of a responsive contrast agent, which exhibits a different relaxivity (r_1) upon exposure to an analyte, can allow researchers to visualize a biochemical process within a whole-body subject in concert with a clinical MRI scanner.^{19, 20}

Relatively few MRI contrast agents have been designed to probe redox activity.²¹⁻³³ Most redox-responsive contrast agent probes with mononuclear metal centers function via changes in the oxidation state of the metal, with the more paramagnetic species having the greater r_1 .^{21, 22} Caravan and co-workers, for instance, reported a manganese-containing contrast agent capable of switching between the +2 and +3 oxidation states through reactions with glutathione and H_2O_2 .²¹ Morrow's group recently reported an oxygen-sensitive cobalt complex that toggles between paramagnetic +2 and diamagnetic +3 oxidation states; it should be noted that this contrast agent operates through a PARACEST mechanism, rather than changes in T_1 .²³

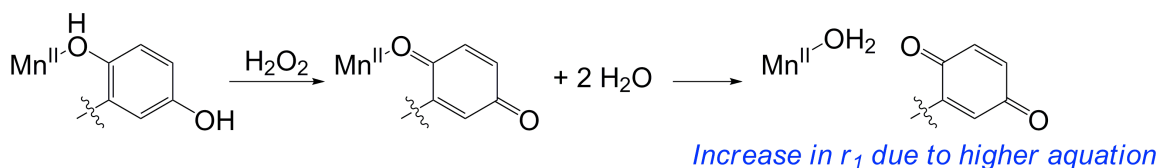
An alternative strategy is to couple the change in the MRI properties to a change in the oxidation state of the ligand, rather than the metal. The research groups of Sherry and Louie used this approach to develop lanthanide complexes that activate upon reduction by β -NADH.^{24, 25} Our own research team has developed mononuclear Mn(II) complexes with ligands containing *para*-methylphenol and quinol groups that react directly with H_2O_2 .^{26, 27} The sensor with the quinol ligand exhibits an increase in the r_1 value upon oxidation, which was the first instance of an oxidant-triggered enhancement in the T_1 contrast for a small molecule sensor.²⁷ Surface-

derivatized Gd₂O₃ nanoparticles were previously reported as turn-on sensors for H₂O₂ by the Almutairi group.²⁸

The quinol is an effective functional unit in [Mn(H₂qtp1)(MeCN)]²⁺ (**1**, Scheme 4.1) since it can be oxidized to a more weakly metal-binding *para*-quinone (Scheme 4.2). Water molecules can more readily displace quinones than quinols from the Mn(II), and the r_1 is believed to improve through an increase in the average aquation number (q).¹⁸ The Mn(II) serves as both the paramagnetic reporter and the catalyst for the oxidation of the quinol; after the reaction, the manganese remains in the +2 oxidation state. Reductants can reverse the ligand oxidation and regenerate the quinol. Although the stability in water is good and the response is selective for H₂O₂ over O₂, the modest relaxivity difference (0.8 mM⁻¹ s⁻¹) between the reduced and fully oxidized forms is just barely noticeable with a clinical MRI scanner.



Scheme 4.1 Ligand structure for complex **1** and **2**.



Scheme 4.2 Mechanism of MRI response to H₂O₂.

In the present work, we synthesized a second-generation MRI contrast agent [Mn(H₄qtp2)Br₂] (**2**) by installing a second quinol moiety in place of one of the pyridine rings

(Scheme 4.1). The presence of the second quinol subunit improves the response to H₂O₂ without severely compromising the stability of the complex in aerobic aqueous solutions. The relaxivity of **2** increases by 1.75 mM⁻¹ s⁻¹ after oxidation by H₂O₂; this represents an approximately three-fold improvement over the response exhibited by **1**.

4.2 Experimental Section

Materials

Except where stated otherwise, all chemicals were purchased from Sigma-Aldrich and used as received. 2,2-Diphenyl-1-picryl-hydrazyl hydrate (DPPH) was bought from EMD Millipore. Cambridge Isotopes supplied the deuterated acetonitrile (CD₃CN) and methanol (CD₃OD). Diethyl ether (ether) and methanol (MeOH) were purchased from Fisher. Methylene chloride (CH₂Cl₂) was acquired from Mallinckrodt Baker. The ligand precursor *N,N'*-bis(2-pyridinylmethyl)-1,2-ethanediamine (bispicen) was prepared as described previously.³⁴

Instrumentation

All ¹H and ¹³C NMR spectra were recorded on a 400 MHz AV Bruker NMR spectrometer; all reported resonance peak frequencies were referenced to internal standards. Electron paramagnetic resonance (EPR) spectra were collected using a Bruker EMX-6/1 X-band EPR spectrometer operated in the perpendicular mode and analyzed with the program EasySpin. Each EPR sample was run as a frozen solution in a quartz tube. High-resolution mass spectrometry (HR-MS) data were obtained at the Mass Spectrometer Center at Auburn University on a Bruker microflex LT MALDI-TOF mass spectrometer via direct probe analysis operated in the positive ion mode. Infrared spectroscopy (IR) data were obtained with a Shimadzu IR Prestige-21 FT-IR spectrophotometer. A Johnson Matthey magnetic susceptibility balance (model MK I#7967) was used to measure the magnetic properties of the Mn(II) complex

with H_4qtp2 ; the reported μ_{eff} value was the average of two independent measurements, each of which corresponded to a unique solid sample. Atlantic Microlabs (Norcross, GA) performed the elemental analyses (C, H, N). All samples submitted for elemental analysis were dried under vacuum prior to their shipment. All cyclic voltammetry (CV) was performed under N_2 at 294 K using an Epsilon electrochemistry workstation (Bioanalytical System, Inc.), a gold working electrode, a platinum wire auxiliary electrode, and a silver/silver(I) chloride reference electrode.

X-Ray Crystallography

Crystals of $[Mn(H_4qtp2)Br_2]$ and its fully oxidized analog $[Mn(qtp2)Br_2]$ were mounted in Paratone oil on a glass fiber and aligned on a Bruker SMART APEX CCD X-ray diffractometer. Intensity measurements were performed using graphite monochromated $Mo\ K\alpha$ radiation ($\lambda = 0.71073\ \text{\AA}$) from a sealed tube and monocapillary collimator. SMART (v 5.624) was used to determine the preliminary cell constants and regulate the data acquisition. The intensities of reflections of a sphere were collected through the compilation of three sets of exposures (frames). Each set had a different φ angle for the crystal, with each exposure spanning a range of 0.3° in ω . A total of 1800 frames were collected with exposure times of 40 s per frame. The data were corrected for Lorentz and polarization effects. Structures were solved using direct methods and expanded using Fourier techniques. All non-hydrogen atoms were refined anisotropically.

Hydrogen atoms were included at idealized positions $0.95\ \text{\AA}$ from their parent atoms prior to the final refinement. Further details regarding the data acquisition and analysis are included in Tables 4.1 and 4.2.

Measurement of Binding Affinity of H_4qtp2 for Mn(II)

The $\log(K)$ for the interaction between H_4qtp2 and $Mn(II)$ was measured via a competitive binding assay between N,N,N',N' -tetrakis(2-pyridylmethyl)ethylenediamine (TPEN) and H_4qtp2 . Various amounts of TPEN were added to a solution of $[Mn(H_4qtp2)Br_2]$ in D_2O . The resultant mixtures were analyzed by 1H NMR. The ratio of uncoordinated TPEN to uncoordinated H_4qtp2 was used to measure an equilibrium constant for the reaction:



This equilibrium constant was then combined with the known $\log(K)$ of 10.3 for TPEN³⁵ to obtain a $\log(K)$ of 10.2 (± 0.1) for H_4qtp2 .

Magnetic Resonance Imaging (MRI)

All MRI data were collected at the Auburn University MRI Research Center (Auburn, AL) on a Siemens Verio open-bore 3-T MRI clinical scanner. Samples were imaged using a 15-channel knee coil, which allowed the simultaneous imaging of 12-26 samples. An inversion recovery (IR) sequence was used that featured a non-selective adiabatic inversion pulse followed by a slice-selective gradient recalled echo (GRE) readout after a delay period corresponding to the inversion time (TI).^{36, 37} The GRE was a saturation readout, such that only one line of k-space was acquired per repetition time (TR). This method was selected to maximize both the signal strength and the accuracy of the T_1 estimates. Specific imaging parameters were as follows: TR was set to 4 s, TI was varied from 4.8 to 2500 ms over 37 steps, the echo time (TE) was set to 3.6 ms, the flip angle equaled 90° , averages = 1, slice thickness = 5 mm, field of view = 140×140 mm, matrix = 128×128 , resulting in a pixel size of $1.1 \times 1.1 \times 5.0$ mm. All samples were run in 50 mM solutions of HEPES in water that were buffered to pH 7.0 and kept at $22^\circ C$. The manganese content was systematically varied from 0.10 to 1.00 mM. The inverses of the T_1 values were plotted versus the concentration of $Mn(II)$ to obtain r_1 values. All reported r_1 values

are derived from the results of two separate series of experiments, each of which used a different batch of $[\text{Mn}(\text{H}_4\text{qtp2})\text{Br}_2]$.

MRI Data Analysis

Image analysis was performed using custom Matlab programs (Mathworks, Natick, MA). The initial $\text{TI} = 4.8$ ms image served as a baseline to determine the circular region of interest (ROI) boundaries for each sample; from these, the mean pixel magnitudes for each ROI were calculated. For each of the 36 subsequent TI images, the same ROI boundaries were applied and the mean pixel magnitude calculations were repeated. This gave consistent ROI spatial definitions and a corresponding time course of magnitudes for each of the samples over all the TI time points. Each sample's complex phase was used to correct the magnitude polarity to produce a complete exponential T_1 inversion recovery curve. The Nelder-Mead simplex algorithm³⁸ was applied to each sample's exponential curve to estimate its corresponding T_1 value.

Analysis of Anti-Oxidant Behavior

Superoxide was produced from a reaction between xanthine and xanthine oxidase. Subsequent reaction between O_2^- and lucigenin provides a luminescent response that can be used to quantitatively measure the ability of an anti-oxidant to degrade O_2^- .^{39, 40} Superoxide degradation assays were performed with 1 mL aqueous solutions containing tris (50 mM, pH 8.0), hypoxanthine (50 μM), xanthine oxidase (0.005 U/ml, Calbiochem) and dark adapted lucigenin (5 μM) in the absence or presence of **2** (0.1 nM - 10 μM). Reactions were carried out at room temperature and were initiated by the addition of xanthine oxidase to the hypoxanthine-containing solution. The copper/zinc superoxide dismutase isolated from bovine erythrocytes (0.001-100 U/ml, Calbiochem) was used as a positive control. Luminescence was measured using a TD-20/20 (Turner Designs) luminometer and expressed as relative light units (RLU).

Luminescence was measured for four 10 s integrations after an initial delay of 3 s. The four RLU values were averaged, and each concentration was expressed as a percent of that produced in the presence of vehicle. Each assay data point was performed in duplicate and each assay was repeated three times.

The DPPH assay provides an alternative gauge of a compound's anti-oxidant properties by assessing its ability to donate hydrogen atoms.⁴¹⁻⁴³ Aqueous solutions of either **2** or ascorbic acid were added to a solution of 0.10 mM DPPH in MeOH, such that the final reaction volume was 0.2 mL. Samples were incubated in the dark for 30 min at room temperature. Spectrophotometric measurements were subsequently performed at 517 nm using a Molecular Devices Spectramax Plus. This wavelength corresponds to the λ_{max} of the reduced product, 2,2-diphenyl-1-picryl-hydrazine. Measurements within each experiment were performed in triplicate, and the entire series were repeated twice.

Cytotoxicity Assay

The toxicity of the probe was tested with H9c2 cells. H9c2 cells were obtained from the American Tissue Type Collection (Manassas, VA, USA) and grown at 37 °C with 95% humidity and 5% CO₂. Cells were grown in Dulbecco's modified eagles medium (DMEM) supplemented with 10% fetal bovine serum. All experiments were performed at 70-80% confluence. To determine the cytotoxicity of **2**, H9c2 cells were exposed to increasing concentrations of the Mn(II) complex (0.1 - 1000 μM) or its vehicle in DMEM for 4 or 24 h. Cell number was assessed using the CyQUANT Cell Proliferation Assay Kit (Life Technologies Corporation, Carlsbad, CA) per manufacturer's instructions. Cell number was expressed as percentage of the vehicle-treated cells.

Biological Imaging

Male Sprague-Dawley rats (approximately 220 g body weight, Harlan Laboratories, IN) were housed in filter-top polycarbonate cages with ad libitum food (pelleted chow) and water, and acclimated for 4-7 days prior to treatment. Rats were administered either doxorubicin (Sagent Pharmaceuticals, Schaumburg, IL) at 10 mg/kg in 1.5 mL 0.9% saline vehicle or vehicle alone by intraperitoneal injection. Approximately 72 h later, each rat was anesthetized by inhaled isoflurane (in oxygen, 4% for induction and 1.0-2.5% for maintenance) for whole body perfusion as follows. Each rat was monitored by electrocardiography and a jugular catheter was placed. Via the catheter, each rat received contrast agent **2** at 10 mg/kg, dissolved in 250 microliters of 50% dimethylsulfoxide: 50% phosphate buffered saline (PBS, pH 7.4, 137 mM NaCl, 2.7 mM KCl, 12 mM phosphate buffer) and infused over 10-12 minutes. Following infusion, the rats were maintained under anesthesia for 20 min, then terminally perfused via the jugular catheter with approximately 15 mL of ice cold PBS over approximately 30 s, while simultaneously being exsanguinated by transection of the abdominal aorta. Hearts were then removed, placed into ice-cold PBS, and imaged by MRI.

Multiple *ex vivo* tissue samples and four reference phantoms with known T_1 and T_2 values were simultaneously imaged in the same field of view.

T_1 -weighted (T1w) imaging was performed with a spin-echo (SE) sequence and an array of parameter settings. This allowed us to detect visible differences in T_1 contrast between the samples and the reference phantoms. The T1w SE parameters included 12 repetition times (TR): 50, 75, 100, 150, 200, 300, 400, 600, 800, 1000, 1200, and 1500 ms. The other parameters were held constant: echo time (TE) = 8.5 ms; field of view = 48 × 30 mm; matrix = 144 × 90 pixels; slice thickness = 2 mm; in-plane pixel size = 0.33 × 0.33 mm; bandwidth = 347 Hz/pixel; total measurement time = 30 s to 4 min.

T_2 -weighted (T2w) imaging was also performed using a SE sequence and an array of parameter settings in order to assess whether there were visible differences in the T_2 contrast between the samples and reference phantoms. TR = 1000 ms; TE = 20, 30, 40, 60, 100, 150, or 200 ms; field of view = 48×30 mm; matrix = 144×90 pixels; slice thickness = 2 mm; in-plane pixel size = 0.33×0.33 mm; bandwidth = 347 Hz/pixel; total measurement time = 4 min.

T_1 -mapping was done using an inversion recovery Look-Locker sequence. TR = 2000 ms; 15 inversion times (TI) were used spaced at 100 ms increments from 100 to 1500 ms per TR; field of view = 48×30 mm; matrix = 144×90 pixels; slice thickness = 2 mm; in-plane pixel size = 0.33×0.33 mm; flip angle = 5° ; bandwidth = 347 Hz/pixel; segmentation = 3 k-space lines per TR; averages = 16; total measurement time = 20 min.

T_2 -mapping was performed with a T_2 -Preparation sequence. TR = 2000 ms; four T_2 prep TE = 8.5, 15, 30, or 45 ms; field of view = 48×30 mm; matrix = 144×90 pixels; slice thickness = 2 mm; in-plane pixel size = 0.33×0.33 mm; flip angle = 30° ; bandwidth = 347 Hz/pixel; segmentation = 2 k-space lines per TR; averages = 2; total measurement time = 13 min.

All T_1 and T_2 maps were generated off-line with in-house custom Matlab programs. Temporal T_1 -map image pixel magnitudes from the 15 TI times were curve-fitted to a longitudinal T_1 recovery equation to estimate the per-pixel T_1 time constant. The multiplicative inverse of the T_1 estimate provided the R_1 estimate. Temporal T_2 -map image pixel magnitudes from the 4 TE times were curve-fitted to a transverse T_2 relaxation equation to estimate the per-pixel T_2 time constant. The multiplicative inverse of the T_2 estimate provided the R_2 estimate. In both the T_1 and T_2 maps, regional groupings of pixels were then analyzed for statistical mean and variation as required.

Syntheses

***N*-(2,5-Dihydroxybenzyl)-*N,N'*-bis(2-pyridinylmethyl)-1,2-ethanediamine.**

2,5-Dihydroxybenzaldehyde (552 mg, 4.00 mmol) and bispicen (1.03 g, 4.25 mmol) were dissolved in 20 mL of ether. The resultant mixture was stirred for 4 h, during which time a solid deposited. The precipitate was collected and washed with a mixture of MeOH/ether (1:9). The isolated and washed aminal (900 mg, 2.48 mmol) was dried and redissolved in 30 mL of MeOH. Trifluoroacetic acid (750 mg, 6.58 mmol) was added to the MeOH solution at 0 °C, followed by sodium cyanoborohydride (220 mg, 3.50 mmol). The mixture was stirred at RT for 24 h, at which point the solvent was removed to yield the crude product. The crude was purified by repeated precipitation from MeOH/ether to yield the product as a white solid (568 mg, 63% yield). Typical yields range from 60-70%. ¹H NMR (400 MHz, CD₃OD, 293 K): δ 8.54 (d, J = 4.5 Hz, 1H), 8.44 (d, J = 4.5Hz, 1H), 7.80 (m, 2H), 7.38 (m, 4H), 6.58 (m, 3H), 4.25 (s, 2H), 3.92 (s, 2H), 3.71 (s, 2H), 3.31 (m, 4H). ¹³C NMR (100 MHz, CD₃OD, 293 K): δ 158.42, 151.51, 149.87, 149.22, 148.70, 148.29, 137.48, 137.32, 124.04, 123.55, 122.48, 117.43, 115.94, 115.09, 57.76, 54.23, 49.58, 49.27, 44.64. MS (ESI): Calcd for MH⁺, 365.1978; Found, 365.2156.

***N,N'*-Bis(2,5-dihydroxybenzyl)-*N,N'*-bis(2-pyridinylmethyl)-1,2-ethanediamine (H₄qtp2).**

N-(2,5-Dihydroxybenzyl)-*N,N'*-bis(2-pyridinylmethyl)-1,2-ethanediamine (939 mg, 2.57 mmol) and 2,5-dihydroxybenzaldehyde (354 mg, 2.57 mmol) were combined in 60 mL of MeOH. The mixture was cooled to 0 °C with an ice bath. Subsequently, acetic acid (308 mg, 5.14 mmol) was added to the solution, which then stirred for 30 min. After this period, sodium cyanoborohydride (161 mg, 2.57 mmol) was added, and the resultant solution was stirred for an additional 24 h. Second portions of 2,5-dihydroxybenzaldehyde (354 mg, 2.57 mmol), acetic acid (308 mg, 5.14 mmol), and sodium cyanoborohydride (161 mg, 2.57 mmol) were added and

allowed react for another 16 h. The solvent was removed under reduced pressure, and the residue was purified by silica gel chromatography (15:1 EtOAc/MeOH eluent, product $R_f = 0.3$) to yield the ligand as a white powder (800 mg, 64% yield). Typical yields range from 45-65%. ^1H NMR (400 MHz, CD_3OD , 293 K): δ 8.46 (qd, $J = 5.2$ Hz, 1.6 Hz, 0.8 Hz, 2H), 7.75 (dt, $J = 9.6$ Hz, 2.0 Hz, 2H), 7.31 (m, 4 H), 6.58 (d, $J = 1.6$ Hz, 4H), 6.55 (m, 2H), 3.81 (s, 4H), 3.68 (s, 4H), 2.87 (s, 4H). ^{13}C NMR (100 MHz, CD_3CN , 293 K): δ 150.08, 149.36, 148.97, 137.07, 123.56, 122.59, 117.14, 116.47, 115.47, 58.27, 56.15, 49.82. MS (ESI): Calcd for MH^+ , 487.2346; Found, 487.2277.

***cis*-Dibromo(*N,N'*-bis(2,5-dihydroxybenzyl)-*N,N'*-bis(2-pyridinylmethyl)-1,2-ethane diamine)manganese(II) ($[\text{Mn}(\text{H}_4\text{qtp2})\text{Br}_2]$, 2).**

The $\text{H}_4\text{qtp2}$ ligand (500 mg, 1.03 mmol) and MnBr_2 (221 mg, 1.03 mmol) were dissolved in 5 mL of MeCN in a dry and anaerobic glovebox. The solution was allowed to stir at 60°C for 16 h during which time, a white precipitate deposited. The solution was filtered, and the filtrate was washed with MeCN to yield the product as a white powder (550 mg, 71% yield). Typical yields range from 70-85%. Crystals suitable for single crystal X-ray diffraction were grown by slow evaporation from a saturated solution of the crude in MeOH. MS (ESI): Calcd for $[\text{Mn}(\text{L-H})]^+$, 540.1569; Found, 540.1564. Solid-state magnetic susceptibility (294 K): $\mu_{\text{eff}} = 5.6 \mu_{\text{B}}$. Optical spectroscopy (MeOH): 302 nm ($5420 \text{ M}^{-1} \text{ cm}^{-1}$). IR (KBr, cm^{-1}): 3405 (s), 1604 (m), 1511 (s), 1446 (s), 1358 (w), 1341 (w), 1310 (w), 1210 (m), 1191 (s), 1156 (w), 1066 (w), 1049 (w), 1016 (w), 948 (w), 934 (w), 810 (m), 754 (m). Elemental Analysis (powder): Calcd for $\text{C}_{28}\text{H}_{30}\text{N}_4\text{MnO}_4\text{Br}_2 \cdot \text{CH}_3\text{CN}$: C, 48.54%; H, 4.48%; N, 9.43%; Found: C, 48.43 %; H, 4.58%; N, 9.72%.

***cis*-Dibromo(*N,N'*-bis(2,5-benzoquinone)-*N,N'*-bis(2-pyridinylmethyl)-1,2-ethanediamine)manganese(II) ([Mn(qtp2)Br₂], 3).**

Complex **2** (60 mg, 0.080 mmol) was dissolved in 1 mL of CH₂Cl₂ under N₂. 2,3-Dichloro-5,6-dicyano-*p*-benzoquinone (DDQ, 37 mg, 0.16 mmol) was dissolved in 5 mL of CH₂Cl₂. The resultant solution was added to **2** dropwise. The mixture was allowed to stir overnight, at which point it was filtered through the Celite. Slow evaporation of the solvent from the filtrate deposited red crystals that were suitable for X-ray diffraction. These were collected and washed with cold CH₂Cl₂ to yield 9.8 mg of product (16%). Typical yields range from 10-15%. Optical spectroscopy (MeOH): 249 nm (4140 M⁻¹ cm⁻¹). IR (KBr, cm⁻¹): 3434 (s), 3234 (w), 2963 (m), 2925 (w), 2855 (w), 1657 (C=O, s), 1602 (m), 1443 (m), 1262 (m), 1102 (m), 1050 (m), 1015 (m), 810 (m). Elemental Analysis: Calcd for C₂₈H₂₆N₄MnO₄Br₂•0.5H₂O: C, 47.62%; H, 3.85%; N, 7.93%; Found: C, 47.70 %; H, 3.97%; N, 7.84%.

4.3 Results

Synthesis

The H₄qtp2 ligand can be synthesized from the readily available *N,N'*-bis(2-pyridinylmethyl)-1,2-ethanediamine (bispicen) in three steps. The synthesis of H₄qtp2 is more challenging than that of the closely related H₂qtp1. The installation of the second quinol requires much more effort, and obtaining high yields of pure H₄qtp2 required the addition of the reagents in two portions and a 40 h reaction time. The product is also hygroscopic and degrades under basic conditions (pH > 10). An alternate route in which the two quinol groups were added to 1,2-ethanediamine before the picolyl arms was explored, but it presented drawbacks similar to those for the route proceeding through bispicen in that adding the fourth arm of the ligand required forcing conditions. Further, the quinols needed to be protected before the installation of the

picolyl subunits; this and the subsequent deprotection add two synthetic steps. Although H₄qtp2 was successfully prepared through this route, the alternative synthesis requires much more time and yields less of the product.

The H₄qtp2 ligand appears to bind to Mn(II) readily, but we were unable to obtain a crystalline product from reactions between H₄qtp2 and either Mn(OTf)₂ or Mn(ClO₄)₂. Consequently, MnBr₂ was selected as the salt for the H₄qtp2 complex for two reasons. First, the solubility of this salt in MeCN facilitated the product's isolation and purification. Second, bromide does not bind avidly to Mn(II),⁴⁴ and we anticipated that this anion would be readily displaced by O-donors, such as quinols and water molecules, upon solvation. The complex [Mn(H₄qtp2)Br₂] (**2**) was prepared in moderately high yield by mixing the ligand with MnBr₂ in 60 °C MeCN. Upon standing, complex **2** precipitates from the reaction mixture.

The Mn(II) complex with the fully oxidized ligand (qtp2) was prepared by oxidizing **2** with 2,3-dichloro-5,6-dicyano-*p*-benzoquinone (DDQ) in CH₂Cl₂. This oxidant was previously noted for its ability to cleanly and fully oxidize the quinol subunit in the related **1**.²⁷ Crystals of [Mn(qtp2)Br₂] (**3**) can be obtained after approximately 20 h, albeit in relatively low yield. Regrettably, the solubility of crystalline **3** is poor in H₂O, MeCN, and MeOH; this and the poor yield limit our ability to both characterize the complex and use it as a standard for reactions involving **2** and H₂O₂.

Structural Characterization

Needle-shaped crystals of **2** were grown from saturated solutions of the complex in MeOH via slow evaporation of the solvent (Table 4.1). The Mn(II) center is six-coordinate, with the two bromides bound in a *cis* fashion and the four nitrogen donors provided by the H₄qtp2

ligand binding in a *cis-α* conformation which places the two pyridine groups *trans* to each other (Figure 4.1). Neither quinol binds directly to the Mn(II) in the crystal. The Mn-N and Mn-Br bond distances measured for **2** are typical for a hexacoordinate high-spin Mn(II) complex (Table 4.2).⁴⁵ The oxidation number and spin-state assignments derived from the metrical parameters are corroborated by solid-state magnetic susceptibility measurements ($\mu_{\text{eff}} = 5.6 \mu_{\text{B}}$). The Mn-N bonds to the pyridine rings are shorter than those to the tertiary amines; both pairs of bond distances are similar to those measured for other MnN_4X_2 cores with amine and pyridine N-donors.⁴⁶ The C-O bond distances average 1.37 Å, indicating that the quinols remain fully protonated.^{27, 47}

The product of DDQ oxidation, **3**, was also crystallized and structurally characterized (Figure 4.2). The metal center remains hexacoordinate and retains the same N_4Br_2 coordination sphere upon oxidation. The structure confirms that both quinols have been oxidized to *para*-quinones, as evidenced by the shorter C-O bond lengths (Table 4.2). The C-O bond distances average 1.23 Å. Upon oxidation, the bonds between the Mn(II) and the amine N atoms lengthen slightly while those between the Mn(II) and the Br atoms slightly contract. Although the crystals are colored, the oxidation state of the manganese remains +2, as best structurally evidenced by the Mn-N and Mn-Br bond distances.⁴⁵ None of the metal-ligand bonds are significantly elongated or shortened. This absence of Jahn-Teller distortions would be inconsistent with a high-spin Mn(III) center.

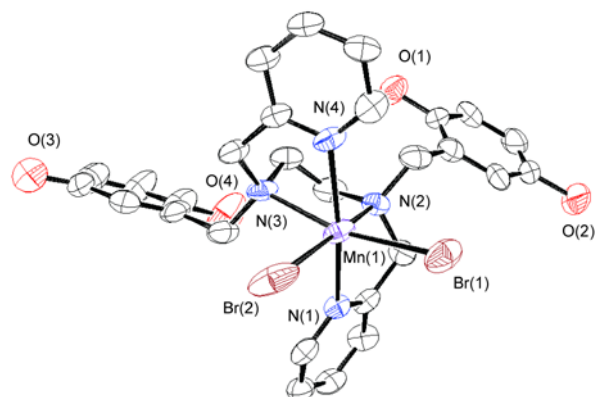


Figure 4.1. Structure of $[\text{Mn}(\text{H}_4\text{qtp}2)\text{Br}_2]$ (**2**). All hydrogen atoms and solvent molecules are omitted for clarity. All thermal ellipsoids are drawn at 50% probability.

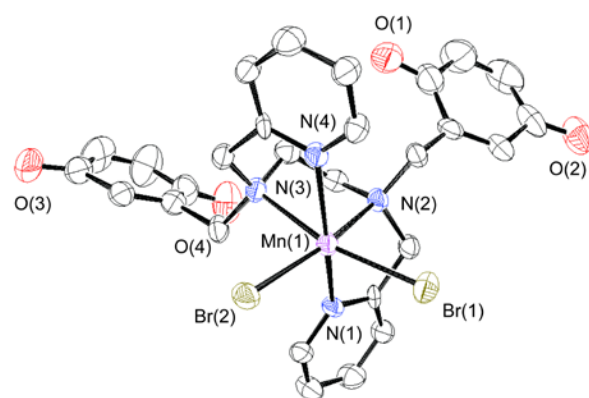


Figure 4.2. Structure of $[\text{Mn}(\text{qtp}2)\text{Br}_2]$ (**3**). All hydrogen atoms and solvent molecules are omitted for clarity. All thermal ellipsoids are drawn at 50% probability. The atoms have been relabeled from those in the CIF file in order to facilitate comparison to the structure of **2**.

Table 4.1. Selected crystallographic data for **2** and **3**.

Parameter	[Mn(H ₄ qtp2)Br ₂]•MeCN•H ₂ O (2)	[Mn(qtp2)(Br) ₂] (3)
Formula	C ₃₀ H ₃₃ Br ₂ MnN ₅ O ₅	C ₂₈ H ₂₆ Br ₂ MnN ₄ O ₈
MW	758.35	761.27
Crystal system	Monoclinic	Cubic
Space group	<i>P</i> _{21/n}	<i>Ia</i> 3 <i>d</i>
a (Å)	9.6411(2)	34.991(2)
b (Å)	21.9027(6)	34.991(2)
c (Å)	15.3507(4)	34.991(2)
α (deg)	90	90
β (deg)	99.881(1)	90
γ (deg)	90	90
V (Å ³)	3193.46(14)	42842(9)
Z	4	48
Cryst color	Light orange	Light red
T (K)	180	180
Reflns collected	31999	38465
Unique reflns	3031	1350
R1 (F, I > 2σ(I))	0.0566	0.0578
wR2 (F ² , all)	0.1104	0.2042

$$R1 = \sum | |F_o| - |F_c| | / \sum |F_o| ; wR2 = [\sum w(F_o^2 - F_c^2)^2 / \sum w(F_o^2)^2]^{1/2}.$$

Table 4.2. Selected bond lengths (Å) for complexes **2** and **3**. N(1) and N(4) correspond to pyridine nitrogens; N(2) and N(3) correspond to amine nitrogens. The atoms in **3** have been relabeled in order to facilitate comparison to those in the structure of **2**.

Complex	2	3
Mn-N(1)	2.241(5)	2.252(8)
Mn-N(2)	2.338(6)	2.395(8)
Mn-N(3)	2.346(6)	2.395(8)
Mn-N(4)	2.272(5)	2.252(8)
Mn-Br(1)	2.6244(14)	2.5971(19)
Mn-Br(2)	2.6134(15)	2.5971(19)
O(1)-C(13)	1.363(8)	1.226(15)
O(2)-C(10)	1.383(10)	1.242(16)
O(3)-C(22)	1.395(11)	1.242(16)
O(4)-C(19)	1.334(10)	1.226(15)

Spectroscopic Characterization

Complex **2** displays a moderately intense UV/vis absorbance band at 302 nm. This feature can be assigned to an electronic excitation within the quinol subunit.⁴⁸ As expected, the oxidized product **3** lacks this UV/vis band. Optical spectroscopy therefore provides a means to readily monitor the oxidation state of the ligand.

The oxidation state of the ligand can also be assessed by IR spectroscopy. The C=O stretches associated with the *para*-quinones are anticipated to appear between 1600 and 1800 cm⁻¹. The IR spectrum of **2** has a band at 1605 cm⁻¹, which has a frequency and intensity typical of a C-N stretch for a pyridine bound to a divalent metal,^{49, 50} but otherwise lacks features in this range. The IR spectrum of **3**, conversely, has a strong band at 1657 cm⁻¹, consistent with the presence of C=O bonds.

Electrochemistry

Complex **2** was studied by cyclic voltammetry (CV) in water containing 50 mM phosphate to buffer the solution to pH 7.2. A redox feature with $E_{1/2}$ of 60 mV vs. Ag/AgCl (295 mV vs. NHE) is observed. A similar redox process is found for both **1** and a Zn(II)-H₂qtp1 complex, leading us to assign the 60 mV redox event to the oxidation of the ligand, rather than the manganese.²⁷ The separation between the anodic and cathodic peaks, ΔE , for this feature is 230 mV, which is much larger than its analog in the CV of **1** (75 mV) and is consistent with a nearly irreversible process. A second and entirely irreversible redox event occurs at 725 mV (960 mV vs NHE). We have tentatively assigned this feature to the oxidation of Mn(II) to Mn(III).

Stability of [Mn(H₄qtp2)Br₂] to Water and Air

The stability of the H₄qtp2-Mn(II) adduct in water was confirmed by NMR. When complex **2** is dissolved in D₂O, ¹H NMR spectroscopy detects no resonances aside from that

corresponding to the solvent. The ^1H NMR data are therefore inconsistent with the presence of either the free $\text{H}_4\text{qtp2}$ ligand or potential decomposition products. The formation constant of the $\text{Mn-H}_4\text{qtp2}$ adduct was estimated through a competitive binding assay with N,N,N',N' -tetrakis(2-pyridylmethyl)-1,2-ethanediamine (tpen). The tpen and $\text{H}_2\text{qtp1}$ ligands were previously found to have similar binding affinities for Mn(II) .²⁷ The $\log(K)$ for $\text{H}_4\text{qtp2}$ was determined to be 10.2, which is slightly less than the 10.7 value measured for the interaction between Mn(II) and $\text{H}_2\text{qtp1}$.

The stability of **2** to air and adventitious metal ions was monitored primarily by UV/vis spectroscopy. In MeOH, the 302 nm feature corresponding to the quinol groups decreases in intensity by about 10% over 12 h, which demonstrates that **2** is sufficiently air stable for MRI studies. Complex **2** is, however, susceptible to metal exchange. When equimolar amounts of **2** and $\text{Fe}(\text{ClO}_4)_2$ are mixed in MeCN, 80% of the Mn(II) is replaced by Fe(II) by 3 h. Experiments monitored by NMR suggest that Zn(II) can also readily displace the Mn(II) from **2** (*via infra*).

Reactivity with H_2O_2

Although complex **2** is stable to prolonged exposure to air and moisture, it reacts with H_2O_2 to yield a mixture of Mn(II) species in which either zero, one, or two of the quinol groups have been oxidized to *para*-quinones.

EPR spectroscopy confirms that the manganese in the oxidized samples remains in the +2 oxidation state. The EPR spectrum of a 1.0 mM solution of **2** in MeOH is highly similar to that corresponding to a 1.0 mM sample of **2** that was allowed to react with 10 mM of H_2O_2 for 30 min (Figure 4.3). Both EPR spectra show a major feature at $g = 2.00$ that is split six-fold by the $I = 5/2$ manganese nucleus. A minor feature at 1000 gauss is present in both samples as well. For the non-oxidized sample, this feature likewise exhibits hyperfine splitting; the oxidized sample,

conversely, lacks this detail. The two EPR spectra overlap almost perfectly, suggesting that they have nearly equal concentrations of Mn(II).

The oxidation by H_2O_2 was also monitored spectrophotometrically (Figure 4.4). The reaction requires 1 h to equilibrate, as evidenced by changes in the features at 250 nm and 302 nm. The disappearance of the 302 nm band is consistent with the quinol groups being oxidized to *para*-quinones. The 250 nm peak, conversely, intensifies as the oxidation proceeds. When the reaction is monitored beyond 1 h, a new absorption band starts to develop at 420 nm; the wavelength of this band is reminiscent of those associated with previously prepared mononuclear Mn(III) complexes with N- and O-donor ligands.^{51, 52} The aforementioned changes in the 250 nm and 302 nm features can also be triggered by the addition of DDQ. The changes in the spectra are consistent with an induction period, in that little change occurs until approximately 10 min after the reagents are mixed. Excesses of O_2^- or ClO^- result in the decomposition of the ligand and do not appear to cleanly generate the species with either one or two *para*-quinones.

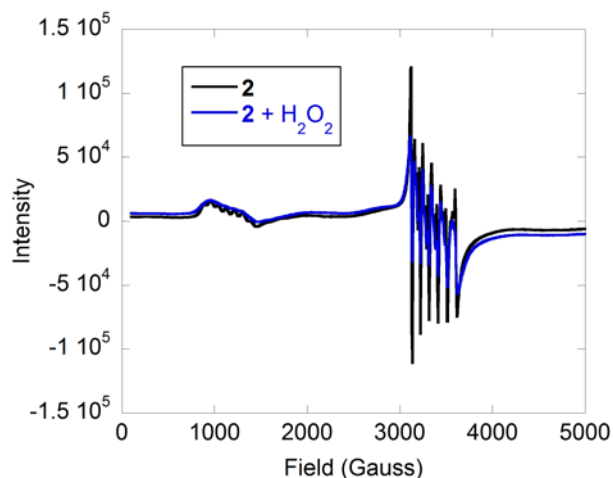


Figure 4.3. X-band EPR spectra of 1.0 mM solutions of **2** in MeOH in the absence and presence of 10 mM H_2O_2 . The reaction between **2** and H_2O_2 proceeded for 30 min before the sample was

frozen and analyzed. The data were acquired at 77 K. For both spectra: $g_{eff} = 2.00$, $A = 103$ Gauss.

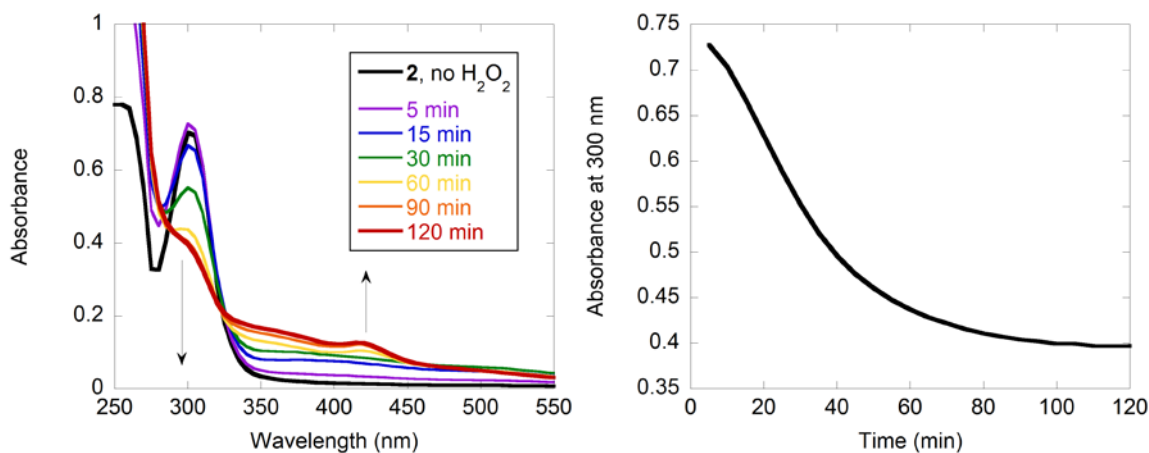


Figure 4.4. UV/vis spectra corresponding to the 298 K reaction between a 0.10 mM **2** and 10 mM H₂O₂ in MeOH. The reaction was tracked for 2 h. The absorbance initially increases slightly due to the unreacted H₂O₂. The right panel shows the change in the absorbance at 300 nm over this time.

The reaction between **2** and various amounts of H₂O₂ in MeOH was also analyzed by mass spectrometry (MS). Methanolic solutions of **2** changed from pale blue to light brown within a few minutes after adding H₂O₂. The MS shows new m/z peaks at 485.20 and 483.19 corresponding to the oxidation of one and two of the quinols to *para*-quinones. With 4 equiv. of H₂O₂, the oxidation is slower, and more of the singly oxidized ligand is observed. The reaction appears to finish within 1 h. With 8 and 16 equiv. of terminal oxidant, the reactivity occurs more quickly and results in more of the doubly oxidized ligand. These reactions finish within 30 min. Additional m/z peaks are found when the reaction is allowed to proceed for 12 h. These peaks have not been assigned to discrete species, and they likely result from subsequent oxidation of the ligand and manganese.

The IR of the solid isolated from reactions between **2** and 4 equiv. H₂O₂ in MeOH after 1 h reveals an intense band at 1659 cm⁻¹, which is typical of the carbonyl stretch associated with a non-metal-coordinated *para*-quinone. This compares well to the 1657 cm⁻¹ feature observed for **3**. Upon treatment with excess dithionite, this band disappears, suggesting that the ligand is reduced back to the diquinol state. We observed similar reversibility for **1**.²⁷ The intensity of the 3405 cm⁻¹ band, which can be at least partly attributed to O-H stretches from the quinol, decreases upon oxidation by H₂O₂, providing further evidence for the conversion of the quinols to *para*-quinones.

The changes to the ligand can also be monitored and analyzed indirectly by ¹H NMR. Although **2** and **3** are NMR-inactive, the addition of excess Zn(ClO₄)₂ promotes metal ion exchange and the formation of diamagnetic Zn(II) adducts with H₄qtp2 and its oxidized forms. Complex **1** had previously been studied in this manner.²⁷ Mixing the Zn(II) salt and the H₄qtp2 ligand led to a 3:10 mixture of complexes. These may either be conformers, solvent isomers, ionization isomers, or a combination thereof. The ¹H NMR resonances corresponding to the quinolic C-H groups in the free ligand and Zn(II) complex are offset, but these changes aren't large enough to unambiguously confirm the coordination of the quinols to the Zn(II). The resonances corresponding to the quinolic C-H and O-H bonds overlap at 6.5 ppm in CD₃CN. The integration of this peak decreases by ~4 upon oxidation by DDQ; this is consistent with the oxidation of the two quinols to *para*-quinones.

When 4 equiv. of H₂O₂ are added to a CD₃OD solution of **2** prior to treatment with Zn(II), 50% of the quinols have been oxidized by 1 h. Increasing the loading of oxidant to 8 equiv. increases the conversion to 70%, but further increasing the H₂O₂ loading to 16 equiv. does not improve the yield beyond this value. Without the Zn(II), no ligand-derived resonances are observed, suggesting that the Mn(II) remains bound to the oxidized components.

Measurement of Aliquot Group T_1 Relaxivity

The capability of **2** to serve as a MRI contrast agent was assessed with a 3 T clinical MRI scanner. The relationship between the concentration of **2** in 50 mM HEPES buffer (pH 7.0, 25 °C) and T_1 was linear and consistent with the Mn(II)-H₄qtp2 adducts remaining intact in solution. The slope yields a relaxivity (r_1) of 5.27 mM⁻¹ s⁻¹. The r_1 of **2** increases to 7.02 mM⁻¹ s⁻¹ upon the addition of 10 mM of H₂O₂. We attempted to measure r_1 for the isolated samples of the fully oxidized **3**, but the poor water solubility of this compound precluded these measurements.

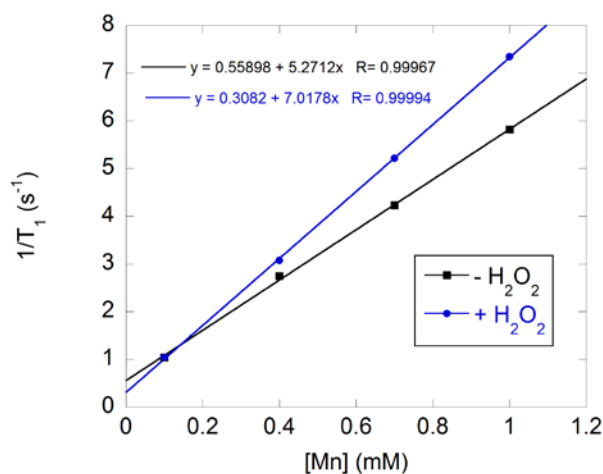


Figure 4.5. Plots of ($1/T_1$) versus Mn(II) concentration for **2** in the presence (blue) and absence (black) of 10 mM H₂O₂. All samples were run in 298 K aqueous solutions containing 50 mM HEPES buffered to pH 7.00, using a 3 T field provided by a clinical MRI scanner. The data were fit to the indicated linear equations; the y-intercepts were within error of $1/T_1$ measurements associated with two control samples that contained no Mn(II): pure water (0.39 s⁻¹) and 50 mM HEPES buffer (0.38 s⁻¹).

Cytotoxicity

The toxicity of **2** was tested using H9c2 cells in order to facilitate comparison to those of **1** and [Mn(Hptp1)(MeCN)](ClO₄)₂.²⁷ Compound **1** was the less toxic of the two latter probes,

and H9c2 cells could withstand concentrations of up to 1.0 μM indefinitely. The cells withstood a 10 μM dose of **1** for 4 h, but less than 50% survived after 24 h of continuous exposure.

Complex **2** is significantly less toxic than **1** (Figure 4.6). H9c2 cells can survive continuous contact with a 10 μM dose of **2** for at least 24 h. The viability of cells to a 4 h exposure to 50 μM of **2** is within error to that of the control. Higher concentrations of **2** do trigger cell death, but markedly greater percentages of the cells survive for all analyzed dosages and exposure times than for **1**. It should be noted that these cytotoxicities represent upper limits. A human or animal model would be expected to eliminate the probe, and the contact between individual cells and the contrast agent should therefore not be expected to approach 4 h.

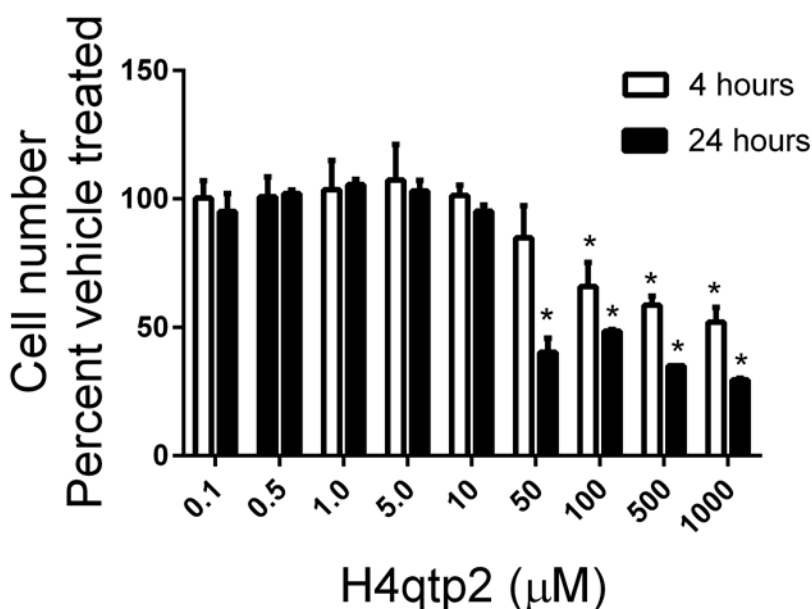


Figure 4.6. Cytotoxicity of **2** towards H9c2 cells. H9c2 cells were obtained from the American Tissue Type Collection (Manassas, VA, USA) and grown at 37 °C with 95% humidity and 5% CO₂. Cells were grown in Dulbecco's modified eagles medium (DMEM) supplemented with 10% fetal bovine serum. Experiments were performed at 70-80% confluence. To determine the cytotoxic effects of **2**, H9c2 cells were exposed to increasing concentrations of **2** (0.1 - 1000 μM) or its vehicle in DMEM for 4 or 24 hr. Cell number was assessed using the CyQUANT Cell

Proliferation Assay Kit (Life Technologies Corporation, Carlsbad, CA) per manufacturer's instructions. Cell number was expressed as percentage of the vehicle-treated cells. Values are expressed as mean and standard deviation and represent 2-4 experiments performed in triplicate. The bars marked with an * display a significant difference from the vehicle-treated cell number for corresponding time period ($p < 0.05$).

Ex Vivo Biological MRI

The improved T_1 response to H_2O_2 and lower cytotoxicity prompted us to seek a means to test the ability of **2** to function *in vivo*. The primary complication in finding an appropriate system is that *in vivo* concentrations of ROSs in normal and aberrant physiology have not been measured to high degrees of certainty.⁵³ The baseline oxidative activity in certain environments may be sufficiently high to activate the sensor without oxidative stress. Alternatively, inducing oxidative stress in other tissues may be insufficient to activate the sensor to a noticeable degree.

The drug doxorubicin (DOX) has been used to treat a variety of cancers, but its clinical doses are strictly limited by its cardiotoxicity.⁵⁴ High dosages of DOX have been found to induce oxidative stress in the heart.⁵⁵ Anti-oxidants have been documented to decrease the drug's cardiotoxicity.^{56, 57}

The hearts of rats intravenously dosed with the responsive contrast agent 20 min prior to MRI displayed noticeably higher contrast than the probe-free controls, as indicated by lower T_1 values throughout the myocardium (Figure 4.7). This demonstrates that **2** can be used to improve cardiac imaging.

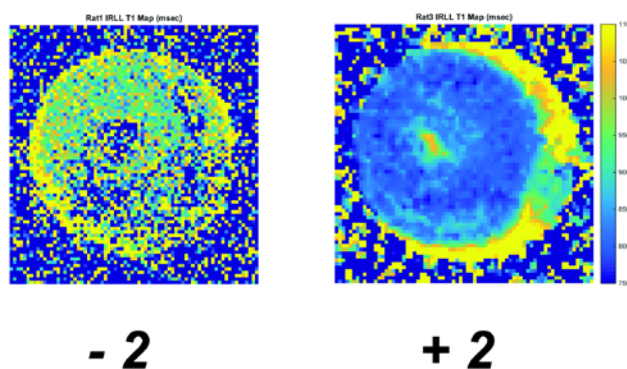


Figure 4.7. T_1 maps of rat hearts treated without and with contrast agent **2**. Neither rat was pre-administered DOX prior to MRI. With this series of experiments, treatment with **2** increases R_1 from 1.080 s^{-1} to 1.246 s^{-1} .

We next performed *ex vivo* heart imaging on rats that had been treated with DOX and **2**. High doses of DOX were administered to the non-control animals 72 h before imaging. The contrast agent was introduced intravenously 20 min before MRI. Rats that had been pre-administered DOX displayed between a 7 (± 3)% better T_1 response. Figure 4.8 show the best response that was observed, which corresponds to a 10% increase in R_1 . In all cases, the contrast difference is limited to the myocardium; the surrounding fluid is not influenced by treatment with either DOX or **2**. The hearts appeared identical within error to each other when either viewed by T_2 -weighted MRI or analyzed after a shorter 48 h exposure to DOX. The large variability and the small magnitudes of the T_1 response limit what we can currently say about the role of oxidative stress in the cardiotoxicity of DOX. Histological studies on the hearts do not detect oxidative damage. The profiles of the tissues' gene expression, conversely, suggest that cellular responses to oxidative stress have been activated. In concert, the data suggest that the 72 h timepoint may coincide with the onset of oxidative stress. This in turn may at least partly explain the large variability and the incomplete turn-on of the sensor.

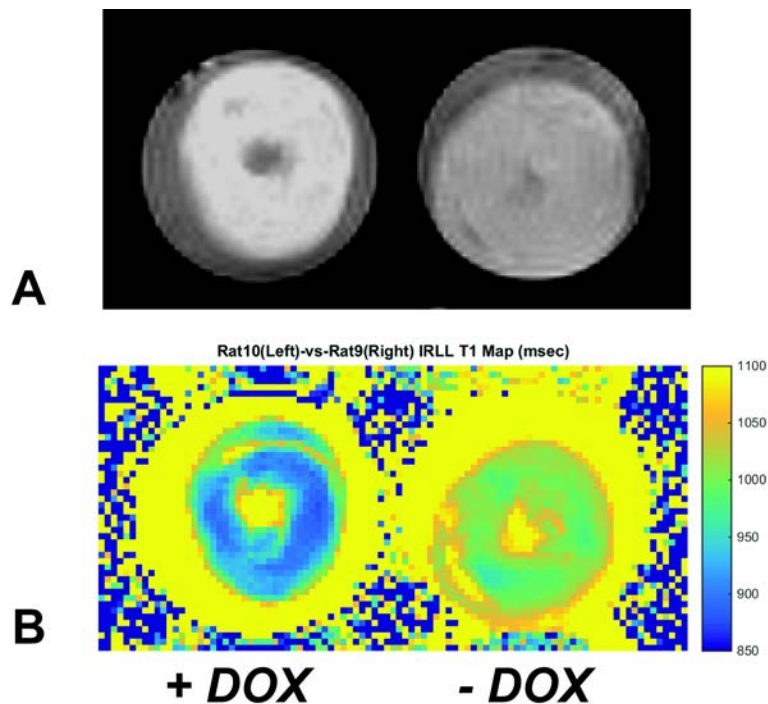


Figure 4.8. *Ex vivo* cardiac MRI of rats treated with contrast agent **2**. The images on the left correspond to a rat that was treated with DOX 72 h prior to imaging. (A) MRI of the +DOX and –DOX hearts. The two hearts were scanned simultaneously. (B) T_1 map of the hearts shown in panel (A). For this series of experiments, the DOX pre-treatment increases R_1 from 0.995 s^{-1} to 1.092 s^{-1} .

Anti-oxidant Activity

Previously reported H_2O_2 sensors from our laboratory were found to behave as potent anti-oxidants.²⁷ Complex **1** served as an excellent mimic of superoxide dismutase (SOD) and could donate hydrogen atoms more readily than ascorbic acid, as assessed by the 2,2-diphenyl-1-picryl-hydrazyl hydrate (DPPH) assay.

The ability of **2** to degrade superoxide was tested using a standard technique that uses the reaction between xanthine oxidase and xanthine to generate O_2^- and a subsequent reaction with the chemiluminescent probe lucigenin to detect it.^{39, 40} Complex **2** successfully intercepts O_2^-

before its reaction with lucigenin, although it does not do so as efficiently as either **1** or $[\text{Mn}(\text{Htp1})(\text{MeCN})](\text{ClO}_4)_2$ (Figure 4.9).²⁷ The IC_{50} value for **2** was found to be 18.2 nM. Although this is the highest of the values for the three investigated Mn(II) complexes, the results for the two quinol-containing complexes appear to be approximately equal to each other.

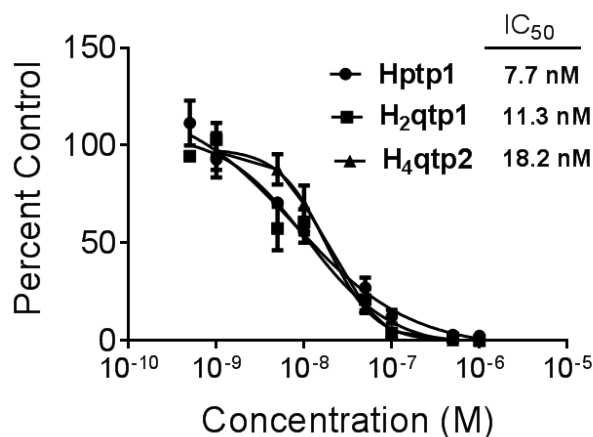


Figure 4.9. Superoxide scavenging effects of **1**, **2**, and $[\text{Mn}(\text{Htp1})(\text{MeCN})](\text{ClO}_4)_2$. The Mn(II) complexes are identified by their ligand. Superoxide was generated using a hypoxanthine-xanthine oxidase reaction and detected using the chemiluminescent probe lucigenin. Reactions were carried out in 50 mM Tris-HCl (pH 8.0). Data for the various concentrations of Mn(II) complex are expressed as a percentage of luminescence in the presence of vehicle.

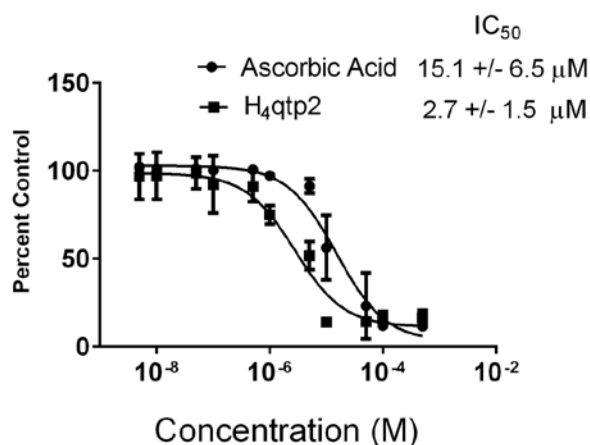


Figure 4.10. DPPH free radical scavenging assay of **2** and ascorbic acid. The anti-oxidants were added to DPPH and incubated in the dark for 30 min at 298 K. Spectroscopic measurements

were performed at 517 nm. The data were normalized to the absorbance in the presence of vehicle. All experiments were performed in triplicate and repeated twice.

Complex **2** is also a competent oxidant as assessed by the DPPH assay (Figure 4.10), which tests the abilities of compounds to donate hydrogen atoms to 2,2-diphenyl-1-picrylhydrazyl radical hydrate.^{41-43, 58} In this assay, the hydrazine product is monitored by UV/vis. The IC₅₀ for **2** was found to be 2.7 μM; ascorbic acid was found to have an IC₅₀ value of 15.1 μM under the same conditions.

4.4 Discussion

Previous work from our laboratory found that a Mn(II) complex with the H₂qtp1 ligand, [Mn(H₂qtp1)MeCN]](OTf)₂ (**1**), acts as a turn-on sensor for H₂O₂ when monitored by magnetic resonance imaging (MRI).²⁷ The reaction with H₂O₂ oxidizes the quinol portion of the ligand to a *para*-quinone, which binds to metal ions less avidly and can be more readily displaced by water molecules. Ligand oxidation is therefore believed to result in greater metal ion aquation, which in turn, increases the r_1 value associated with the contrast agent. One significant drawback associated with **1** was that its relaxivity response was slight, amounting to only about 0.6 mM⁻¹ s⁻¹ even with a large excess of H₂O₂. This represents a 12% increase from the starting r_1 of 4.73 mM⁻¹ s⁻¹.

Reasoning that the presence of a second redox-active group would result in a greater spectroscopic response, we prepared the H₄qtp2 ligand by replacing one of the pyridines with another quinol (Scheme 4.1). The synthesis of the ligand is more difficult than that used to prepare H₂qtp1, but pure product can still be obtained in good yield in three steps from commercially available starting materials. The installation of the fourth arm onto the 1,2-ethanediamine backbone is the major complication, and we hypothesize that steric repulsions

with the other arms of the ligand hinder the addition of the last quinol. We had encountered similar difficulties in the syntheses of sterically encumbered ligands used to support non-heme iron catalysis.⁵⁹

Much like H₂qtp1, the H₄qtp2 ligand binds Mn(II) readily in its neutral form. We were unable to obtain crystalline adducts with either Mn(OTf)₂ or Mn(ClO₄)₂, the former of which was used to prepare [Mn(H₂qtp1)MeCN](OTf)₂ (**1**).²⁷ The ligand was instead complexed to MnBr₂. The resultant [Mn(H₄qtp2)Br₂] (**2**) features two Mn-Br bonds but no Mn-O bonds to the quinol subunits (Figure 4.1). The structure of **1**, conversely, contains a Mn-O bond to the quinol group of the ligand.²⁷ The difference in the structures can be rationalized by the much stronger metal-binding affinity of bromide ions relative to triflates. We do not believe that the structure in Figure 4.1 is strictly maintained in aqueous solution since the measured log(*K*) of 10.2 for the H₄qtp2-Mn(II) adduct is reasonably close to the 10.7 value for the H₂qtp1-Mn(II) adduct. The loss of even one donor atom should more substantially impact the ligand's binding affinity for the metal.^{35, 60} The similar binding constants would suggest that the two ligands coordinate to the Mn(II) ions through the same number of donor atoms.

Much like **1**, complex **2** is moderately stable in aerobic aqueous solutions. The ligand remains attached to the metal, as assessed by the lack of ¹H NMR resonances for solutions of **2** in D₂O. Only slight ligand oxidation is observed upon 12 h of exposure to air. Complex **2** is much more susceptible to metal substitution than **1**, and a 3 h treatment of a 0.10 mM solution of the Mn(II) complex with 0.10 mM Fe(ClO₄)₂ is sufficient to remove approximately 80% of the manganese. Biological concentrations of peptide-free transition metal ions are not anticipated to approach this level, however,⁶¹ and metal displacement is unlikely to significantly impact the ability of the probe to function in most biological environments.

When **2** reacts with H₂O₂, the ligand is preferentially oxidized, with the manganese remaining in the +2 oxidation state (Figure 4.4). Depending upon the concentration of H₂O₂ and the length of exposure, either one or two of the quinols is oxidized to the *para*-quinone, as confirmed by UV/vis, IR, MS, and crystallography. The former three techniques were previously used to confirm the oxidation of the H₂qtp1 ligand, but the oxidized product of **1** was not isolated and structurally characterized.²⁷ Complex **2**, conversely, was successfully crystallized after its oxidation to [Mn(qtp2)Br₂] (**3**) by the alternative oxidant DDQ. The Mn(II)-containing components of the crystals are remarkably similar, and in both structures, the Mn-Br and Mn-N bonds are consistent with a high-spin Mn(II) metal center. The major differences in the two structures are the lengths of the C-O bonds, which contract by 0.14 Å upon oxidation. The shortened C-O bonds provide strong evidence for the formation of the *para*-quinone.

Spectroscopic measurements confirm that the oxidation is largely limited to the ligand; at 30 min, the EPR analysis of the reaction between **2** and H₂O₂ indicates that the manganese remains in the +2 oxidation state. Parallel ¹H NMR analysis does not detect any free ligand or Mn(III) species. UV/vis spectroscopy, however, suggests that the metal begins to oxidize by 3 h; this process was not observed for the monoquinol complex. Complex **2** therefore seems to be more sensitive to over-oxidation than **1**. The contrast agent, however, can be administered and used to enhance MRI imaging comfortably within 3 h.

As with complex **1**, excess H₂O₂ does not fully oxidize **2**. The NMR measurements suggest that ~70% of the quinols are converted to *para*-quinones under a prolonged exposure to 8 equiv. of the oxidant; this value is identical within error to the ~70% oxidation found for the response of **1** to excess H₂O₂.²⁷ The response, however, is noticeably slower and appears to have

an induction period (Figure 4.4). This may indicate that the H_2O_2 requires time to displace the bromides, but a fuller kinetic analysis is needed to interrogate this.

Complex **2** behaves as an excellent MRI contrast agent. The $5.27 \text{ mM}^{-1} \text{ s}^{-1} r_1$ value is higher than those of our previously reported mononuclear Mn(II) contrast agents with the structurally similar ligands Htp1 ($4.39 \text{ mM}^{-1} \text{ s}^{-1}$) and $\text{H}_2\text{qtp1}$ ($4.73 \text{ mM}^{-1} \text{ s}^{-1}$)^{26, 27} and is high for a mononuclear Gd(III)- or Mn(II)-containing complex.^{18, 62} The value is within error of the $5.26 \text{ mM}^{-1} \text{ s}^{-1}$ value measured for $[\text{Mn}(\text{H}_2\text{O})_6]^{2+}$ under the same conditions,⁶³ but since ^1H NMR and EPR demonstrate that the $\text{H}_4\text{qtp2}$ complex remains intact in water, we believe that this is coincidental. The heightened r_1 value relative to the Htp1 and $\text{H}_2\text{qtp1}$ complexes may be attributed to more extensive outer-sphere interactions with water molecules. The number of hydrogen bonds to outer-sphere water molecules would be anticipated to scale with the number of hydroxyl groups on the ligand.

Upon exposure to H_2O_2 , the relaxivity increases markedly. The $1.75 \text{ mM}^{-1} \text{ s}^{-1}$ response is almost three times greater than that of **1**²⁷ and represents a 33% increase. To the best of our knowledge, **2** is the third MRI contrast agent with a direct turn-on r_1 response to H_2O_2 . Other complexes either display a turn-off response²¹ or require a co-analyte.²⁹ In 2013, Almutairi and co-workers reported that Gd_2O_3 nanoparticles coated with a biodegradable polymer exhibited a 10-fold increase in r_1 upon exposure to excess H_2O_2 .²⁸ Although the response is stronger, the irreversibility of the response would preclude the nanoparticle sensors from tracking fluctuations in the concentration of H_2O_2 .

One concern about introducing redox-active metals into a biological system is that they have the capacity to increase the concentrations of ROSs through reactions with O_2 . The $\text{H}_2\text{qtp1}$

complex **1** was instead found to be a strong anti-oxidant in that it can catalytically degrade superoxide and transfer hydrogen atoms to radical species.²⁷ Despite the significant structural differences, compound **2** behaves similarly. The superoxide dismutase (SOD) activity is slightly worse than that for **1**, but its IC₅₀ value still ranks **2** amongst the best small molecule SOD mimics (Figure 4.9).^{64, 65} Much like **1**, complex **2** has an electrochemical feature at about 300 mV vs. NHE, but this feature is much less reversible. The lesser reversibility may explain the attenuated SOD activity. The hydrogen atom donating ability of **2** was measured with the DPPH assay. By this measure, the complex was found to be a superior anti-oxidant to ascorbic acid (Figure 4.10). Due to the sensitivity of the assay, direct comparison of **1** and **2** is difficult, but based on their reactivity relative to a common ascorbic acid standard, they appear to be roughly equivalent.

One drawback associated with **1** was that a high dose was required to observe a significant spectroscopic difference between the oxidized and reduced forms. Achieving such a high *in vivo* concentration is complicated by its cytotoxicity. A short-term (4 h) impact on the viability of H9c2 cells is observed at a 100 μM concentration of **1**, and the mortality rate markedly increases as the concentration is raised to 1.0 mM. Complex **2** is less toxic, and H9c2 cells can withstand higher concentrations for longer periods of contact (Figure 4.6). These higher concentrations are not strictly necessary due to the greater r_1 difference between reduced and oxidized forms of the probe. The physiological basis for the lower toxicity is currently unknown and remains the subject of investigation.

Compound **2** was successfully used in the *ex vivo* imaging of rat hearts (Figures 4.7 and 4.8). When administered intravenously, **2** accumulates to high enough concentrations to improve the contrast of cardiac images. The response to oxidative stress appears to be at least partly

retained, and we observe modest improvements to the MRI contrast when the rats are given a high dose of DOX 72 h prior to the administration of **2** and imaging. The 7 (\pm 3)% increase in r_1 is much less than the 33% improvement observed in the *in vitro* measurements. Based on the histology, we currently speculate that the oxidative stress has not yet fully manifested by 72 h, but additional experiments are needed to confirm that this is indeed a contributing factor in the partial sensor activation. If our hypothesis is validated by further experiments, sensor **2** may well be detecting oxidative stress before it damages tissues.

4.5 Conclusions

The addition of a second redox-active quinol to a previously reported MRI contrast agent sensor for H₂O₂ markedly increases its relaxivity response, albeit at the cost of some stability to adventitious transition metal ions and O₂. The fundamental reactivity with H₂O₂ appears to be the same for the Mn(II) complexes with the monoquinol and diquinol ligands, in that the enhancement in r_1 is correlated to the oxidation of the quinols to more weakly metal-binding *para*-quinone groups. The second quinol increases the r_1 values of both the reduced and oxidized forms of the sensor, and the incorporation of these highly hydrogen-bonding groups appears to be a viable strategy for the production of higher-relaxivity mononuclear contrast agents. The ability to isolate the oxidized product allows us to confirm the molecular changes associated with the activation of the sensor. The replacement of one of the pyridine rings with a second quinol also reduces the cytotoxicity through an unknown mechanism. The complex with the diquinol ligand displays anti-oxidant activity that strongly resembles that of the monoquinol complex. The better T_1 response and lessened cytotoxicity allowed us to successfully use **2** in *ex vivo* cardiac imaging.

Appendix

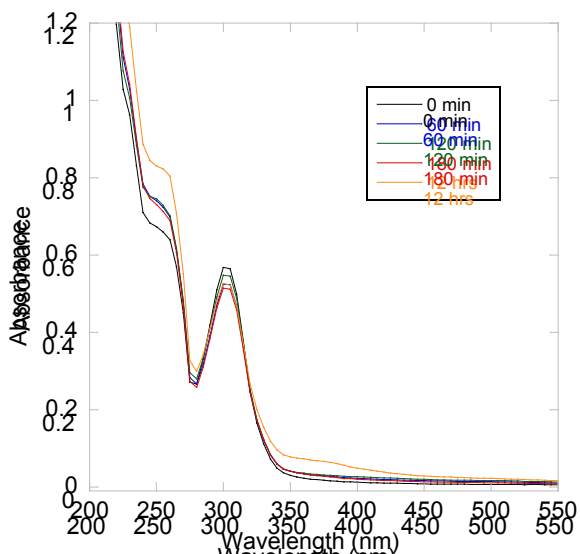


Figure 4A.1. UV/Vis spectra depicting the stability of a 0.10 mM solution of [Mn(H₄qtp2)Br₂] (2) in MeOH to air. The reaction was scanned at 0, 1, 2, 3, and 12 h. The band at 302 nm is characteristic of quinol functional groups.

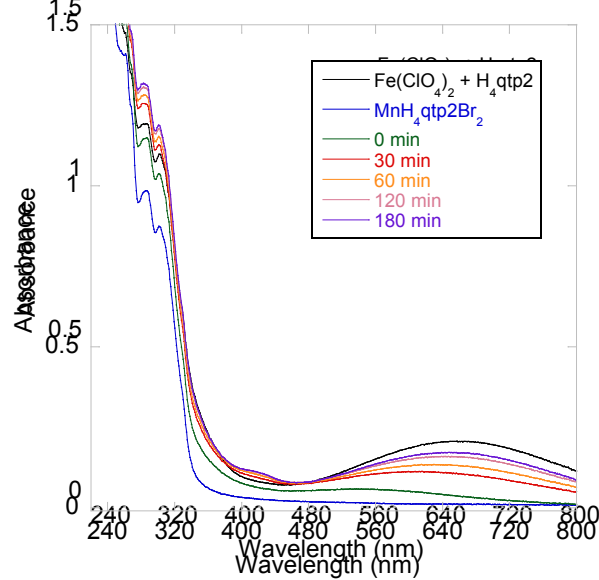


Figure 4A.2. Spectrophotometric analysis of the reaction between 0.10 mM Fe(ClO₄)₂ and 0.10 mM 2 in MeOH at 298 K. The UV/vis spectrum of the product formed from 0.10 mM Fe(ClO₄)₂

and 0.10 H₄qtp2 (black) and that corresponding to 0.10 mM **2** are provided for comparison.

Approximately 80% of Mn(II) has been replaced by Fe(II) by 3 h.

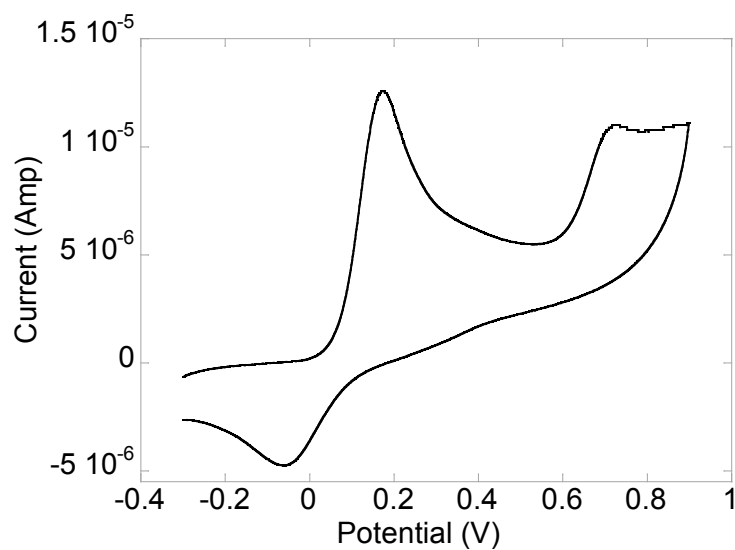


Figure 4A.3. Cyclic voltammetry of 1.0 mM **2** in 0.10 M phosphate buffer ($\text{NaH}_2\text{PO}_4/\text{Na}_2\text{HPO}_4$, pH=7.2). The scan rate was 100 mV/s. For the quasi-reversible feature: $E_{1/2} = 57$ mV vs. Ag/AgCl, $\Delta E = 232$ mV. An irreversible feature with $E_{pc} = 725$ mV is also observed.

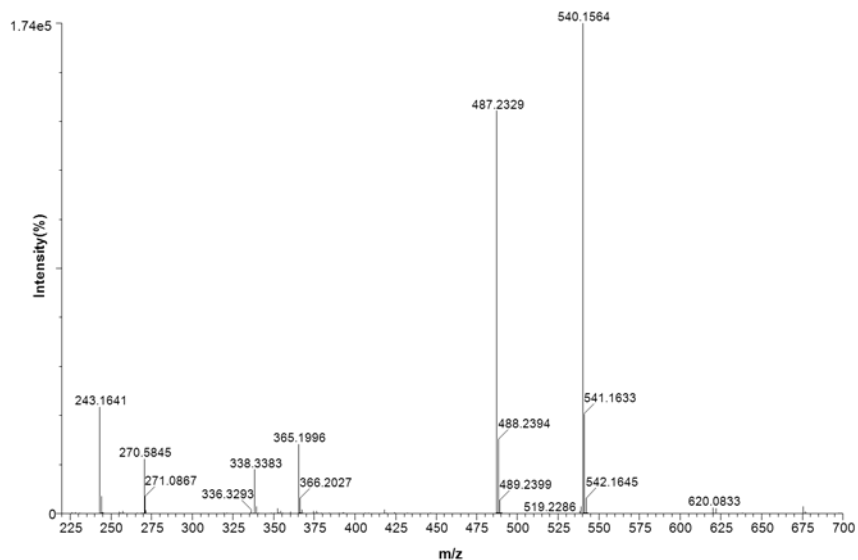


Figure 4A.4. Mass spectrometry (ESI) of **2** in MeOH. The 540.1564 m/z feature is assigned to the singly deprotonated Mn(II) complex $[\text{Mn}(\text{H}_3\text{qtp}2)]^+$ (calculated m/z = 540.1569). The 487.2329 m/z feature is assigned to $[\text{H}_5\text{qtp}1]^+$, the singly protonated ligand (calculated m/z = 487.2345).

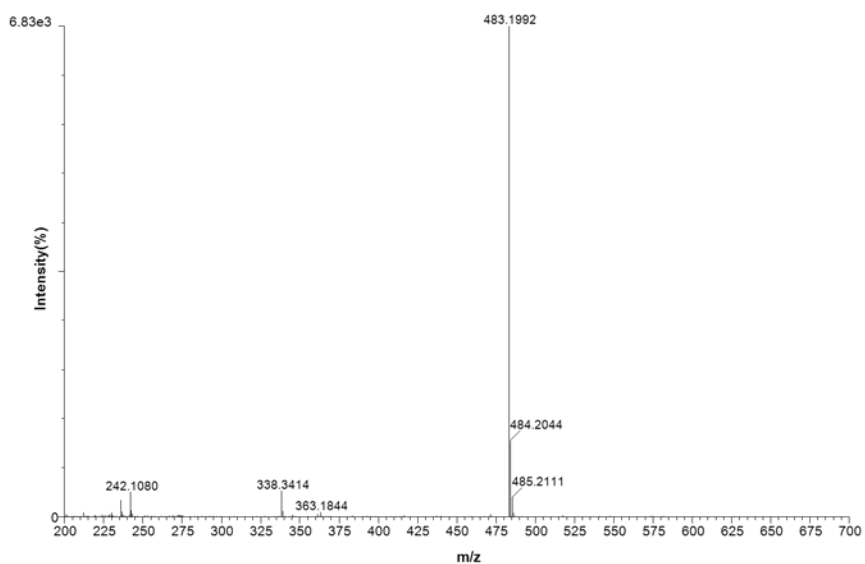


Figure 4A.5. Mass spectrometry (ESI) of $[\text{Mn}(\text{qtp}2)\text{Br}_2]$ (**3**) in MeCN. The 483.1992 m/z feature is assigned to $[\text{Hqtp}2]^+$, the singly protonated form of the diquinone qtp2 ligand (calculated m/z = 483.2032).

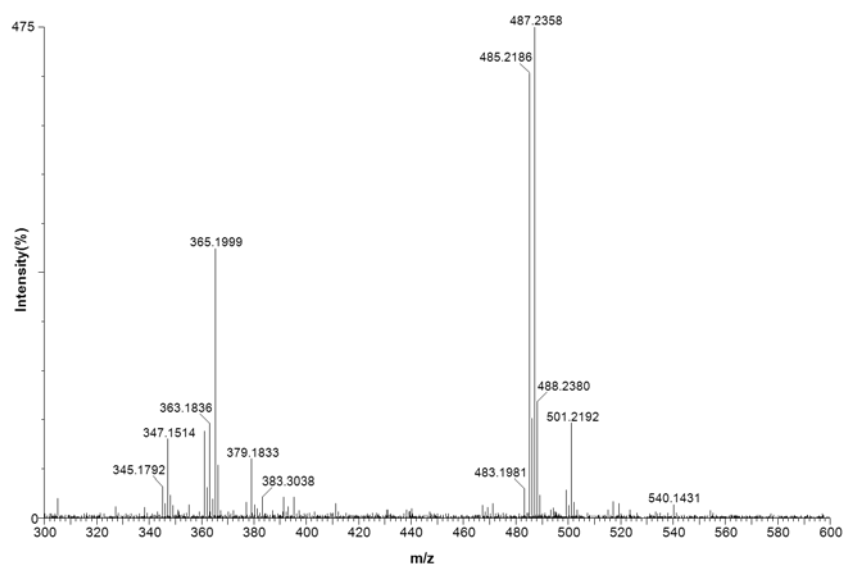


Figure 4A.6. Mass spectrometry (ESI) of a mixture of **2** in H₂O and 4 equiv. of H₂O₂. The reaction was allowed to proceed for 30 min. The 483.1981 m/z feature is assigned to [Hqtp2]⁺ (calculated m/z = 483.2032), the singly protonated form of the fully oxidized (diquinone) ligand. The 485.2186 m/z feature is assigned to [H₃qtp2]⁺ (calculated m/z = 485.2189), the singly protonated form of the partially oxidized (monoquinone) ligand, H₂qtp2. The 487.2358 m/z feature is assigned to [H₅qtp1]⁺ (calculated m/z = 487.2345).

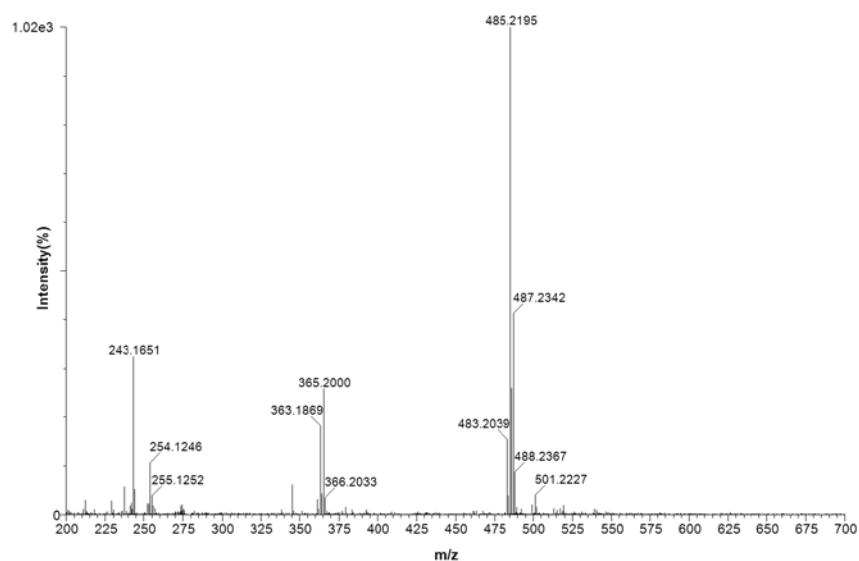


Figure 4A.7. Mass spectrometry (ESI) of a reaction between **2** and 4 equiv. of H_2O_2 in MeOH.

The reaction was allowed to proceed for 60 min. The 483.2039 m/z feature is assigned to $[\text{Hqtp2}]^+$ (calculated m/z = 483.2032), the singly protonated form of the fully oxidized (diquinone) ligand. The 485.2195 m/z feature is assigned to $[\text{H}_3\text{qtp2}]^+$ (calculated m/z = 485.2189), the singly protonated form of the partially oxidized (monoquinone). The 487.2342 m/z feature is assigned to $[\text{H}_5\text{qtp1}]^+$ (calculated m/z = 487.2345), the singly protonated form of the non-oxidized ligand.

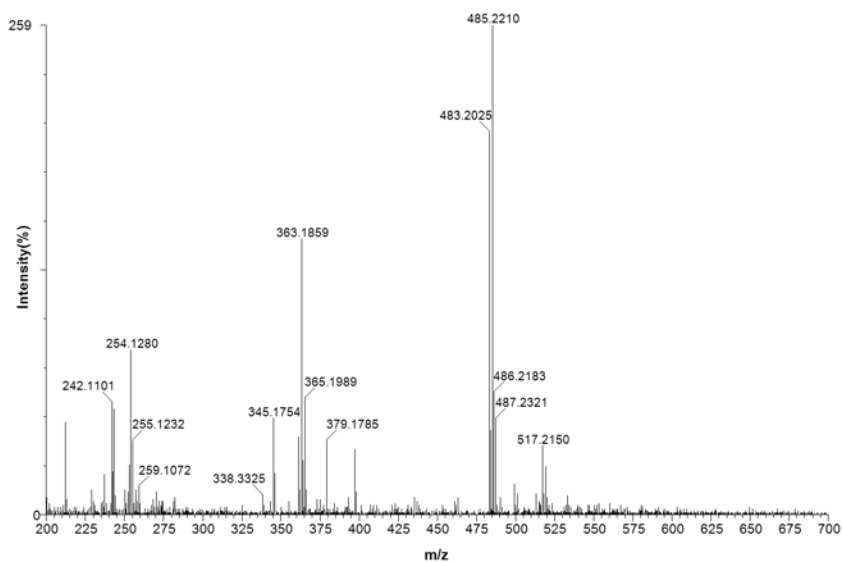


Figure 4A.8. Mass spectrometry (ESI) of a reaction between **2** and 8 equiv. of H₂O₂ in MeOH.

The reaction was allowed to proceed for 60 min. The 483.2025 m/z feature is assigned to [Hqtp2]⁺ (calculated m/z = 483.2032). The 485.2210 m/z feature is assigned to [H₃qtp2]⁺ (calculated m/z = 485.2189). The 487.2321 m/z feature is assigned to [H₅qtp1]⁺ (calculated m/z = 487.2345).

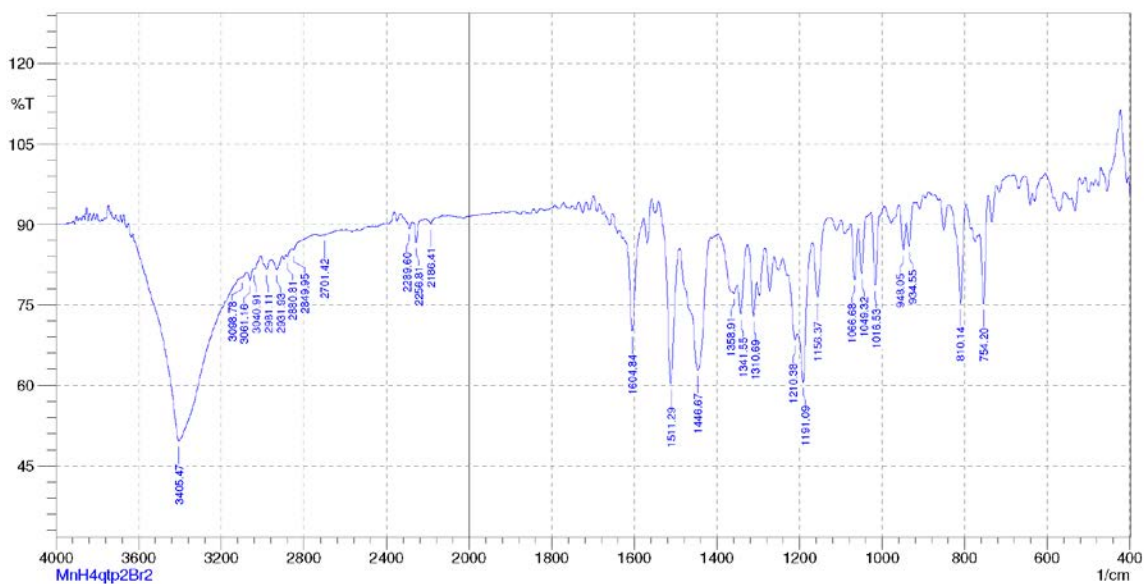


Figure 4A.9. IR spectrum of **2** (KBr). The 3405 cm^{-1} feature is assigned to the O-H stretches associated with the quinol groups of the $\text{H}_4\text{qtp2}$ ligand. The 1605 cm^{-1} feature is assigned to the C-N stretches associated with the metal-coordinated pyridine rings.

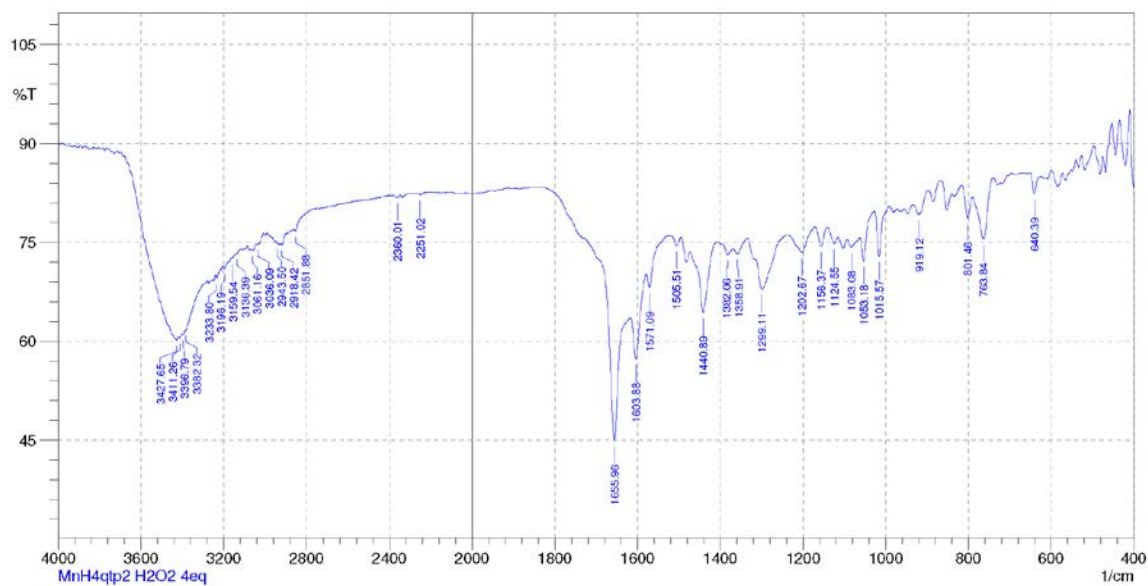


Figure 4A.10. IR spectrum of the crude product from the reaction between 1.0 mM **2** and 4.0 mM H₂O₂ in MeOH. After allowing 30 min to react, the solvents were stripped, yielding the solid used to prepare the sample (KBr). The peak at 1659 cm⁻¹ is assigned to a C=O stretch for the quinone groups formed upon the partial oxidation of the H₄qtp2 ligand.

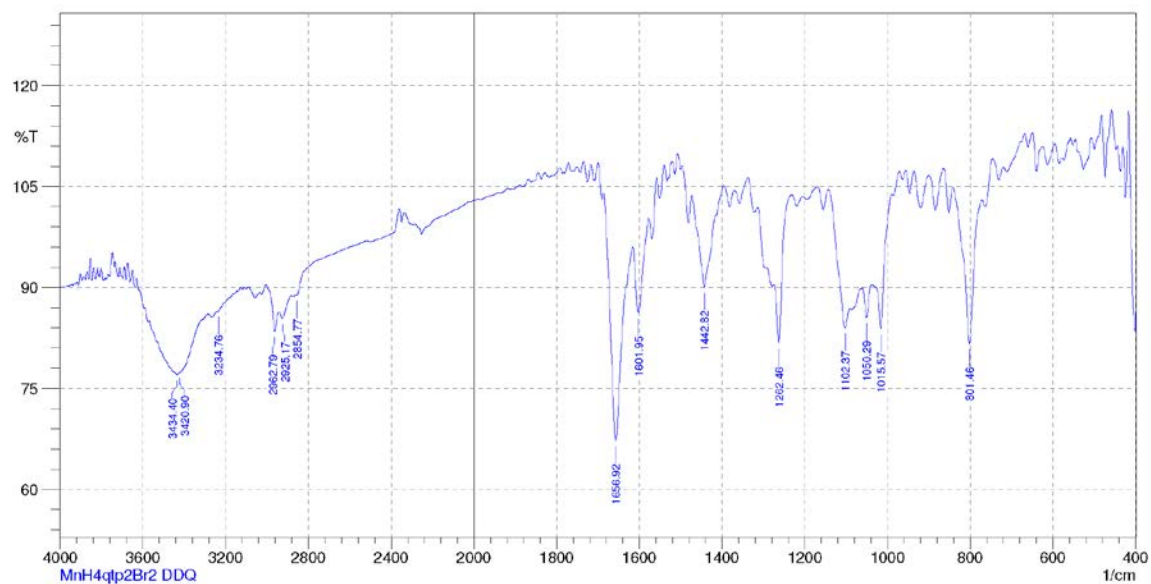


Figure 4A.11. IR spectrum of **3** (KBr). This compound was prepared cleanly from the oxidation of **2** by 2,3-dichloro-5,6-dicyano-1,4-benzoquinone (DDQ). The peak at 1657 cm^{-1} is assigned to the C=O stretches of the quinone subunits.

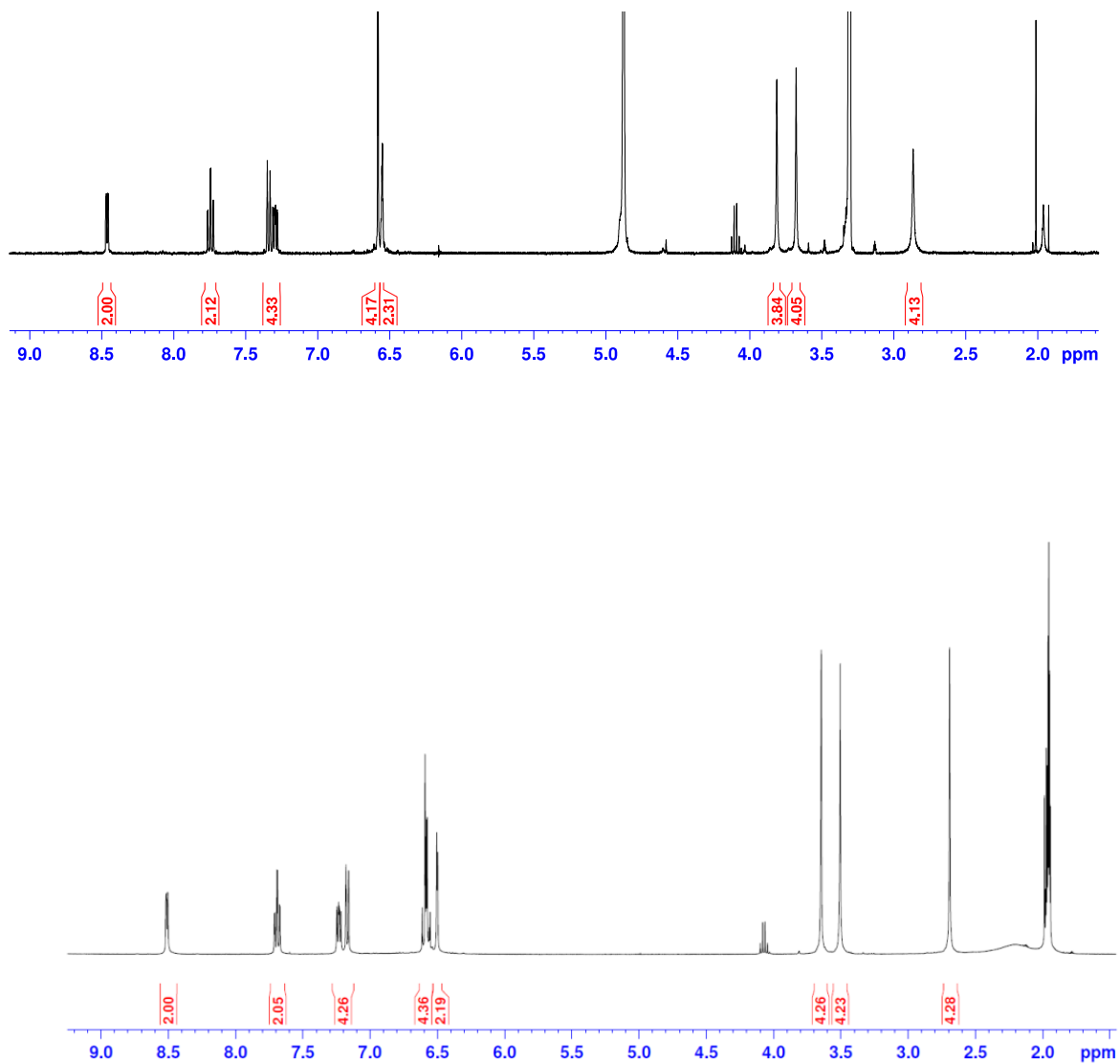


Figure 4A.12. ¹H NMR spectra of H₄qtp2 in CD₃OD (top) and CD₃CN (bottom). The peaks around 6.5 ppm can be attributed to the O-H and C-H protons on the quinol subunits.

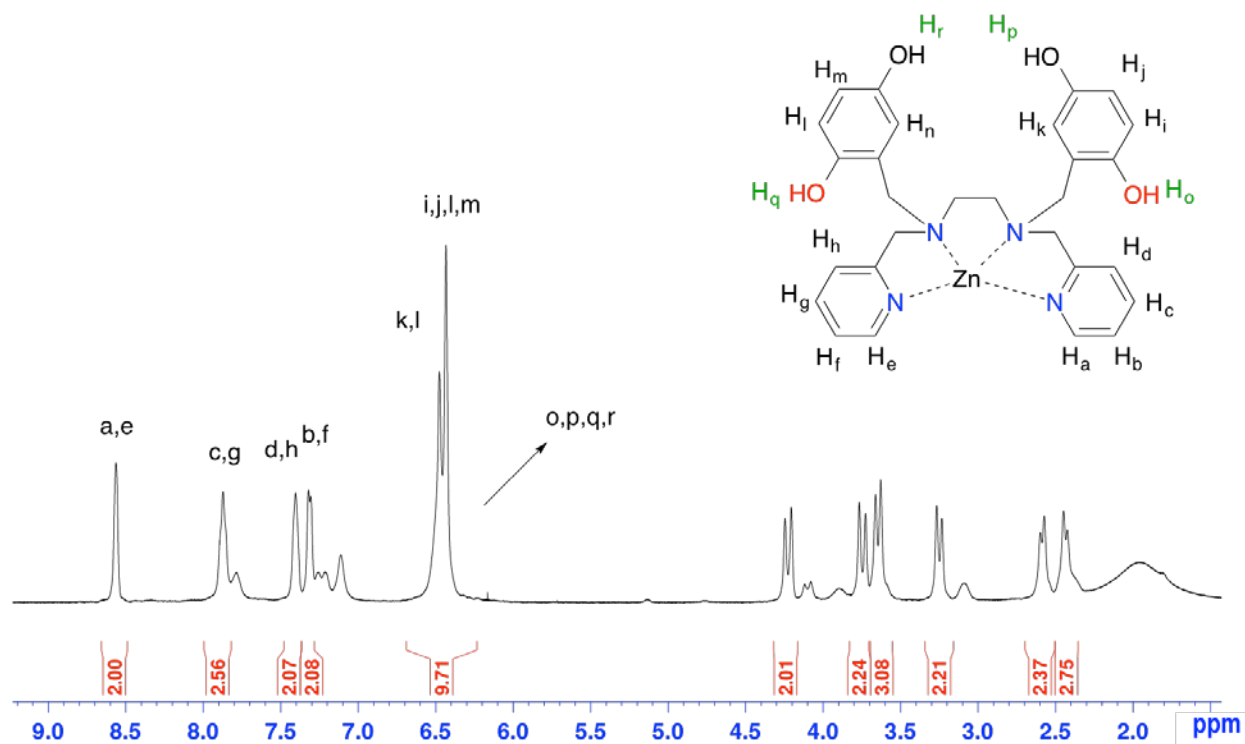


Figure 4A.13. ¹H NMR spectrum of the diamagnetic product from the reaction between 10 mM **2** and 20 mM Zn(ClO₄)₂ in CD₃CN. The reaction was given 2 h to equilibrate. The peaks observed between 7.0 and 8.8 ppm can be assigned to the protons on the pyridine subunits. The peaks around 6.5 ppm can be attributed to the O-H and C-H protons on the quinol subunits.

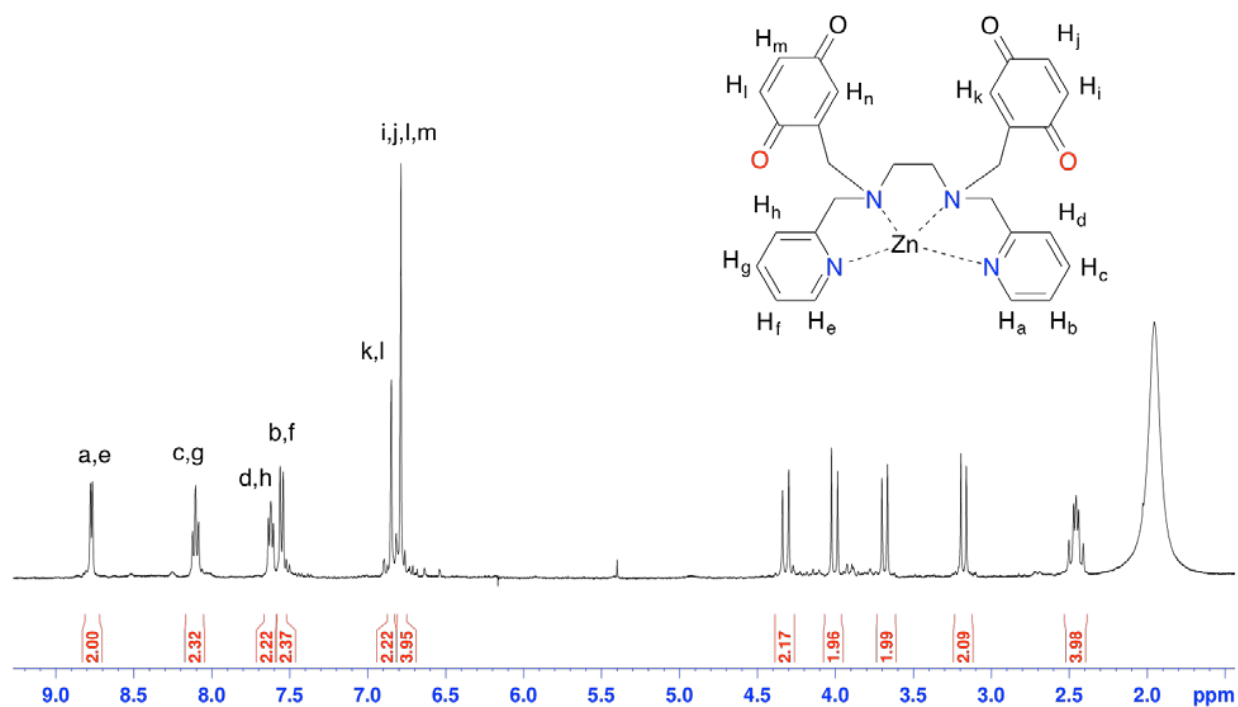


Figure 4A.14. ¹H NMR spectrum of the diamagnetic product from the reaction between 10 mM **3** and 20 mM Zn(ClO₄)₂ in CD₃CN. The reaction was given 2 h to equilibrate. The decreased intensities of the peaks at ~6.8, relative to those in **Figure 4A.13**, correspond to a loss of 4 H nuclei upon oxidation.

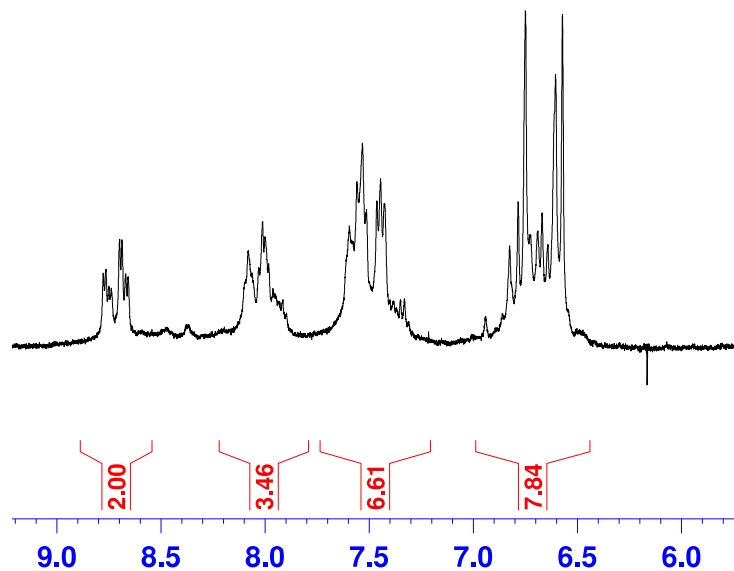


Figure 4A.15. ^1H NMR spectrum of the diamagnetic product between **2**, 4 equiv. of H_2O_2 , and 2 equiv. of $\text{Zn}(\text{ClO}_4)_2$ in CD_3CN . The Mn(II) complex and H_2O_2 were allowed to react for 1 h. The subsequent reaction with Zn(II) was provided 2 h to equilibrate. The spectrum is consistent with a mixture of the species observed in **Figures 4A.13** and **4A.14**. Approximately 55% of the quinols have been oxidized.

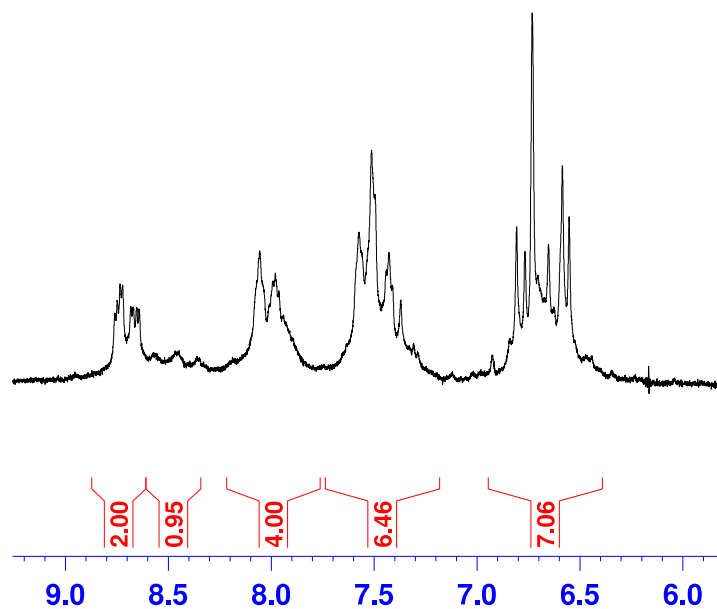


Figure 4A.16. ¹H NMR spectrum of the diamagnetic product between **2**, 8 equiv. of H₂O₂, and 2 equiv. of Zn(ClO₄)₂ in CD₃CN. The Mn(II) complex and H₂O₂ were allowed to react for 1 h. The subsequent reaction with Zn(II) was provided 2 h to equilibrate. The spectrum is consistent with a mixture of the species observed in **Figures 4A.13** and **4A.14**. Approximately 75% of the quinols have been oxidized to *para*-quinones.

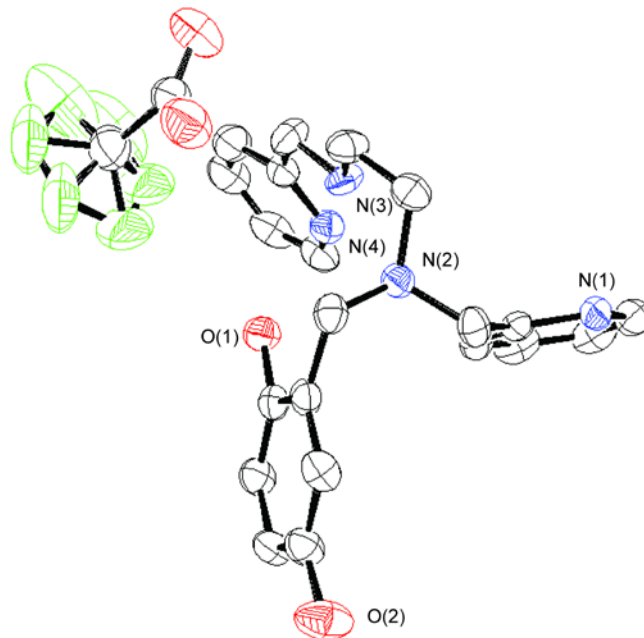


Figure 4A.17. ORTEP representation of the ligand precursor *N*-(2,5-dihydroxybenzyl)-*N,N'*-bis(2-pyridinylmethyl)-1,2-ethanediammonium trifluoroacetate. All thermal ellipsoids are drawn at 50% probability. Hydrogen atoms are excluded for clarity. The CF₃ group on the trifluoroacetate ion is disordered over two positions. The crystals were grown by diffusing ether into a MeOH solution of crude *N*-(2,5-dihydroxybenzyl)-*N,N'*-bis(2-pyridinylmethyl)-1,2-ethanediamine.

Table 4A.1. Doxorubicin rat serum enzyme and histology results.

Rat #	DOX	CK (U/L)	ALT (U/L)	Heart Histology
1	No-48	IS	IS	No lesion detected
2	Yes-48	574	96	No lesion detected
3	No-48	155	58	No lesion detected
4	Yes-48	202	85	No lesion detected
5	No-48	IS	IS	No lesion detected
6	Yes-48	IS	IS	No lesion detected
7	No-48	IS	IS	No lesion detected
8	Yes-48	IS	IS	No lesion detected
9	No-72	238	72	No lesion detected
10	Yes-72	4112-SS	172-SS	No lesion detected
11	No-72	328	61	No lesion detected
12	Yes-72	397	88	No lesion detected
13	No-72	1137	39	No lesion detected
14	Yes-72	69	31	Minimal necrosis- considered background
15	No-72	IS	IS	No lesion detected
16	Yes-72	IS	IS	No lesion detected
17	No-72	1370	69	No lesion detected
18	Yes-72	668	103	No lesion detected
19	No-72	446	100	No lesion detected
20	Yes-72	489	139	No lesion detected
21	No-72	287	40	No lesion detected
22	Yes-72	697	108	No lesion detected
23	No-72	247	72	No lesion detected
24	Yes-72	319	102	No lesion detected

U/L- Units per liter, IS- Insufficient Sample, SS- Short Sample, DOX- doxorubicin, ALT- alanine aminotransferase (measure of liver damage), CK- creatine kinase (measure of heart damage).

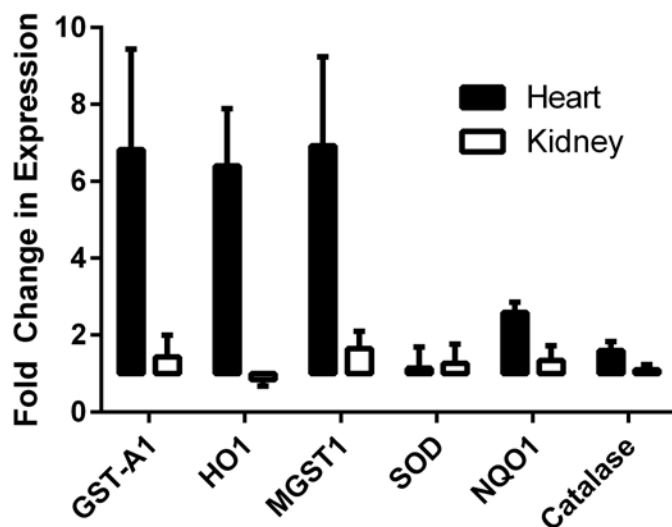


Figure 4A.18. Gene expression in the hearts and kidneys of doxorubicin-treated rats. Expression for each gene is expressed as fold change in expression compared to vehicle treated rats. RNA was extracted using a combination of TRIzol (Invitrogen) and the RNeasy Plus Kit (Qiagen, Valencia, CA). Hearts and kidney were homogenized in Trizol (Invitrogen, 1mL trizol/100mg tissue) using a polytronix tissue homogenizer (Fisher Scientific, Pittsburg, PA) for 30 s. Samples were centrifuged at $10,000 \times g$ for fifteen minutes at $4^{\circ}C$. Chloroform phase separation was performed and the aqueous phase was collected and combined with three volumes of 70% ethanol. The mixture was added to the column of the RNeasy Plus kit, and the RNA was isolated per manufacturer's instructions. cDNA was synthesized using the iScript cDNA Synthesis Kit (Bio-Rad) using 500 ng of total RNA and real-time PCR was performed on a CFX96 Real Time PCR Detection System using SYBR green (Bio-Rad). Data were normalized to the housekeeping gene glyceraldehyde 3-phosphate dehydrogenase. Values represent mean \pm SD. GST-A1, glutathione S-transferase alpha 1; HO1, hemeoxygenase-1; MGST1, microsomal glutathione S-transferase 1; SOD, superoxide dismutase 1; NQO1, NAD(P)H quinone dehydrogenase 1, catalase.

Table 4A.2. Listed data for binding constant ($\log(K)$) measurement of **2**.

Entry	[2] (mM)	[TPEN] (mM)	Equilibrium * Constant	$\log(K)$
1	4.984	5.889	1.179	10.23
2	6.600	8.951	1.513	10.12
3	5.522	8.009	0.891	10.35

* Equilibrium constant is defined as the ratio of K_{TPEN}/K_2

References

- (1) Buttke, T. M.; Sandstrom, P. A. *Free Radic. Res.* **1995**, *22*, 389-397.
- (2) Serrano, F.; Klann, E. *Ageing Res. Rev.* **2004**, *3*, 431-443.
- (3) Sundaresan, M.; Yu, Z.-X.; Ferrans, V. J.; Irani, K.; Finkel, T. *Science* **1995**, *270*, 296-299.
- (4) Lyle, A. N.; Griendling, K. K. *Physiology* **2006**, *21*, 269-280.
- (5) Rhee, S. G. *Science* **2006**, *312*, 1882-1883.
- (6) Mosley, R. L.; Benner, E. J.; Kadiu, I.; Thomas, M.; Boska, M. D.; Hasan, K.; Laurie, C.; Gendelman, H. E. *Clin. Neurosci. Res.* **2006**, *6*, 261-281.
- (7) Fearon, I. M.; Faux, S. P. *J. Mol. Cell. Cardiol.* **2009**, *47*, 372-381.
- (8) Roberts, C. K.; Sindhu, K. K. *Life Sci.* **2009**, *84*, 705-712.
- (9) Gladden, J. D.; Ahmed, M. I.; Litovsky, S. H.; Schiros, C. G.; Lloyd, S. G.; Gupta, H.; Denney, T. S., Jr.; Darley-Usmar, V.; McGiffin, D. C.; Dell'Italia, L. J. *Am. J. Med. Sci.* **2011**, *342*, 114-119.
- (10) Eskici, G.; Axelsen, P. H. *Biochemistry* **2012**, *51*, 6289-6311.
- (11) Chang, M. C. Y.; Pralle, A.; Isacoff, E. Y.; Chang, C. J. *J. Am. Chem. Soc.* **2004**, *126*, 15392-15393.
- (12) Lippert, A. R.; Van de Bittner, G. C.; Chang, C. J. *Acc. Chem. Res.* **2011**, *44*, 793-804.
- (13) Koide, Y.; Urano, Y.; Kenmoku, S.; Kojima, H.; Nagano, T. *J. Am. Chem. Soc.* **2007**, *129*, 10324-10325.
- (14) Lim, M. H.; Xu, D.; Lippard, S. J. *Nat. Chem. Biol.* **2006**, *2*, 375-380.
- (15) Maeda, H.; Yamamoto, K.; Nomura, Y.; Kohno, I.; Hafsi, L.; Ueda, N.; Yoshida, S.; Fukuda, M.; Fukuyasu, Y.; Yamauchi, Y.; Itoh, N. *J. Am. Chem. Soc.* **2005**, *127*, 68-69.
- (16) McQuade, L. E.; Ma, J.; Lowe, G.; Ghatpande, A.; Gelperin, A.; Lippard, S. J. *Proc. Nat.*

- Acad. Sci., U. S. A.* **2010**, *107*, 8525-8530.
- (17) Lou, Z.; Li, P.; Han, K. *Acc. Chem. Res.* **2015**, *48*, 1358-1368.
- (18) Caravan, P.; Ellison, J. J.; McMurry, T. J.; Lauffer, R. B. *Chem. Rev.* **1999**, *99*, 2293-2352.
- (19) Major, J. L.; Meade, T. J. *Acc. Chem. Res.* **2009**, *42*, 893-903.
- (20) De Leon-Rodriguez, L. M.; Lubag, A. J. M.; Malloy, C. R.; Martinez, G. V.; Gillies, R. J.; Sherry, A. D. *Acc. Chem. Res.* **2009**, *42*, 948-957.
- (21) Loving, G. S.; Mukherjee, S.; Caravan, P. *J. Am. Chem. Soc.* **2013**, *135*, 4620-4623.
- (22) Aime, S.; Botta, M.; Gianolio, E.; Terreno, E. *Angew. Chem. Int. Ed.* **2000**, *39*, 747-750.
- (23) Tsitovich, P. B.; Sperryak, J. A.; Morrow, J. R. *Angew. Chem. Int. Ed.* **2013**, *52*, 13997-14000.
- (24) Ratnakar, S. J.; Viswanathan, S.; Kovacs, Z.; Jindal, A. K.; Green, K. N.; Sherry, A. D. *J. Am. Chem. Soc.* **2012**, *134*, 5798-5800.
- (25) Tu, C.; Nagao, R.; Louie, A. Y. *Angew. Chem. Int. Ed.* **2009**, *48*, 6547-6551.
- (26) Yu, M.; Beyers, R. J.; Gorden, J. D.; Cross, J. N.; Goldsmith, C. R. *Inorg. Chem.* **2012**, *51*, 9153-9155.
- (27) Yu, M.; Ambrose, S. L.; Whaley, Z. L.; Fan, S.; Gorden, J. D.; Beyers, R. J.; Schwartz, D. D.; Goldsmith, C. R. *J. Am. Chem. Soc.* **2014**, *136*, 12836-12839.
- (28) Viger, M. L.; Sankaranarayanan, J.; de Gracia Lux, C.; Chan, M.; Almutairi, A. *J. Am. Chem. Soc.* **2013**, *135*, 7847-7850.
- (29) Chen, J. W.; Pham, W.; Weissleder, R.; Bogdanov, A., Jr. *Magn. Reson. Med.* **2004**, *52*, 1021-1028.
- (30) Breckwoldt, M. O.; Chen, J. W.; Stangenberg, L.; Aikawa, E.; Rodriguez, E.; Qiu, S.; Moskowitz, M. A.; Weissleder, R. *Proc. Nat. Acad. Sci., U. S. A.* **2008**, *105*, 18584-18589.

- (31) Panizzi, P.; Nahrendorf, M.; Wildgruber, M.; Waterman, P.; Figueiredo, J.-L.; Aikawa, E.; McCarthy, J.; Weissleder, R.; Hilderbrand, S. A. *J. Am. Chem. Soc.* **2009**, *131*, 15739-15744.
- (32) Raghunand, N.; Jagadish, B.; Trouard, T. P.; Galons, J.-P.; Gillies, R. J.; Mash, E. A. *Magn. Reson. Med.* **2006**, *55*, 1272-1280.
- (33) Hyodo, F.; Matsumoto, K.-i.; Matsumoto, A.; Mitchell, J. B.; Krishna, M. C. *Cancer Res.* **2006**, *66*, 9921-9928.
- (34) Toftlund, H.; Pedersen, E.; Yde-Andersen, S. *Acta. Chem. Scand. A* **1984**, *38*, 693-697.
- (35) Smith, R. M.; Martell, A. E. *Critical Stability Constants*, 1st ed.; Plenum Press: New York, NY, 1975; Vol. 2, pp 249.
- (36) Bernstein, M. A.; King, K. F.; Zhou, X. J. *Handbook of MRI Pulse Sequences*; Elsevier Academic Press: Amsterdam, 2004.
- (37) Haacke, E. M.; Brown, R. W.; Thompson, M. R.; Venkatesan, R. *Magnetic Resonance Imaging: Physical Principles and Sequence Design*; John Wiley & Sons: New York, NY, 1999.
- (38) Nelder, J. A.; Mead, R. *Comput. J.* **1965**, *7*, 308-313.
- (39) Iranzo, O. *Bioorg. Chem.* **2011**, *39*, 73-87.
- (40) McCord, J. M.; Fridovich, I. *J. Biol. Chem.* **1969**, *244*, 6049-6055.
- (41) Kedare, S. B.; Singh, R. P. *J. Food Sci. Technol.* **2011**, *48*, 412-422.
- (42) Milaeva, E. R.; Shpakovsky, D. B.; Gracheva, Y. A.; Orlova, S. I.; Maduar, V. V.; Tarasevich, B. N.; Meleshonkova, N. N.; Dubova, L. G.; Shevtsova, E. F. *Dalton Trans.* **2013**, *42*, 6817-6828.
- (43) Ancerewicz, J.; Migliavacca, E.; Carrupt, P.-A.; Testa, B.; Brée, F.; Zini, R.; Tillement, J.-

- P.; Labidalle, S.; Guyot, D.; Chauvet-Monges, A.-M.; Crevat, A.; Le Ridant, A. *Free Rad. Biol. Med.* **1998**, *25*, 113-120.
- (44) Fryer, J. R.; Morris, D. F. C. *Talanta* **1968**, *15*, 1309-1312.
- (45) Shannon, R. D. *Acta Cryst.* **1976**, *A32*, 751-767.
- (46) Coates, C. M.; Hagan, K.; Mitchell, C. A.; Gorden, J. D.; Goldsmith, C. R. *Dalton Trans.* **2011**, *40*, 4048-4058.
- (47) Chan, T.-L.; Mak, T. C. W. *J. Chem. Soc., Perkin Trans. 2* **1983**, 777-781.
- (48) Owsik, I.; Kolarz, B. *J. Mol. Catal. A* **2002**, *178*, 63-71.
- (49) Gill, N. S.; Nuttall, R. H.; Scaife, D. E.; Sharp, D. W. A. *J. Inorg. Nucl. Chem.* **1961**, *18*, 79-87.
- (50) Jiang, W.; Gorden, J. D.; Goldsmith, C. R. *Inorg. Chem.* **2013**, *52*, 5814-5823.
- (51) Goldsmith, C. R.; Cole, A. P.; Stack, T. D. P. *J. Am. Chem. Soc.* **2005**, *127*, 9904-9912. 31
- (52) Hubin, T. J.; McCormick, J. M.; Alcock, N. W.; Busch, D. H. *Inorg. Chem.* **2001**, *40*, 435-444.
- (53) Giorgio, M.; Trinei, M.; Migliaccio, E.; Pelicci, P. G. *Nat. Rev. Mol. Cell. Biol.* **2007**, *8*, 722-728.
- (54) Zhang, Y. W.; Shi, J.; Li, Y. J.; Wei, L. *Arch. Immunol. Ther. Exp. (Warsz)* **2009**, *57*, 435-445.
- (55) Zhang, S.; Liu, X.; Bawa-Khalfe, T.; Lu, L. S.; Lyu, Y. L.; Liu, L. F.; Yeh, E. T. *Nat. Med.* **2012**, *18*, 1639-1642.
- (56) Al-Shabanah, O. A.; Aleisa, A. M.; Hafez, M. M.; Al-Rejaie, S. S.; Al-Yahya, A. A.; Bakheet, S. A.; Al-Harbi, M. M.; Sayed-Ahmed, M. M. *Oxid. Med. Cell. Longev.* **2012**, *2012*, 619185.

- (57) Tenore, G. C.; Manfra, M.; Stiuso, P.; Coppola, L.; Russo, M.; Gomez Monterrey, I. M.; Campiglia, P. *J. Agric. Food Chem.* **2012**, *60*, 9680-9687.
- (58) Blois, M. S. *Nature* **1958**, *181*, 1199-1200.
- (59) Zhang, Q.; Gorden, J. D.; Goldsmith, C. R. *Inorg. Chem.* **2013**, *52*, 13546-13554.
- (60) Goldsmith, C. R.; Lippard, S. J. *Inorg. Chem.* **2006**, *45*, 6474-6478.
- (61) Ba, L. A.; Doering, M.; Burkholz, T.; Jacob, C. *Metallomics* **2009**, *1*, 292-311.
- (62) Drahoš, B.; Lukeš, I.; Tóth, É. *Eur. J. Inorg. Chem.* **2012**, *2012*, 1975-1986.
- (63) Zhang, Q.; Gorden, J. D.; Beyers, R. J.; Goldsmith, C. R. *Inorg. Chem.* **2011**, *50*, 9365-9373.
- (64) Batinic-Haberle, I.; Rajic, Z.; Tovmasyan, A.; Reboucas, J. S.; Ye, X.; Leong, K. W.; Dewhirst, M. W.; Vujaskovic, Z.; Benov, L.; Spasojevic, I. *Free Rad. Biol. Med.* **2011**, *51*, 1035-1053.
- (65) Aitken, J. B.; Shearer, E. L.; Giles, N. M.; Lai, B.; Vogt, S.; Reboucas, J. S.; Batinic-Haberle, I.; Lay, P. A.; Giles, G. I. *Inorg. Chem.* **2013**, *52*, 4121-4123.

Chapter 5

Summary and Future Perspectives

In this chapter I make a brief summary of the three projects that we have completed so far and itemize the advantages and disadvantages of the three MRI contrast agents. I also outline potential future directions for the research.

We used three different redox-responsive ligands to synthesize three manganese(II)-based MRI contrast agents. Upon reacting with H_2O_2 , each of the three complexes displayed changes in T_1 relaxation time via ligand structural changes. The oxidation-triggered changes in the ligand structure either decrease the paramagnetism per manganese unit or increase the inner-sphere hydration number (q) of the metal center.

The Mn-Htp1 complex exhibits a $0.8 \text{ mM}^{-1}\text{s}^{-1}$ decrease in r_1 in the presence of excess H_2O_2 ; this is attributed to the formation of a binuclear Mn(II) species with a magnetic moment of $4.5 \mu_{\text{B}}$ per metal ion.¹ Further study has indicated that nearly negligible anti-ferromagnetic coupling exists between the two Mn(II) centers; the observed paramagnetic moment seems typical for binuclear manganese complex with noninteracting metal centers.² Regrettably, our experiments with bovine serum albumin (BSA) failed to show an enhancement in r_1 suggesting that the sensor cannot couple to this protein as it did with a small molecule phenol. We currently hypothesize that the tyrosine residues on BSA are insufficient in either number or accessibility to allow our probe to label the protein. Nonetheless, I feel that the phenol coupling reaction can be exploited to label regions of oxidative stress. Liposomes, as I mentioned earlier in the introduction chapter, are widely used in different areas. These can self-assemble from lipids containing hydrophobic and hydrophilic functional groups. Introducing phenol moieties to these lipids can potentially provide a means to attach the sensor to the liposome surface.

The second and third MRI contrast agents incorporate redox-responsive quinol groups that can be oxidized to *para*-quinone which have weaker binding affinities for the Mn(II). Unlike the

Mn-Htp1 complex, these two sensors exhibit turn-on responses to H_2O_2 due to the increase of q . We sought to improve the modest r_1 enhancement of the Mn- $\text{H}_2\text{qtp1}$ complex by replacing one of its pyridine rings with an additional quinol. Although the r_1 increase does improve, the stability of sensor is compromised in terms of its metal-binding affinity and its sensitivity to contaminant metal ions and O_2 .

One option for solving the stability issue would be to introduce a macrocycle, such as a cyclen, into the ligand structure; but synthesizing such cyclen derivatives with quinol arms has thus far proven to be a challenge. There are several problems: 1) the quinol is sensitive to both base and oxygen, necessitating protecting groups and a more completed synthetic route; 2) the steric hindrance on the macrocycles makes the introduction of quinol rings more difficult than it is for the acyclic structures; 3) additionally, the macrocycle only improves the binding affinity of ligand but doesn't guarantee better O_2 stability. The benefits that macrocyclic ligands can provide may not be worth the effort.

Notably, both Mn- $\text{H}_2\text{qtp1}$ and Mn- $\text{H}_4\text{qtp2}$ complexes are strong anti-oxidants. One major concern about using redox-active metals as paramagnetic reporters in MRI contrast agents is that the metals themselves can generate ROSs.³ The redox-activity of the metals can therefore generate a false positive result for ROS imaging. That our sensors degrade ROSs, instead of generating them, is a significant advantage. Further, the anti-oxidant activity is attractive in that a single compound can be used to both monitor and treat oxidative stress. The intrinsic mechanisms of the reactions between these Mn complexes and superoxide and other ROSs remain unclear, representing another avenue for future research.

The redox-activity of the ligand by itself may be sufficient for the anti-oxidant activity. Another current direction focuses on a Zn- $\text{H}_2\text{qtp1}$ complex. The advantages to using Zn(II)

instead of Mn(II) is that the metal ion binds more strongly to more ligands and is less toxic in its free form.⁴ A Zn(II)-reliant SOD mimic would therefore be active for a longer period of time while allowing a higher loading. The incorporation of redox-inactive Zn(II) into the H₂qtp1 ligand thus far seems to enhance the SOD activity. How the activity is improved remains to be clarified. One hypothesis is that the Zn(II) facilitates proton-coupled-electron-transfer (PCET) processes between the metal complex and HO₂. Alternatively, the Zn(II) could improve the activity by attracting anionic superoxide towards the redox-active quinol portion of the molecule.⁵

One major improvement of Mn-H₄qtp2 over Mn-H₂qtp1 is that its response is suitable for *ex vivo* cardiac imaging. There are many challenges that must be overcome to translate a successful *in vitro* r_1 response into a clinically useful diagnostic technique. The criteria for redox-responsive MRI contrast agents are currently nebulous. One major issue is that *in vivo* concentrations of ROSs under normal and aberrant conditions are poorly defined. Another issue is that the localization of the contrast agent probe is difficult to predict and control *a priori*. The success of our experiments with doxorubicin (DOX) should therefore be considered serendipitous. We were fortunate in that the Mn-H₄qtp2 probe collected, seemingly intact, within the heart. We were further fortunate in that the concentrations of ROSs of the DOX- and vehicle-treated hearts led to observable differences in the MRI contrast. Altering the pharmacological properties of the sensors represents another possible avenue for research. The stability of the probe can be addressed more readily than its bodily distribution.

Our current research is focused on T_1 -weighted MRI contrast agents, but other mechanisms for contrast agent turn-on exist. One such mechanism involves chemical exchange saturation transfer (CEST), which is facilitated by using a paramagnetic contrast agent to further

differentiate the resonance frequencies of the contrast agent's protons from those of the bulk water (PARACEST).⁶ PARACEST contrast agents have recently attracted the attention of many research groups. The PARACEST signal, represented by the net magnetization of water protons under steady state (M_z/M_0), is affected by three terms: the number of exchangeable protons (q), the longitudinal relaxation time of bulk water (T_1), and the proton exchange rate ($1/\tau_m$) as indicated by the following equation.^{7, 8} The influences of q and τ_m are relatively straightforward; but we should be aware that the CEST signal will be quenched if T_1 is shorter than τ_m .⁹ One wants to introduce paramagnetic metals in order to increase the energy gap between exchanging proton pools and minimize the background noise. The need for a reasonable water/proton exchange rate precludes the use of some transition metals, such as Mn(II) and Gd(III), for PARACEST.⁶

$$M_z/M_0 (\%) = 100 (1 + cqT_1/55.5\tau_m)^{-1}$$

Ni(II) and Co(II) PARACEST agents have been reported.^{10, 11} Unlike lanthanides, first-row transition metals are generally more redox-active and can have multiple accessible oxidation states that can be manipulated to tune the CEST signal. One promising future direction would be to coordinate H₂qtp1 or H₄qtp2 to Ni(II). Given that the quinols have exchangeable protons that are in fast equilibrium with those from the bulk water, the bulk water signal should be diminished when the reduced form of the sensor is present. In the presence of oxidants, such as H₂O₂, these quinols convert into *para*-quinones, which lack exchangeable protons. This quenches CEST and thereby improves the intensity of the bulk water's signal. There are several challenges related with this project: 1) the chemical shift ($\Delta\omega$) between the quinolic OH protons and the water protons must be large enough to qualify for CEST contrast;¹² 2) although Ni(II) is redox-active, its ability to catalyze quinol oxidation remains unknown; 3) the quinol –OH groups

generally have a very fast proton exchange rate that exceeds the $\Delta\omega$ and therefore no CEST effect can be observed;^{6, 13} 4) a large pH-dependence should be expected in the CEST effect and this may make the sensor extremely sensitive to environmental effects; 5) protons from metal-bound water molecules may also influence or even eliminate the CEST effect.

References

- (1) Yu, M.; Beyers, R. J.; Gorden, J. D.; Cross, J. N.; Goldsmith, C. R. *Inorg. Chem.* **2012**, *51*, 9153–9155.
- (2) Lieb, D.; Friedel, F. C.; Yawer, M.; Zahl, A.; Khusniyarov, M. M.; Heinemann, F. W.; Ivanović-Burmazović, I. *Inorg. Chem.* **2013**, *52*, 222–236.
- (3) Roberts, C. K.; Sindhu, K. K. *Life Sciences* **2009**, *84*, 705–712.
- (4) Nordberg, G. F.; Fowler, B. A.; Nordberg, M. Handbook on the Toxicology of Metals - Google Books, 4th ed.; Elsevier, 2014; Vol. 1.
- (5) Miriyala, S.; Spasojevic, I.; Tovmasyan, A.; Salvemini, D.; Vujaskovic, Z.; St Clair, D.; Batinic-Haberle, I. *Biochim. Biophys. Acta* **2012**, *1822*, 794–814.
- (6) Woods, M.; Woessner, D. E.; Sherry, A. D. *Chem. Soc. Rev.* **2006**, *35*, 500–511.
- (7) Woessner, D. E.; Zhang, S.; Merritt, M. E.; Sherry, A. D. *Magn. Reson. Med.* **2005**, *53*, 790–799.
- (8) Viswanathan, S.; Kovacs, Z.; Green, K. N.; Ratnakar, S. J.; Sherry, A. D. *Chem. Rev.* **2010**, *110*, 2960–3018.
- (9) Terreno, E.; Boffa, C.; Menchise, V.; Fedeli, F.; Carrera, C.; Castelli, D. D.; Digilio, G.; Aime, S. *Chem. Commun.* **2011**, *47*, 4667.
- (10) Dorazio, S. J.; Tsitovich, P. B.; Sifers, K. E.; Sperryak, J. A.; Morrow, J. R. *J. Am. Chem. Soc.* **2011**, *133*, 14154–14156.
- (11) Olatunde, A. O.; Dorazio, S. J.; Sperryak, J. A.; Morrow, J. R. *J. Am. Chem. Soc.* **2012**, *134*, 18503–18505.
- (12) Li, A. X.; Suchy, M.; Li, C.; Gati, J. S.; Meakin, S.; Hudson, R. H. E.; Menon, R. S.; Bartha, R. *Magn. Reson. Med.* **2011**, *66*, 67–72.

- (13) Soesbe, T. C.; Wu, Y.; Sherry, A. D. *NMR Biomed.* **2013**, *26*, 829–838.